Emerging Electronic Materials: Thin Films of Asphaltenes and Coal Nanoparticles for Electronic Devices and Large Area Layer Controlled 2-Dimensional Semiconductor Synthesis.
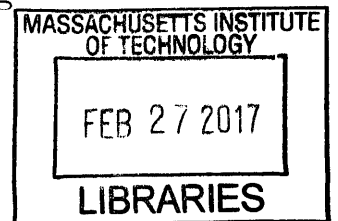
by

Brent D. Keller

Submitted to the Department of Materials Science and Engineering
in partial fulfillment of the requirements for the degree of

Doctor of Philosophy in Materials Science and Engineering

at the

MASSACHUSETTS INSTITUTE OF TECHNOLOGY

September 2016

Author .... **Signature redacted**

Department of Materials Science and Engineering
July 26, 2016

Certified by .... **Signature redacted**

Jeffrey C. Grossman
Professor of Materials Science and Engineering
Thesis Supervisor

Accepted by .... **Signature redacted**

Donald R. Sadoway
Chair, Departmental Committee on Graduate Studies

MITLibraries

DISCLAIMER NOTICE

Due to the condition of the original material, there are unavoidable flaws in this reproduction. We have made every effort possible to provide you with the best copy available.

Thank you.

The images contained in this document are of the best quality available.

Emerging Electronic Materials: Thin Films of Asphaltenes and Coal Nanoparticles for Electronic Devices and Large Area Layer Controlled 2-Dimensional Semiconductor Synthesis.

by

Brent D. Keller

Abstract

Materials for energy and electronic applications is a rich ecosystem. This thesis desribes the work I have performed with the help of my colleages to push the boundaries of this space both in materials processing and unique materials development. In particular, I studied two classes of materials in detail. The first are disordered natural carbonaceous materials which I prepared from source material such as coal and asphaltenes. The second are two dimensional materials in particular transition metal dichalcogenides.

Following an introduction to the materials I have studied in chapter 1, in chapters 2 and 3 I will discuss a class of materials which have seen extensive academic interest for energy and electronic applications: carbon materials. Specifically disordered carbon materials, both amorphous and with long-range order (for example, -C:H and reduced graphene oxide), have been used in a variety of optical and electronic applications from conductive additives and contact materials to transistors and photovoltaics. In contrast, the electronic properties of solid natural carbon materials such as coal have not been explored beyond basic bulk electrical conductivity measurements for correlation with combustion and gasification yields. I will discuss a number of exciting results from exploration of this neglected space:

1) Development of a method of fabrication of thin films of coal nanoparticles based on ball milling and solution processing

2) Chemical, electrical, structural, and optical characterization of the properties of coal thin films through Raman, X-ray photoelectron and UV-Vis spectroscopies as well as low temperature charge transport studies.

3) Fabrication of thin film Joule heating devices which compete with or outperform many reported synthetic materials.

4) Exploration of the electrical properties of thin films of asphaltenes and vacuum

residuals for photovoltaic applications.

Based on these experiments, the solid natural carbon phase space has proven to be rich and promising. Electrical conductivities range over orders of magnitude, and thermal treatment of the resulting films increases the sp^2 content, disorder, and tunes the electrical conductivity in excess of 7 orders of magnitude. Optical absorption measurements demonstrate tunable optical gaps from 0 to 1.8 eV, and low-temperature conductivity measurements demonstrate that variable range hopping controls the electrical properties in both as-prepared and thermally treated films. The measured hopping energies further demonstrate electronic properties similar to vacuum deposited amorphous carbon materials and reduced graphene oxide.

Next in chapter 4, while very promising work for square inch and larger scale methods of uniform monolayer deposition of 2-dimensional (2D) semiconductors such as MoS_2 has been performed, complete film growth and inhibition of bilayer or thicker nucleation has proven difficult. I will present a divergent growth method for MoS_2 via sulfurization of oxide deposited by both thermal ALD from $(tBuN)_2(NMe_2)_2Mo$ and O_3 and plasma enhanced ALD (PEALD) from $(tBuN)_2(NMe_2)_2Mo$ and remote O_2 plasma. Large uniform MoS_2 areas were achieved by studying the effects of various growth process conditions and surface treatments to control the nucleation and growth of MoO_3 and through a detailed study of the chemistry of the film for varied post-sulfurization temperature profiles.

Finally, as discussed in chapter 5, vapor deposition methods are not the only approaches to manufacture of 2D semiconductors. The ultimate in low cost fabrication is based on solution exfoliation of bulk material. After developing a process for depositing materials in this manner, I studied several chemical and thermal methods for removing cholate – a ligand used during the solution exfoliation process – from the films after deposition to improve the purity and quality of the films. I also worked with scotch tape mechanically exfoliated materials to test the properties of heterojunctions of MoS_2 and graphene and demonstrate quenching of the MoS_2 photoluminescence indicating charge injection into the graphene sheet.

Thesis Supervisor: Jeffrey C. Grossman
Title: Professor of Materials Science and Engineering

Acknowledgments

A PhD is approximately 5 years of open ended projects, extremely branching decision trees, often limited guidance, and incredible learning experiences. I have many people to thank who enriched my journey scientifically and emotionally. My committee members, Professor Silvija Gradečak and Professor Harry Tuller, both provided excellent guidance and feedback on this document. I would like to thank Dr. Adam Bertuch for an extremely fruitful collaboration on the ALD guided synthesis of MoS_2. In particular, Adam performed all of the MoO_3 ALD and PEALD depositions discussed in this work. I would also like to thank Dr. Nicola Ferralis, Dr. Ganesh Sundaram, and Dr. J Provine for their help planning experiments, interpreting data, and drafting manuscripts. I was lucky enough to provide mentorship to Mahmoud Ghulman, Andrii Omelianovych, Ferderico Pinna, Patrick Yu, and Corrine Drysdale. All were talented and eager students and have promising careers ahead of them. I would also like to thank my colleagues Dr. Eric Johlin, Dr. David Zhitomirsky, and again Dr. Nicola Ferralis for their guidance in the laboratory and in experimental and device design – particularly in the early years of my PhD. A graduate student has many teachers, and I would particularly like to thank these three.

In addition to being a visionary scientist and talented advisor, Professor Jeff Grossman has also created a work environment full of talented and collaborative people. I received some excellent advice from Professor Christopher Schuh when I arrived at MIT, to pick my advisor and colleagues by their advising style more than project I would be working on. Rarely did a day go by that I was not thankful for how much I enjoy being in the company of my colleagues in the Grossman group, and Professor Grossman in particular. I cannot image a more rewarding place to learn and contribute to science.

My parents are two truly inspirational people without whose support and wisdom, I would not have come this far. Their commitment to my education from a very young age was a truly great gift even if not always graciously received, and for that I owe them a great deal. They have also always been available in times of need and gave

me some of the most important advice that I have lived my life by. They are, truly, the best parents I could have hoped for, and I am deeply grateful for everything they have given me. If that was not enough, their ability to transition smoothly from protector or counselor to friend and compatriot is rare in such exceptional parents. I have always been honored to introduce them to the people I have met in my life outside of their home because of their kindness, charm, and authenticity.

The last five years have also seen great personal change in my life. I would like to thank my friends, in particular, Corentin Monmeyran, Alex Toumar, and David Bursaw for being my emotional safety net in times of need. I would also like to thank Dr. Shreya Dave for bridging the gap between colleague and friend and thus enriching both my science and my life. I have been truly blessed in who I can call my friends. Finally, I would like to thank my partner, Mitul Daiyan. For the last year, she has been my support in my greatest times of stress, and my greatest source of laughter in times of joy. I am overwhelmed with happiness at the prospect of taking her with me into the next chapter of my life. Before her, I could not have imagined a partner who both completes who I am and yet adds so many new dimensions to my life.

Contents

Chapter 1

Background and Motivations

Materials scientists often note that historians name the age that humanity lives in by the material which defines our newest class of tools. Prehistory is divided into the Stone, Bronze, and Iron Ages as advances in metallurgy enabled the smelting of metals – the first materials processing to involve chemical transformations. Materials scientists can certainly be forgiven for glossing over periods typically defined in political or cultural contexts, for example classical antiquity in the Mediterranean basin, or the Han Dynasty in parts of East Asia. Modern history has demarcations for the Industrial Revolution (a larger engineering achievement), as well as the Plastics Age, and now the Silicon Age. Such a labeling scheme emphasizes the impact of materials on the sophistication and capabilities of the tools we use in all aspects of our lives and which shape our culture and politics. But it (as any classification system must) also oversimplifies and glosses over the richness and nuances of even the materials science it leverages to differentiate eras of time. The aggressive performance improvements in computing power known collectively as Moore's Law and which characterize the Silicon Age have been made possible in large part by the expansion of the materials space used in computer chips. Germanium to strain silicon and increase carrier mobility, hafnium oxide as a higher performance gate dielectric, and tantalum nitride as a glue and diffusion barrier for copper interconnects – to name a few. But it is not just the materials processed, but the unprecedented level of control. Nanotechnology enables FinFET architectures and nanometer thickness films to meet the

performance requirements demanded by Moore's Law. Even further, the tremendous modern materials space dovetails with this ability to process at the nanoscale. It is not just the material or even the device geometry that determines its properties, but the atomic detail of the materials structure inherited from how it was processed that often determines the performance of the device.

This thesis covers the processing and properties of two exciting materials systems just beginning to be understood at the level of detail and manner needed to join the many others already being used for optical and electronics applications. The first, natural carbon, is the class of solid carbonaceous materials currently used primarily for combustion. Specifically discussed in this work are coals, asphaltenes, and vacuum distillation residuals. The second, transition metal dichalcogenides, are a class of two dimensional semiconductors which have attracted great attention since their tunable semiconducting properties were demonstrated in 2010. I have endeavored to develop methods of processing these materials and characterize to understand the impact of processing on their atomic structure as well as larger morphology.

1.1 Natural Cabon

Since the industrial revolution the burning of fossil fuels has been the keystone of our economic system and will likely continue to do so unless economically attractive alternatives are found. In recent decades, many exiting carbon materials such as polymers, small molecule semiconductors, carbon nanotubes, fullerenes, amorphous carbon, graphene, and reduced graphene oxide, have been developed for many optical and electronic applications such as transistors, photovoltaics (PV), light emitters, optical and chemical sensors, batteries, piezoelectrics, transparent conductors, and many others. In contrast, the modern economy and the lifestyles it supports are extremely reliant on the combustion of fossil fuels, and a massive phase space of naturally synthesized carbon materials is used primarily for combustion. A transition from a wasteful and environmentally damaging use of our carbon legacy to a more sustainable and technologically sophisticated use of the carbon materials could mean

a paradigm shift in our approach to the energy crisis. And recent work suggests, that there are other better to find energy with carbon – instead of breaking carbon bonds via combustion, we can leverage those same bonds as a renewable energy resource. Consider PV as an example, there are the two families of carbon-based PV cells under development now: solar cells made from oil-derived polymers, with 30–40% carbon content and up to 10% efficiency [1], or the more recent solar cells made entirely from artificial carbon nanomaterials such as nanotubes, graphene and fullerenes [2, 3, 4, 5]. Such solar cells with up to 90% carbon content showed 1–2% efficiency initially [2, 3], but now as large as 3.1% even with the subistution of polychiral nanotubes for much more expensive single chirality tubes [6].

While synthetic carbon materials have attracted great research attention and seen great success particularly in the light emission space, they have seen only limited commercial success for many other applications. This is in large part because of the high cost of synthesizing and purifying materials such as fullerenes and nanotubes, and challenges with chemical and optical stability for many small molecules and polymers. From a materials perspective, Natural Carbon on the other hand possesses three of the most important attributes for large-scale use: low cost, wide availability and extreme materials flexibility. Raw natural carbonaceous materials such as coal are broadly available (e.g. 250 Mton/year for coal) at very low cost. In addition, natural carbonaceous materials possess extensive chemical and physical variability. For example, they can be conductive as well as insulating in their natural state, with excellent light absorption properties due to the presence of multiple complex chemical phases and to a wide range of existing carbon allotropes and complex chemical diversity. Figure 1-1 shows chemical models of just two coals with different maturity highlighting tremendous range of chemical properties availble by materials selection [7]. Such inherent diversity in raw carbonaceous materials constitutes an untapped resource, and a useful means to more readily tune the desired optical and electronic properties, as is essential in the development of materials for renewable energy (and PV cells in particular) [8]. Petroleum products have for decades been seen as chemically interesting materials to be separated, processed, purified, and modified for applications

11

ranging from lubricants to plastics to food additives. If even a small fraction of the level of sophisticated chemistry and materials science that is applied to natural liquid carbon sources was applied to natural solid carbon sources, the wealth of properties provided by these materials could prove game changing in the energy market.

The primary goal of this portion of my thesis is to develop methods of processing thin films of natural carbon materials and characterize the electrical, morphological, and optical properties of these thin films. I have also endeavored to develop first applications for these natural carbon materials that leverages their electronic tunablilty. Because of the novelty of this perspective on natural carbon, a large gap of fundamental understanding of materials properties has to be bridged as ever more sophisticated devices are designed. My work to bridge that gap has focused on a subset of coal materials (Chapter 2) and solid byproducts of crude oil processing (Chapter 3).

We scientists and engineers have harnessed energy from fossil fuels in myriad ways to build our modern society. And we are also the ones who must create a new way to obtain that energy: a clean, safe, renewable way that could last not just another fifty to hundred years but as long as the sun itself. We are responsible for using science and technology to place humanity in a more sustainable position with respect to the planet. And unlike the many other technology revolutions that have occurred, this revolution will center almost entirely around our ability to carefully design and manufacture completely new materials and understand the impact of processing on the atomic details which give rise to their properties. A successful demonstration that it is possible to use the cheap, abundant naturally occurring forms of carbon such as coal as the basis for renewable energy technologies, would represents a dramatic shift in the way we think about this precious resource.

1.2 Transition Metal Dichalcogenides

Most electronic devices are planar or fabricated on a planar substrate. Processing, charge carrier extraction, light admittance or emission, and requirements of a sup-

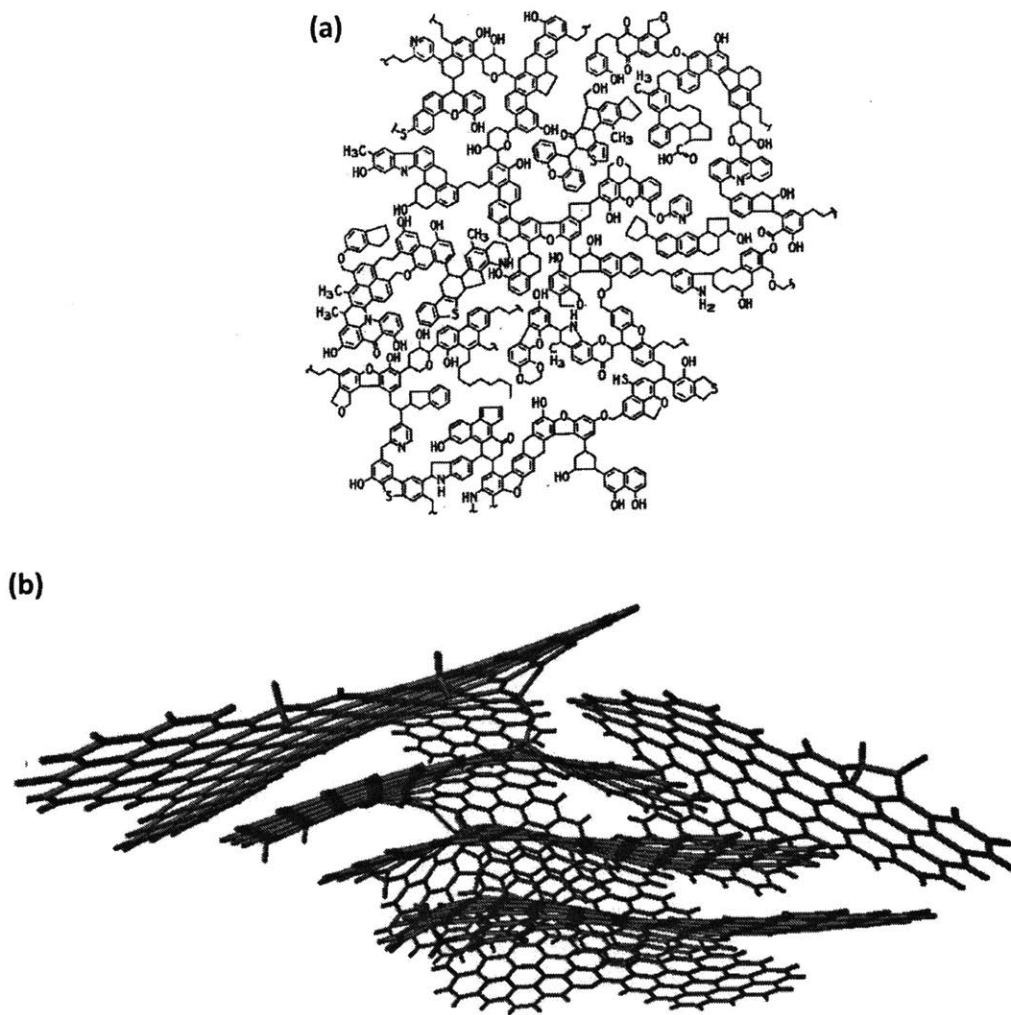Figure 1-1:   Chemical models for a bituminous coal (a) showing its highly aliphatic nature and an anthrcite coal (b) showing its highly graphitic nature. The size of aramatic domains and compositions vary greatly between the samples. Reproduced from [9] and [7] respectively.
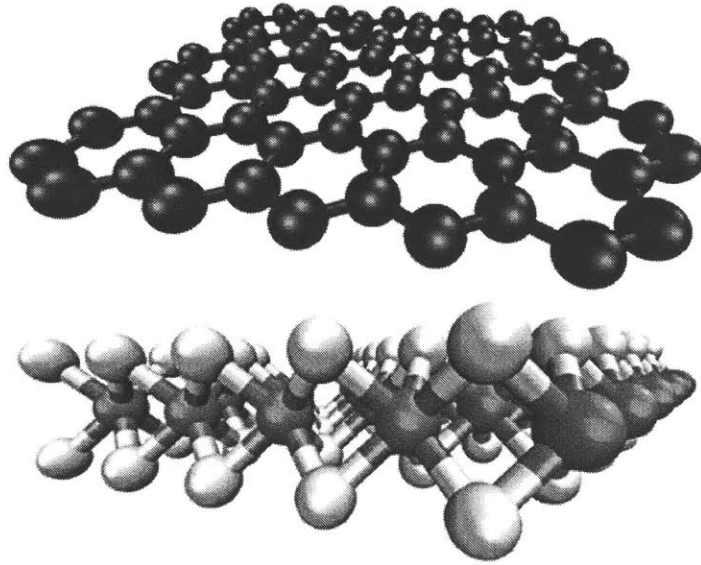
Figure 1-2:   Models of the crystal structure of grpahene (top) and a monolayer of the 2H crystal stucture of MoS_2.

portive substrate require that more often than not, devices are fabricated as a painter paints on canvass – deposited and patterned on top of a wafer of silicon or sheet of glass. As computing devices are made smaller and denser, the thickness of the material can provide problems for devices designed as structures upon a sheet of paper. The edge of a material film means a disruption of the chemical periodicity that gives rise to the semiconducting properties in the bulk. In addition, ever shrinking transistors eventually run into a class of problems known as short channel effects. The thinner the transistor channel can be made, the closer the source and drain can be spaced without the loss of device performance. Thus a material which is fundamentally two dimensional (2D) – only one crystal unit thick with no incomplete covalent bonds – offers inherent advantages simply for that reason. Such materials often have other exciting properties due to either 2D nature such as very strong interactions with light robustness as discussed below. Figure 1-2 shows models of the structure of graphene and molybdenum disulfide (MoS_2), the two most studied 2D materials and the centerpieces of this half of my thesis.

Although only purposefully isolated in 2004 [10], graphene has been extensively studied for a variety of scientific and technical reasons in subsequent years. Of impor-

14

tance to its application to 2D PV is its exceptional carrier mobility which can exceed 200,000 cm^2 V^{-1} s^{-1} when suspended [11]. For use in lower-cost applications, it can be synthesized by chemical vapor deposition (CVD) to produce high quality films of large areas[12, 13, 14] including roll-to-roll production of sheets as large as 30 in [15]. CVD growth of graphene on polycrystalline Cu foils is of particular interest because the reaction is surface mediated and terminates after the production of a single sheet of graphene [16, 17]. Carrier mobilites in CVD graphene are typically around 10,000 cm^2 V^{-1} s^{-1} when measured on SiO$_2$/Si substrates due to the formation of multiple crystal domains in CVD grown graphene films [12, 16].

Figure 1-3a shows an optical microscopy image of graphene I produced using such CVD methods and transferred to a SiO$_2$/Si wafer using a poly(methyl methacrylate) (PMMA) transfer method (see Chapter 6 for details). The image was chosen to include a region in which the film was torn during transfer (top right) to provide contrast to the graphene which otherwise covers the region. Some small darker spots are also visible indicating small regions of multiple layer formation. A representative Raman spectrum for the sample taken after growth (Figure 1-3b) is also included. The large 2D peak (2660 cm^{-1}) indicates the formation of monolayer graphene (see methods, Chapter 6, for discussion of Raman spectroscopy interpretation).

Unfortunately, despite its excellent transport properties, graphene has no electronic band gap limiting its application in semiconductor devices. For example, graphene transitors typically have on/off ratios of approximately 3 meaning logic devices assembled from these materials would require very large power consumption [18]. Several approaches have been taken to introduce a significant band gap into graphene, but all have come at the cost of many of its exciting transport properties. For example, partial sp^3 functionalization of the graphene sheet disrupts the sp^2 electronic structure opening a gap. This approach has been taken with hydrogen [19, 20, 21], flourine [22, 23, 24], and aromatic [25, 26, 27, 28] functionalizations amongst others. While covalent functionalization of graphene has proven very effective in introducing a band gap in the material, it also introduces disorder into the graphene lattice which hampers carrier transport and can be observed through the
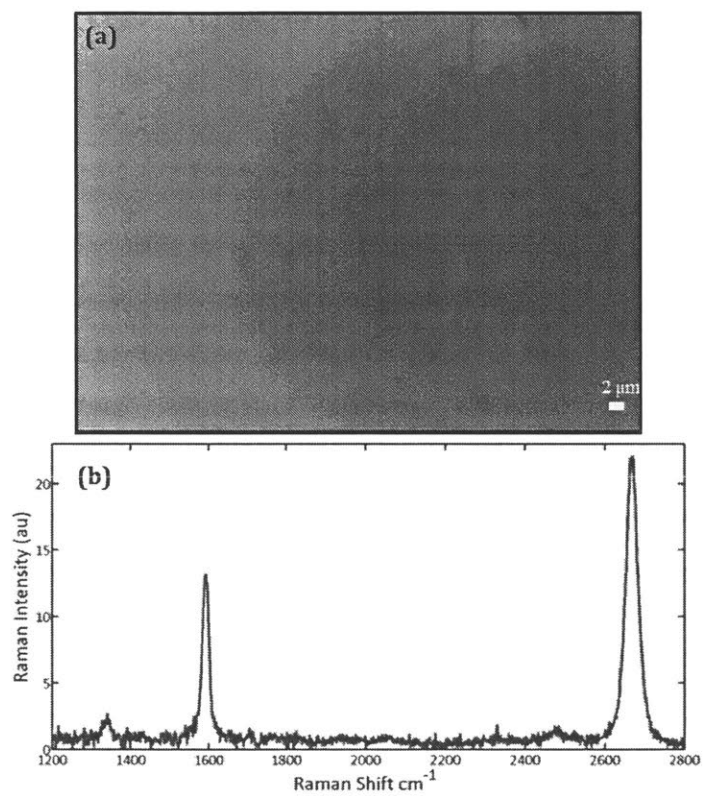
Figure 1-3: (a) Optical image of graphene transferred to SiO2 (300nm) on Si wafer, and (b) representative Raman spectrum of an as-grown film showing formation of monolayer graphene.

emergence of a strong defect peak in the Raman spectrum (Figure 1-4). Carrier mobilities as low as 10 cm^2 V^{-1} s^{-1} have been reported for films of unquantified but nearly saturated H content [21], a four order of magnitude drop compared to pristine graphene.

However, graphite is not the only layered material to exist in nature. Shortly after their discovery of graphene, Novoselov and coworkers applied the scotch tape method they had developed for producing single sheets of graphite to the layered crystals of BN, MoS_2 , $NbSe_2$, $Bi_2Sr_2CaCu_2O_x$ [29]. Two of these materials, MoS_2 and $NbSe_2$ fall into a class of materials know as transition metal dichalcogenides (TMDs). In recent years, single and few layer structures of TMDs have gained significant interest for optical and electronic applications. Working with mechanically exfoliated MoS_2 , Mak [30] and Splendiani [31] demonstrated both a large and variable band gap with the number of layers of material. Specifically, a transition from an indirect gap in the many layered material to a direct gap in single or few layer material – both of which are common to the TMD system. Figure 1-5 shows photoluminescence (PL) and absorption data for mechanically exfoliated MoS_2 [30]. As shown in figure 1-5a, PL is severely quenched for bilayer (as well as thicker) samples. This implies an indirect (1.3 ev) to direct (1.9 eV) band gap transition as the material becomes single layer. This is supported by the observation of a weak PL signal at lower energies in multilayer MoS_2 corresponding to the smaller indirect gap in those samples (Figure 1-5b). The lowest energy PL signal is plotted for all the samples showing a trend towards the bulk indirect gap of MoS_2 (Figure 1-5c), and the absorption spectra show strong optical absorptions corresponding to the 1.9 eV direct gap present in both single and bilayer samples. This indirect to direct transition has also been verified computationally using both DFT [31], G_0W_0, and $scGW_0$ [32].

The following year, Radisavljevic and coworkers [33] reported single layer transistors with carrier mobility in excess of 200 $cm^2V^{-1}s^{-1}$. The 1.9 eV band gap of monolayer MoS_2 allowed them to realize an on/off ratio of greater than 10^7 without modification of the bonding in the material (Figure 1-6; a large on/off ratio is critical for meeting low energy and cooling requirements for chipsets). TMDs also show
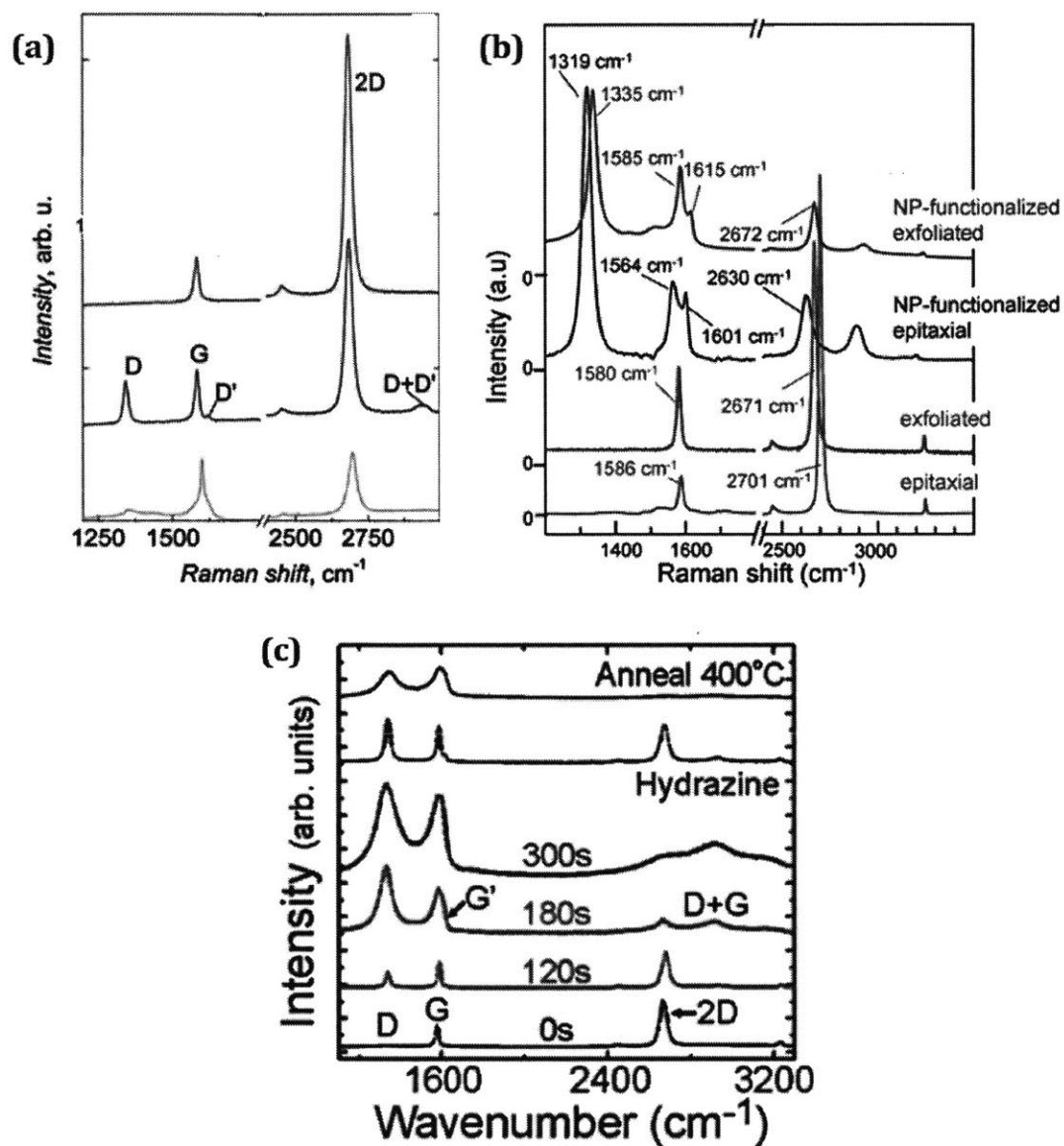
Figure 1-4: Raman spectra for (a) H, (b) nitrophenyl (NP), and (c) F, functionalized graphene sheets. For H, red, blue, and green curves correspond to pristine, hydrogenated, and annealed after hydrogenation (450 °C for 24 hours in Ar) samples. Reproduced from reference [21]. (b) contains data for both graphene grown epitaxially on SiC and exfoliated from graphite. Reproduced from reference [28]. (c) shows spectra after different durations of exposure to XeF2 at 30 °C while on SiO2 as well as those subsequently thermally or hydrazine vapor annealed. Reproduced from reference [24]. Spectra have been displaced vertically for clarity.
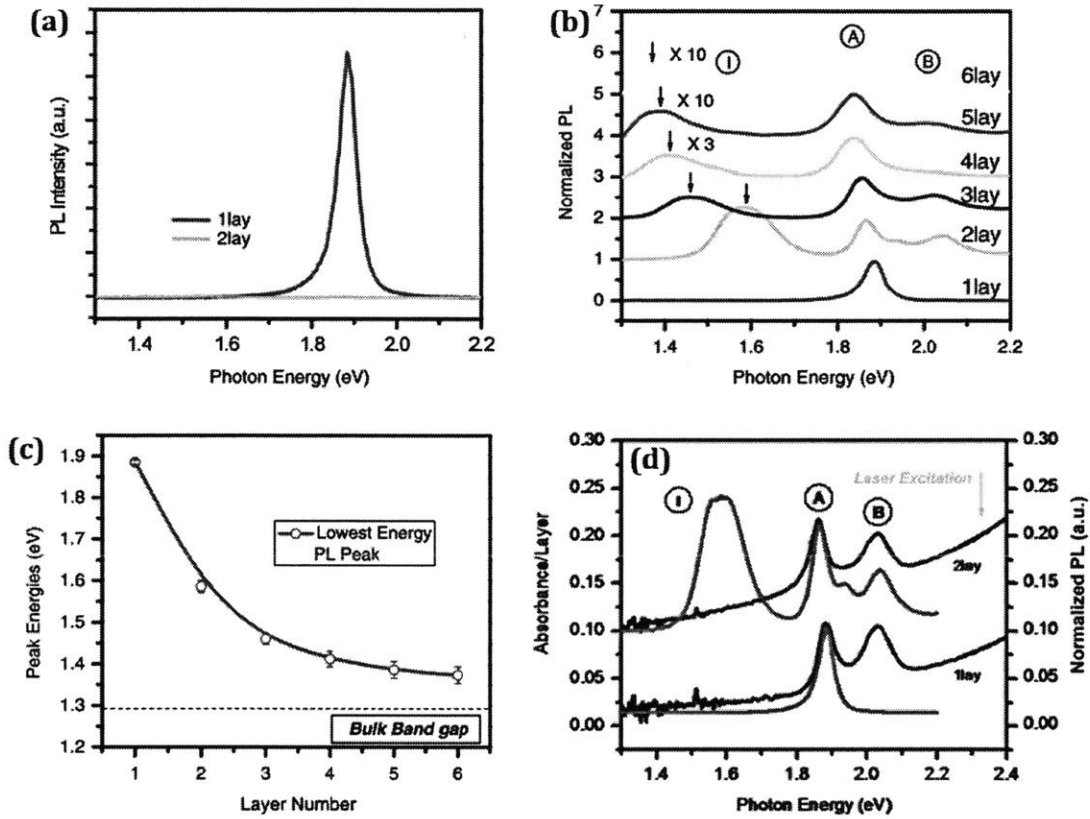
Figure 1-5: Optical properties of single layer MoS_2. (a) PL spectra for mono and bilayer samples. (b) Normalized PL spectra for samples up to 6 layers in thickness. The I feature has been magnified for some samples as labeled. The lowest PL feature has been plotted as a function of layer number in (c) showing the trend towards the bulk MoS_2 band gap. (d) Absorbance spectra (black) with superimposed normalized PL spectra (red) for single and bilayer samples. Spectra displaced on the vertical axis for clarity in (b) and (d). Reproduced from reference [30].

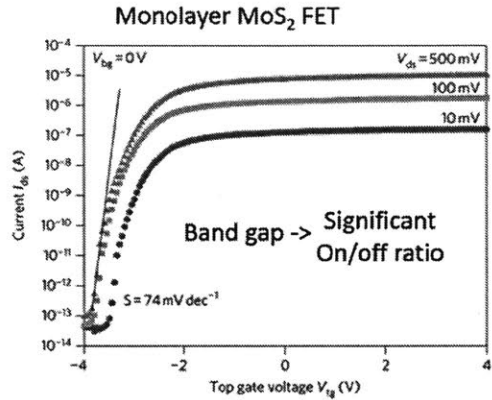Figure 1-6: Source drain current as a function of top gate bias for monolayer MoS_2 field effect transitor fabricated by Radisavljevic et al [33].

different electronic doping depending on preparation method, substrate properties, annealing conditions, and deposition environment adding further tunability to the electrical properites [33, 34, 35, 36, 37, 38, 39]. While these materials are of interested for a variety of applications[40] ranging from valleytronics[41, 42] to catalysis, perhaps one of the most exciting applications of these materials is to PV. Bernardi et al. [43] (Figure 1-7), calculated that single sheets of TMDs are capable of absorbing in excess of an order of magnitude more light than an equivalent thickness of Si, P3HT, or GaAs, making them extremely promising for ultrathin, flexible PV.

While many exciting phenomena have been demonstrated, it has mostly been limited to mechanically exfoliated small area flakes, or in the case of PV applications [44, 45] thick (50 nm) flakes which do not benefit from the electrical and optical phenomena emergent in few layer materials. In order to reap the benefits of the unique properties of TMDs on a device scale, large area and high quality growth methods are needed. While a variety of work has been done to develop such a method, all of the current approaches fall short of meeting this need. Most work has focused on MoS_2 , but even here techniques are limited. Many CVD grown films have poor control over the number of layers [37, 39], have not been used to grow single layer films [46], or are limited to growth on side walls of cleaved wafers [47]. Significant success has been had with an epitaxial approach restricted to Mica substrates which
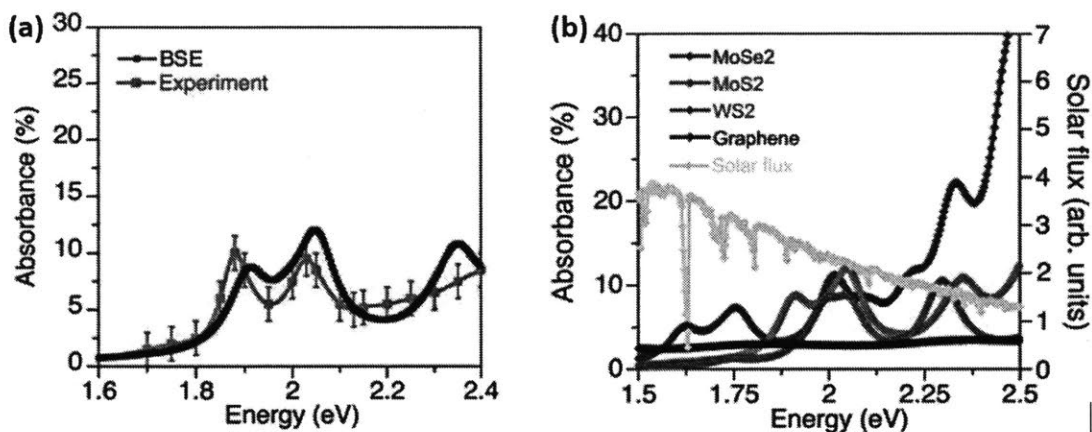
20

Figure 1-7: (a) Absorption spectra for single layer MoS$_2$ measured [30] (red) and calculated using the Bethe Salpeter Equation [43] (black). (b) Calculated absorption spectra for several 2D monolayers and the AM1.5 solar spectrum (yellow). Reproduced from reference [43].

has been shown to produce continuous films but also some undesirable nanotube or fullerene material on the surface of the films [47]. Although excellent progress has been made, as demand for higher quality and more controlled TMD heterostructures grows, further advances in CVD processing are necessary.

Because of its excellent controlled deposition of uniform ultrathin films, ALD is an ideal intriguing alternative growth method of large-area TMD films of specific layer number. Such a growth could be accomplished by two different approaches analogous to the two most studied growth methods currently developed. In the direct chemical vapor deposition approach [37, 47, 48, 49], sulfur vapor from a heated solid sulfur source or gaseous H$_2$S is passed over a transition metal oxide such as MoO$_3$ and a growth substrate. The sulfur containing vapor reduces some of the metal oxide and the resulting gaseous species react to deposit the TMD onto the substrate. In an much more controlled and uniform ALD approach, H$_2$S, H$_2$Se, or similar gas and a metal containing species could be used to deposit the TMD. Bulk thickness materials have already been grown using Mo(CO)$_6$ [50] and WF$_6$ [51] reacted with H$_2$S, but such methods have not been applied to ultrathin materials.

In the conventional alternative approach, a thin film of the pure transition metal [39, 45, 46] or metal oxide [52] is deposited by thermal or e-beam evaporation on the

21

substrate and then it is directly exposed to a sulfur containing vapor to produce the TMD. Rather than using a much less uniform, non-conformal evaporative deposition with limited control over the thickness of the metal film, large area films of metal could be deposited by ALD and then subsequently sulfurized. By depositing an appropriate thickness of metal, the number of layers of resulting TMD could be controlled.

Besides improving the quality and uniformity of the films, a shift from CVD to ALD allow access to a number of exciting device architectures. Films could be deposited on nearly arbitrary substrates without the need for polymer based transfer methods which inevitably introduce tearing and polymer and solvent residues. The discretized nature of the growth and availability of a broad range of candidate reactants, would allow for easy sequential deposition of different TMD materials.

ALD has been used to deposit extremely uniform and thin oxide films to generate large area layer control by Song and coworkers for WS_2 [53], MoS_2 and $W_xMo_{1-x}S_2$ alloys [54] (Figure 1-8). However, given how promising this approach is, it is surprising that it has not received much greater attention. This is in part because the oxide deposition must be so well controlled. A detailed understanding of the specific deposition conditions is required to accelerate nucleation such that film coalescence occurs at a thinner film than the amount required for a monolayer of MoS_2 . This requirement is challenging even with the highly reactive precursors used for oxide synthesis[55] due to the extreme thinness of monolayer MoS_2 . The results from previous work [54] show promising results using $Mo(CO)_6$ and oxygen plasma enhanced ALD (PEALD) and sulfurization with H_2S. While this method clearly shows significant promise for large area, well controlled growth, the factors which control the nucleation regime and thus the thinnest possible coalesced oxide film are still not yet completely understood hence limiting the applicability of this method for ultimate commercial fabrication of MoS_2 and other TMDs.
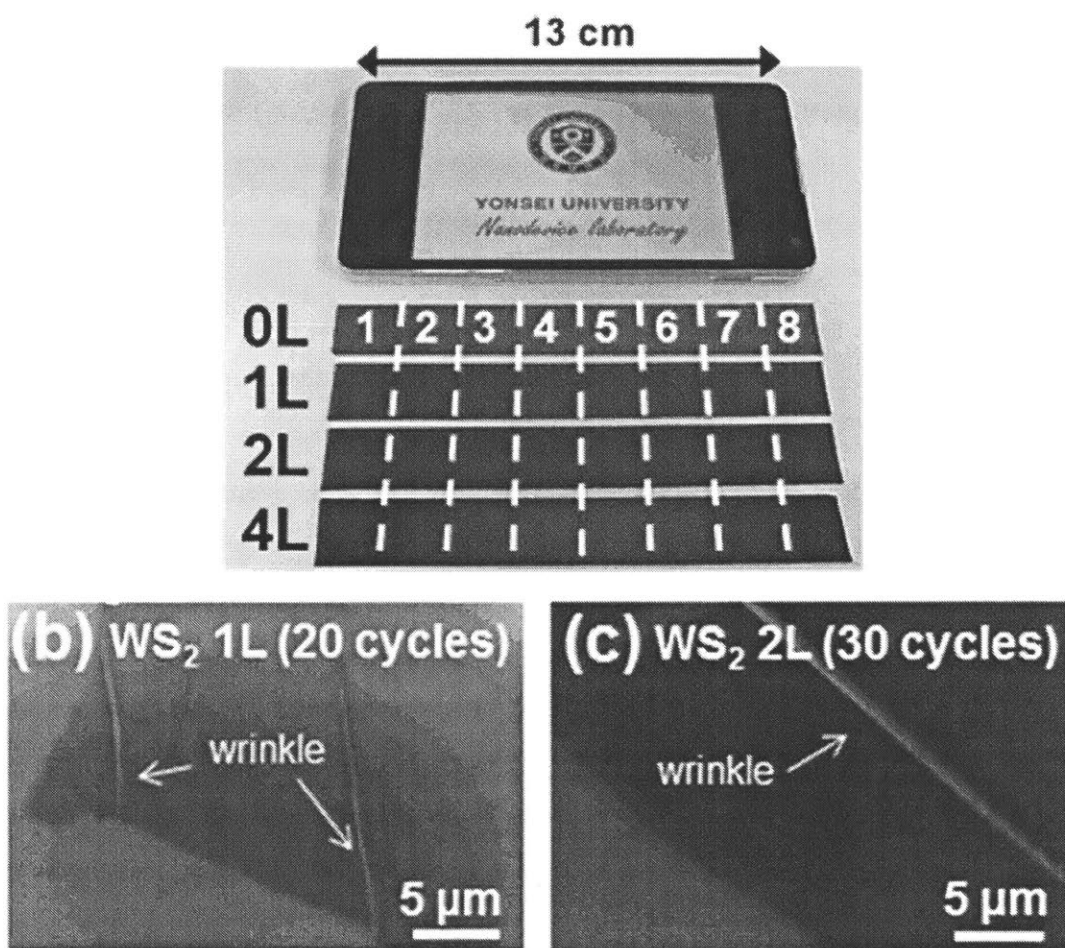
Figure 1-8: Large area, clean, highly uniform, WS_2 films prepared by sulfurization of WoO_3 deposited by ALD. The photograph (a) shows the large area uniformity of the films with increasing number of ALD cycles. (b) and (c) show optical microcsopy images of the films after transfer to a new substrate. Reproduced from [53].

Chapter 2

Thin Films of Coal Nanoparticles

2.1 Introduction

Carbon has long been known as one of the most chemically versatile elements. As a result, carbonaceous materials have been of technological interest for their wide range of electronic properties resulting in materials ranging from low cost conducting materials such as graphite and carbon black, to semiconducting fullerenes and carbon nanotubes, and to insulating diamond and diamond-like carbon. Specifically, carbon black, carbon filaments, and other carbon materials are used in electrodes, conductivity additives, and electromagnetic reflectors[56]. Graphitic materials[57] and amorphous carbon (a-C)[58, 59] are the leading and a promising candidate, respectively, for anode materials in lithium ion batteries. a-C has also been used in the manufacturing of transistors[60, 61] and photovoltaic devices[62, 63], and nanostructured graphitic materials (such as graphene and reduced graphene oxide) have gained significant attention for applications including in photovoltaics[?, 64, 65], transparent conductive membranes[66, 67, 68, 12, 69], and Joule heating devices[70, 71, 72].

Despite decades of research on synthetically processed carbon materials, facile, tunable, low-temperature, solution processing methods remain elusive. Carbon black synthesis requires temperatures as high as 2000 $°C$[73] and a-C is typically deposited by plasma enhanced chemical vapor deposition (CVD)[74, 75] although aerosol assisted CVD has recently been demonstrated[63]. While extensive research has been

conducted to develop solution based methods of graphene deposition, rGO films remain several orders of magnitude less conductive than CVD graphene[69, 76, 77].

In contrast to the widely studied world of synthetic carbonaceous materials, the optical and electronic properties (and corresponding range of tunability) of natural carbonaceous materials are still poorly understood. Yet, this gap in understanding is worth bridging, particularly given the massive global availability of low cost naturally formed carbonaceous materials (for example, nearly 8 gigatonnes per year of coal is produced globally at at $\sim$0.05 $/ kg)[78]. Such materials may find uses beyond combustion, in many of the applications in which synthetic carbon materials are currently being deployed. Due to the wide array of molecular compounds present in different natural carbonaceous materials (from aromatic to aliphatic, with a varying degree of functional chemistry)[79], these materials could provide a broad range of electrical properties at extremely low cost. In order to unlock the potential of these materials, it is crucial to develop compatible, low cost methods of processing them, characterize the nanostructure of such processed films, and measure their optical and electrical properties including a detailed understating of the dominant charge transport mechanisms. To date, electrical conductivity has been measured in coals and coal char, but solely for the purpose of correlating in situ conductivity measurements to fuel processing as part of underground coal gasification programs[80, 81].

In this work [82], we present a method for solution processing sub-100 nm natural carbon particles from standard coal sources to obtain 100 nm thick coal films and characterize their microstructure by scanning electron microscopy (SEM). We relate the carbon bonding configuration (characterized with Raman spectroscopy) to the conductivity, optical absorption properties, and the dominant charge transport mechanism, through variable temperature (50 K to room temperature) current-voltage measurements. Finally, annealing of these films up to temperatures as high as 950 $°C$ was explored as a method for further tailoring the properties of natural carbon films beyond the precursor chemical phase space. We show this simple annealing process leads to a direct modification of the (sp^2) content and aromatic domain size, which allows for the film electrical conductivity to vary over 7 orders of magnitude.

2.2 Preparation of Coal Nano Particles

Figure 2-1 illustrates the approach taken to produce thin films of natural carbon (for experimental details see chapter 6). As received coal powders were ball milled for up to 106 hours. Over this extended milling period, particle size continued to decrease (Figure 2-2). Dilutions of the resulting material were centrifuged to select smaller particles less than 100 nm in diameter from the dispersion (Figure 2-1c), and spin coating was used to then prepare thin films for device fabrication from the supernatant (Figure 2-1d). The milling and centrifugation process did not cause changes in the carbon hybridization chemistry or bonding structure as determined by both x-ray photoelectron spectroscopy (XPS) and Raman spectroscopy (Figure 2-3 and 2-4). Thus this method can be applied to the majority of the natural carbon materials to produce thin films without narrowing the resulting thin film chemistries. Ball milling offers a solution processing approach for the application of the entire coal phase space studied to thin film devices. Material was processed both in air and under nitrogen with no differences observed. Particle suspensions were stored in isopropanol under air for as long as a year with no chemical changes as measured by Raman and XPS.

In order to use natural carbonaceous materials in electrical applications, the morphology of the thin films must be understood as it plays a critical role in carrier mobility and extraction, as well as separation and surface recombination in many applications. While milling was shown to preserve the starting carbon hybridization chemistry and bonding structure for each coal, different coals showed widely varying morphologies after ball milling and after spin coating. The four coals studied in order of increasing rank, or degree of maturation, were Department of Energy Coal Sample (DECS) 25 (lignite A), DECS 31 (high volatile A bituminous - hvAb), DECS 19 (low volatile bituminous), and DECS 21 (anthracite)[83]. The particle size distribution after milling varied across the coals studied (Figure 2-5). In particular, a significant portion of large (5-10 μm) particles remains in the anthracite suspension, although all suspensions include numerous sub 100 nm particles. Following centrifugation, these smaller particles can be selected from the suspensions, with the colloidal stability
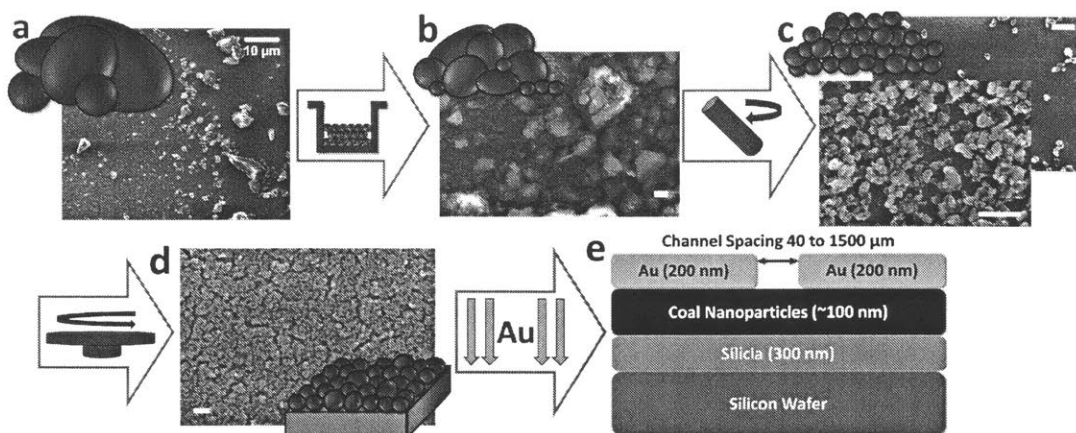
Figure 2-1: Preparation of organic thin films from naturally sourced carbon. As received powders, a, were first milled in a stainless steel ball mill to produce a broad distribution of particle size, b. Sub 100 nm size particles were then selected by centrifugation, c, and spin coating was used to produce thin films, d. e, Thermal evaporation of gold was used to deposit electrical contacts with shadow masking used to define channels ranging from 40 to 1500 μm. All scale bars are 300 nm unless otherwise specified.

also varying across the coals (Figure 2-6). While sub 100 nm dispersions could be achieved with any of the coals through appropriate choice of centrifugation speed and duration, the hvAb produced the thin films with the most uniform thickness and only moderate cracking of the film (Figure 2-1d) when isopropanol was used as a solvent.

Tunability across a broad phase space is critical for tailoring a material to a specific application. To develop a direct method of modifying the properties of a film beyond the choice of a starting coal, annealing at elevated temperature under argon gas was also performed. The less mature the coal (i.e. the higher the aliphatic content), the earlier the onset of thermal decomposition (Thermogravimetric (TGA) analysis, Figure 2-7a) – as has been observed elsewhere[84]. Temperatures as low as $300\,°C$ were observed to impact the properties of hvAb, and even quite mature coals experience chemical changes at sufficiently high temperatures. Scanning electron micrographs of hvAb and anthracite films at several annealing temperatures (Figures 2-7b and 2-7c), show that annealing causes sintering of the particles and amplification of cracks in the films. However, the morphology remains consistent above $450\,°C$. Due to the smaller
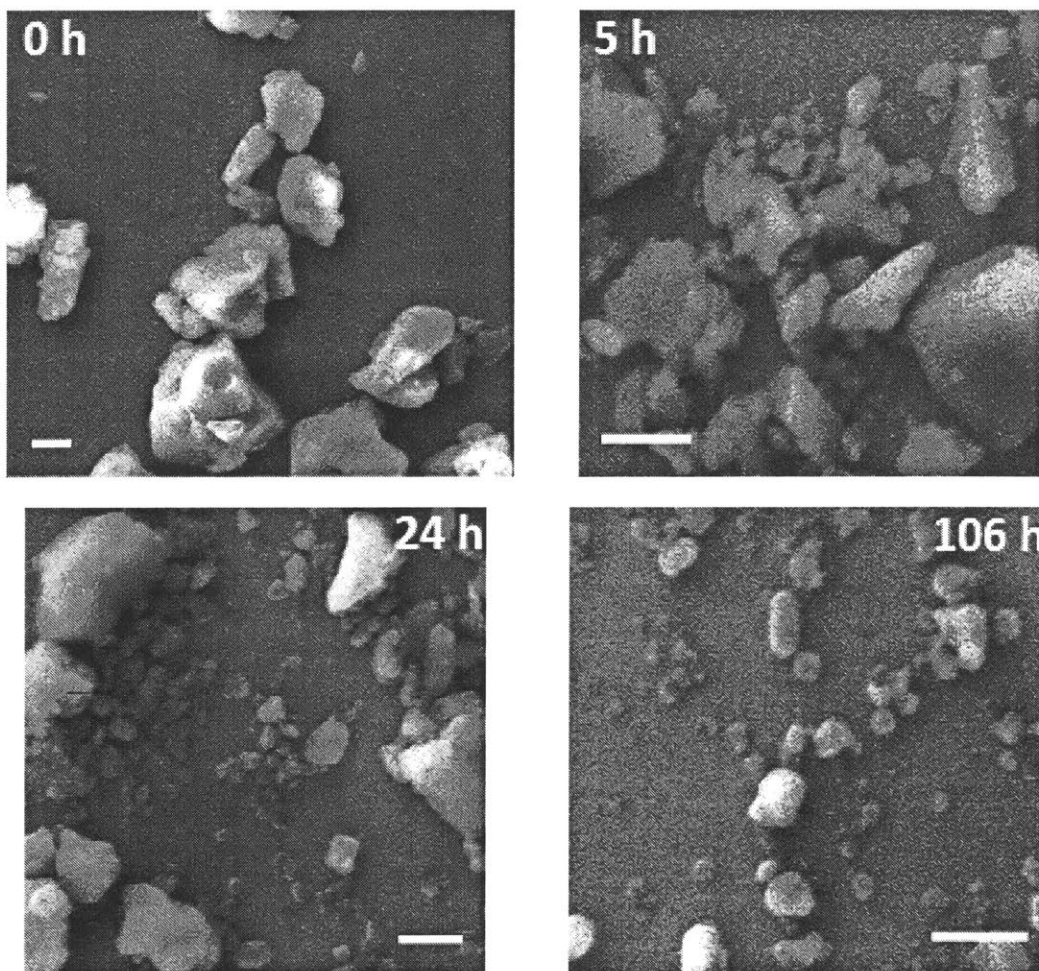
Figure 2-2: Evolution of particle sizes with milling time. SEM images of low volatile bituminous coal (lvB) after 0, 5, 24, and 106 hours of milling. As the milling proceeds, the number of sub 100 nm particles increases and largest particles are consumed. Further milling may produce a higher yield of particles in the 10's of nm regime. All scale bars represent 500 nm.
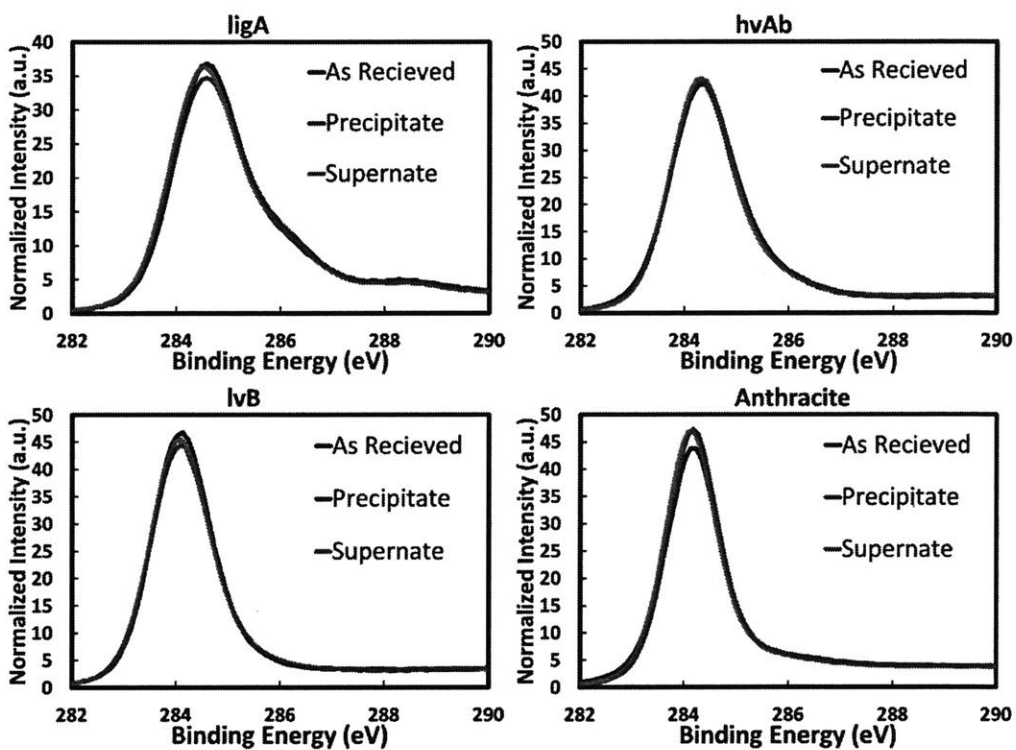
Figure 2-3: XPS spectra across processed coals. Carbon 1s XPS spectra of coal films produced from as received coals as well as both the precipitate (larger particles) and supernatant (smaller particles) following milling and centrifugation. The close agreement between all spectra of material from the same coal illustrates the fidelity of the process to the natural carbon chemistry.
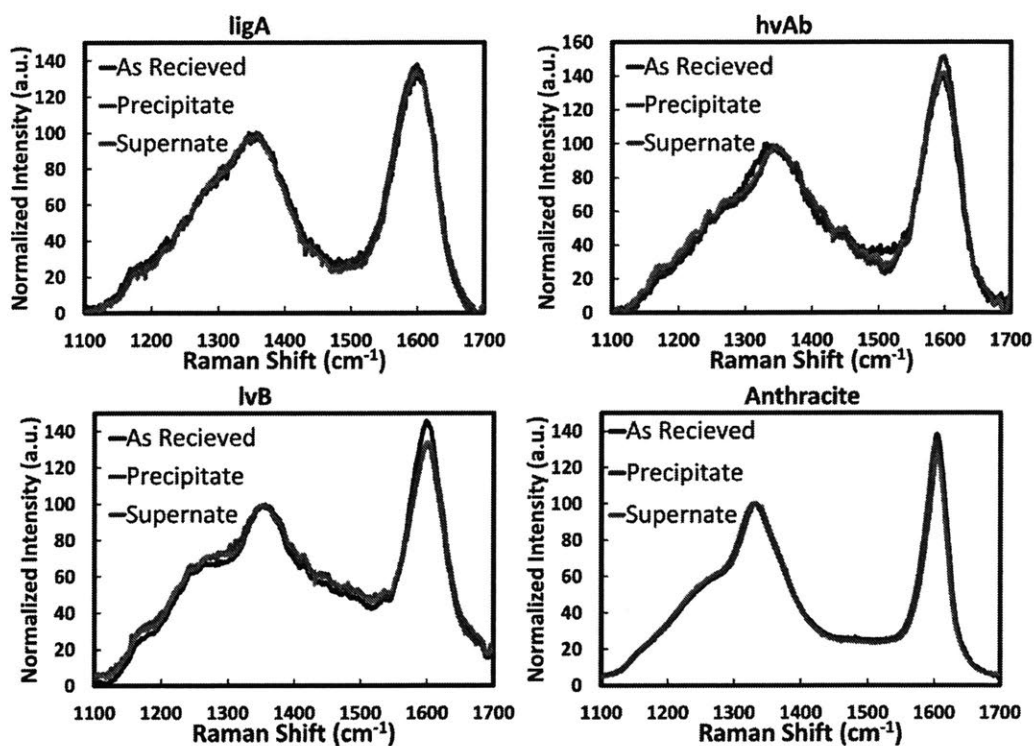
Figure 2-4: Raman spectra across processed coals. Raman spectra of coal films produced from as received coals as well as both the precipitate (larger particles) and supernatant (smaller particles) following milling and centrifugation. The close agreement between all spectra of material from the same coal illustrates the fidelity of the process to the natural carbon chemistry.
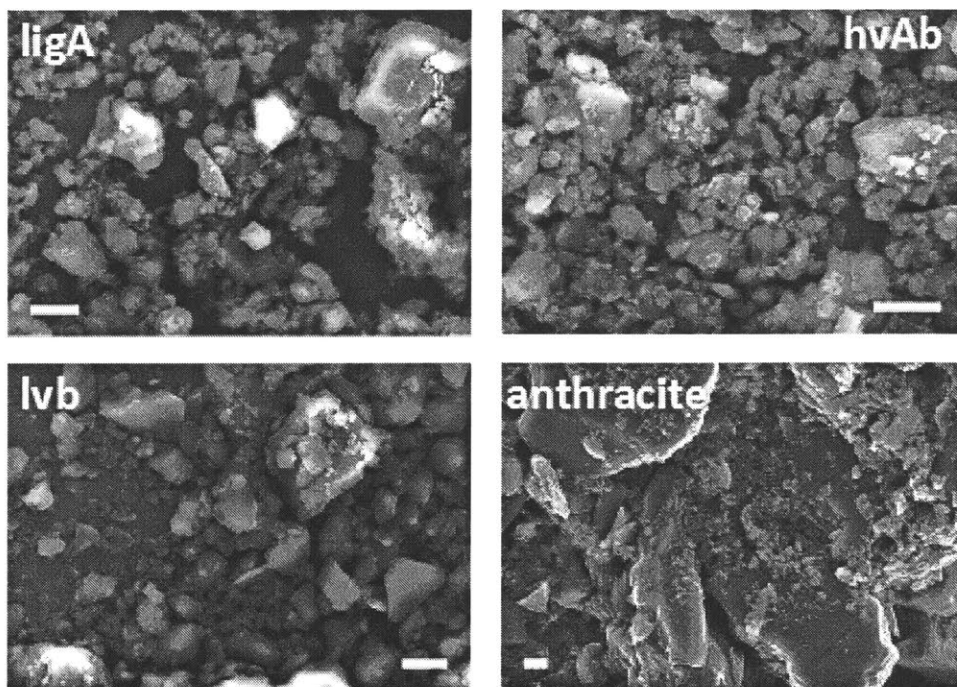
Figure 2-5: Particle differences between coals after milling. SEM images showing a comparison of effects of 100 hours of ball milling on the four coals studied. After milling, the anthracite had far more >1 µm particles, and in general, the product of milling was found to be sensitive to the specific coal chemistry. All scale bars represent 500 nm.
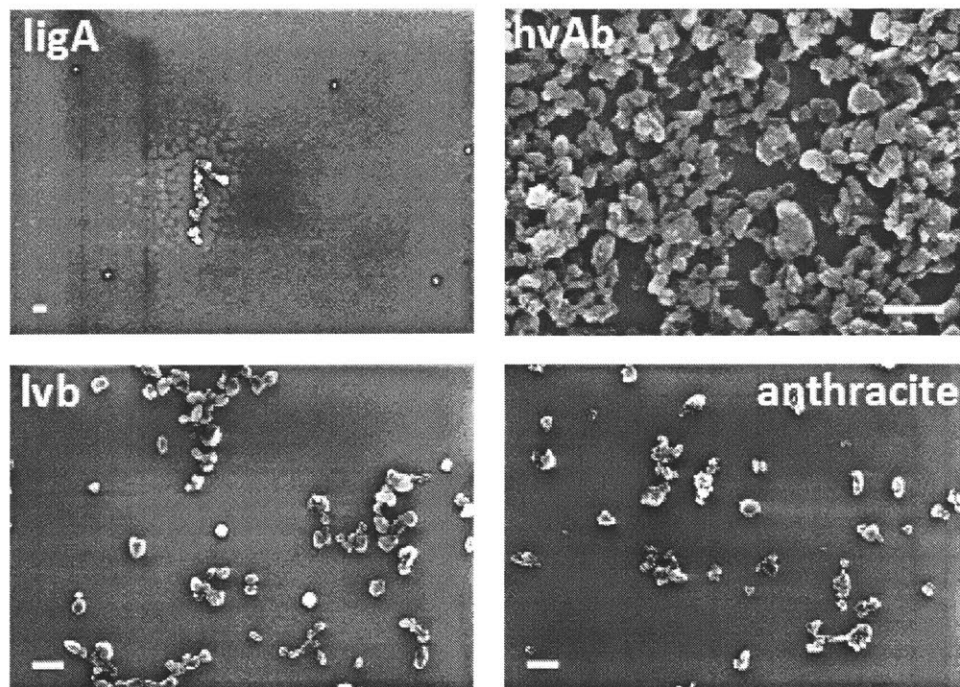
Figure 2-6: Particle differences between coals after centrifugation. SEM images of particles spun cast on silicon wafers after 8 hours of centrifugation at 3500 rpm. The hvAb nanoparticles were particularly stable in isopropanol, producing the highest concentrations of particles after centrifugation. In contrast, ligA is particularly unstable and very few particles remain in the supernatant (such as the cluster imaged). Such clusters of ligA possibly result from material dislodged from the precipitate during decanting. All scale bars represent 200 nm.

Figure 2-7: Morphological effects of thermal processing of coal thin films. a, Differential TGA showing the temperatures at which decomposition peaks occur in each coal. All coals show a low rate of decomposition rate by 900 °C with younger coals (as determined by mean VRO)[83] showing primary mass loss at lower temperatures. Representative SEM images of hvAb, b, and anthracite, c, nanoparticle films after annealing at several temperatures showing both extensive ma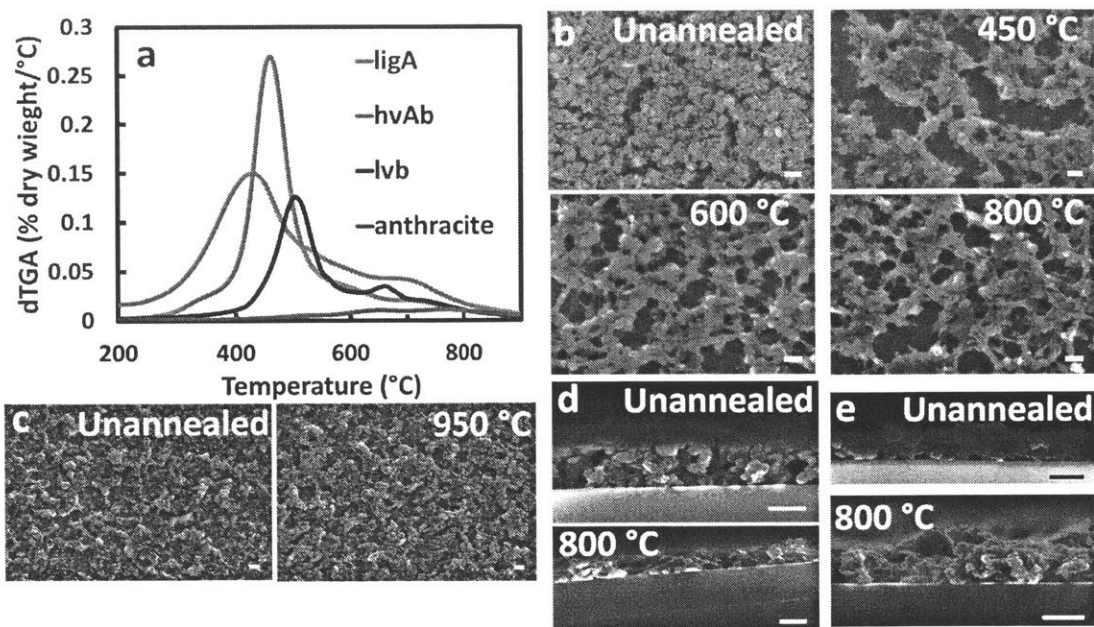ss loss and sintering of the hvAb particles between room temperature and 600 °C. Due to much lower mass loss, the anthracite films show little morphological change. Cross sectional SEM of hvAb, d, and anthracite, e, showing the thickness of films before and after 800 °C annealing. All scale bars 200 nm.

mass loss in the higher rank anthracite, the morphological changes from annealing are less pronounced than in hvAb. It is important to note that the temperatures used remain much lower than those used for production of materials such as carbon black. Furthermore, the tunable electronic properties achieved through annealing are also achievable using a lower temperature annealed or un-annealed precursor coal of different rank, as will be shown below.

2.3 Chemical Characterization

Beyond understanding the nanoscale morphology, natural carbon materials must also be characterized at the level of chemical functionalities, and the impact on the optical properties, electrical conductivity, and carrier transport understood. The characterization of the type of carbon chemistries present in any given film is critical to identifying the appropriate coal material for applications ranging from battery anodes, where specific binding is needed, to transistors and photovoltaics, where electronic state traps associated with specific chemical structures can control device performance. Raman spectra (Figure 2-8) of hvAb and anthracite films at several annealing temperatures provide insight into the changes in the carbon bonding structure. Above 450 °C, the ratio of peak heights of the D and G Raman bands (I_D/I_G) steadily increases indicating increasing sp^2 cluster size in the 0.5 to 2 nm regime (Figure 2-8e) as shown previously in a-C[85, 86], graphite[87], and graphene[88, 89]. There is also a progressive decrease in the intensity of the D shoulder band from 1150 to 1300 cm^{-1} (Figure 2-8b and 2-8d) which corresponds to decreasing aliphatics[90]. Anthracite, which has a higher (sp^2) content before annealing, shows minimal change in the sp^2 bonding network as determined by Raman spectroscopy up to 450 °C (Figure 2-8c). However, annealing at 950 °C causes similar changes to those observed in hvAb as well as broadening of the G-peak indicating an increase in the variety and disorder of (sp^2) domains[85] which was more modest in hvAb due to a larger initial G peak width. In contrast to the physical morphology of the films (Figure 2-7) in which anthracite is observed to undergo a much smaller transformation than hvAb, both coals show similar changes in the carbon bonding configuration for the highest annealing temperatures. Thus, we conclude that annealing up to approximately 600 °C results in a large reduction in aliphatics and a modest increase in sp^2 localization length and disorder. However, annealing between approximately 600 and 950 °C causes a dramatic increase in carbon bond disorder and a rapid conversion to a aromatic rich a-C structure with increasing domain size at higher temperature.

The optical energy bandgap is a critical property for design of light absorbing or
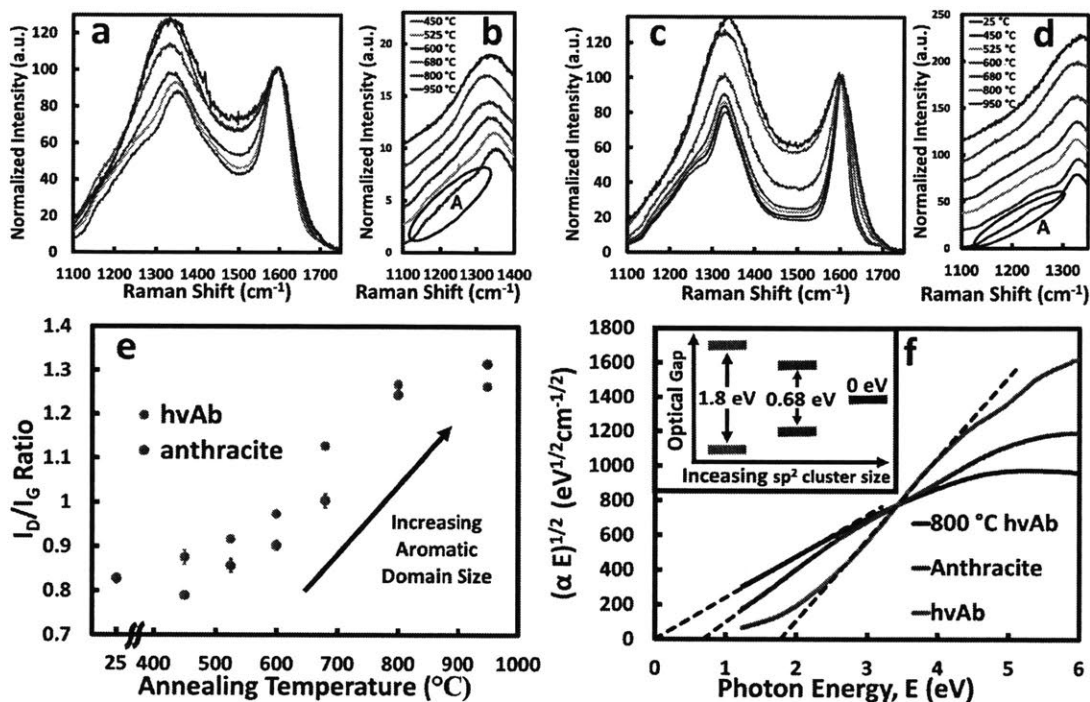
Figure 2-8: Tunability of chemical structure in coal films. Raman spectra (normalized by the G peak maximum) of hvAb, a-b, and anthracite, c-d, nanoparticle films after different annealing conditions. Annealing shows a clear increase in the I_D/I_G ratio and broadening of the G peak, indicative of increasing disorder in sp^2 domains. D shoulder band regions of hvAb, b, and anthracite, d, corresponding to reduced hydrogen content, specifically the loss of the shoulder peak, A (circled for lowest temperature). e, Plot of the ratio D peak maximum to G complex maximum suggesting a steady increase in the relative aromatic content of the films in the 0.5 to 2 nm aromatic domain size regime. Error bars represent standard errors based on at least 3 measurements in different regions of the film. f, Plot of the square root of the product of the absorbance (α) and photon energy (E) as a function of photon energy as determined by optical absorption spectroscopy. The x-intercepts of the fits of the linear regions (dashed lines) give the values of the optical bad gap. The inset shows a schematic of the optical gaps calculated for hvAb, anthracite, and 800 °C annealed hvAb films arranged by increasing sp^2 cluster size.

36

emitting devices, such as photovoltaics or photosensors. To demonstrate the variation of the optical bandgaps across the natural carbon phase space and its modification with thermal processing, optical absorption spectroscopy was performed. Using the method developed by Tauc et al.[91] to determine the value of an optical bandgap, a function of the product of the absorbance (α) and the photon energy (E) may be plotted as a function of photon energy and the x-intercept of a fit of the linear region gives the value of the optical band gap (Figure 2-8f). Because slightly different treatments of the density of states and matrix elements gives rise to different functional forms of to be plotted on the ordinate[92], we have used the square root of the product of the absorbance and the photon energy, ($\alpha E^{1/2}$), as it is appropriate for the electrical states of a-C and hydrogenated amorphous carbon (a-C:H)[74] and fits the data reported here well. This optical gap is associated with to * band transitions in the aromatic domains, and we report values of 0.68 eV in anthracite and 1.8 eV in hvAb films. Furthermore, thermal annealing of hvAb at 800 °C reduced the optical gap to 0 eV. This underscores the chemical and optical tunability as the choice of coal varies the optical gap of the aromatic domains from 1.8 eV to 0.68 eV, and thermal processing allows for extension of the aromatic domain size until elimination of the optical gap.

The aromatic domain cluster size can be estimated from the optical gap based on the approach developed by Robertson et al [93, 94]. Robertson used a Hückel model with the nearest neighbor interaction energy of graphite ($\beta = -2.9eV$) to determine the band gap of systems of 6-membered aromatic rings in both compact and linear arrangements. The energy gaps calculated by this method trend with the number of rings, M, as $E_g = 5.8/M^{1/2}eV$ in the compact case and $E_g = 60/(M + 2.16)^2eV$ in the linear case. Assuming a compact arrangement, the values of the optical gaps reported correspond to sp^2 domains 0.9 nm in diameter (10 rings) in the hvAb and 2.2 nm in diameter (70 rings) in the anthracite which is in good agreement with the I_D/I_G Raman peak ratios discussed earlier (Figure 2-8e), [85, 86, 87, 88, 89].

2.4 Device Characterization

To quantify the effect of the tunable chemical structure observed through Raman and absorption spectroscopies on electrical performance, gold contacts were evaporated onto hvAb and anthracite films including those annealed at several temperatures. The current voltage relationship was found to be linear for all devices (Figure 2-9a). The conductance also varied with contact spacing (L) indicating that contact resistance is not dominant. By plotting the conductance of the film (σ) per contact width (w) as a function of the inverse of the distance between the contacts ($\sigma/wt = \sigma_0/L$), the conductivity of the films can be determined under an assumption of uniform contact resistance (Figure 2-9b). Uniform film thicknesses (t) of 100 nm were assumed (Figure 2-7c and 2-7d). However, conductivity through the films is significantly more circuitous than a direct path between the contacts (Figure 2-7b) and it is also potentially limited by very thin regions of the film. Thus the actual material conductivity is most likely larger than the film conductivity values measured.

In addition to introducing webbing in the film, high temperature annealing also provides an effect of congealing the particles and reducing the resistance of the interface between them (Figure /ref:fig:Coal2). Given the extensive chemical changes which occur in the material as evidenced by the Raman and UV-Vis absorbance spectroscopies, we would expect that while this change could contribute to the variation in conductivity with annealing temperature its effect may be comparatively modest. This congealing of the particles appears nearly complete by 450 °C and complete by 600 °C, but in contrast, we see significant changes in the conductivity above that temperature. We also observe only a modest difference between the conductivity of the as deposited and the 450 °C annealed anthracite. In order to properly and quantitatively decouple the two effects, lower temperature annealing for an extended period of time may prove able to congeal the particles without aggressively tuning the aromatic domain size and other chemical properties.

Without annealing, the hvAb films were not sufficiently conductive for the electrical conductivity to be measured. For hvAb films, measureable conductivity ($> 10^{-6}$
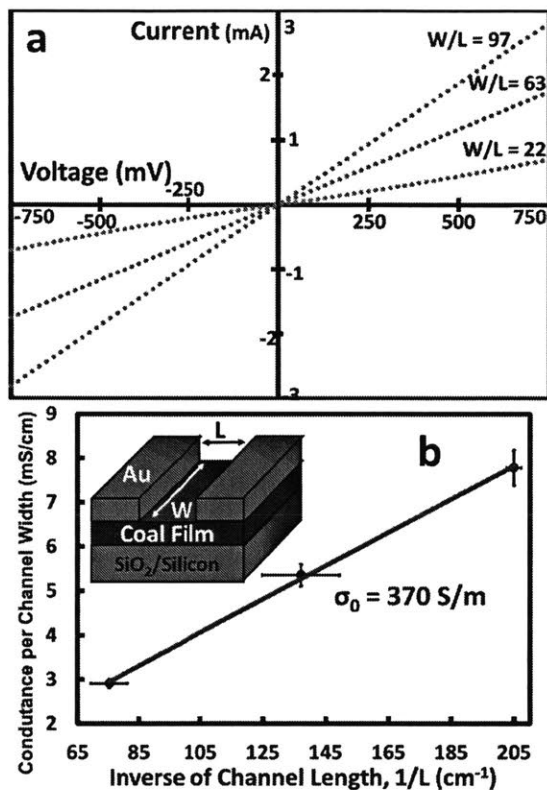
Figure 2-9: Conductivity of coal films. a, Current voltage trace of representative hvAb films annealed at 680 °C showing variation with different channel width to length ratios (w/L) and b, conductance per channel width (σ/w) as a function of the inverse of the contact spacing $(1/L)$ for all devices annealed at 680 °C. The slope of the least squares best fit line gives a conductivity of 370 Sm^{-1}. Error bars represent standard errors over 3 devices.

S/m) was observed for films annealed above 450 °C, where it varied over 7 orders of magnitude before saturation. Figure 2-10a shows the conductivity of these films compared to several synthetic carbon materials under active research. The electrical conductivities observed are broadly tunable over a range of materials such as rGO and a-C by varying the annealing temperature. Films of un-annealed anthracite possess conductivity comparable to that of a 500 °C annealed hvAb film, emphasizing the degree of chemical and therefore property variability of the precursor coals without the need for high temperature annealing. At an annealing temperature of 950 °C, the anthracite shows a transition to conductivity values similar to those of the highest temperature annealed hvAb, in good agreement with the similar (sp^2) localization length (I_D/I_G ratio) observed in both films by Raman spectroscopy.

2.4.1 Charge Transport Mechanism

The optimization of device design relies on the knowledge of electronic transport mechanisms, i.e. what limits the mobility and how carriers move through the material, allowing for a direct link between the bonding structure quantified by Raman and absorption spectroscopies and the wide tunability of electrical conductivity. To characterize this conduction mechanism, conductivity measurements were repeated at temperatures as low as 50 K. The observed trends follow the relationship predicted by variable range hoping in a 3-dimensional material[101], or

$$\sigma \propto e^{-(T_0/T)^{1/4}} \tag{2.1}$$

where σ is the conductivity, T is the temperature, and $k_B T_0$ is the characteristic hopping energy or the average energy spacing near the Fermi level inside a volume defined by the wave function localization length, , or
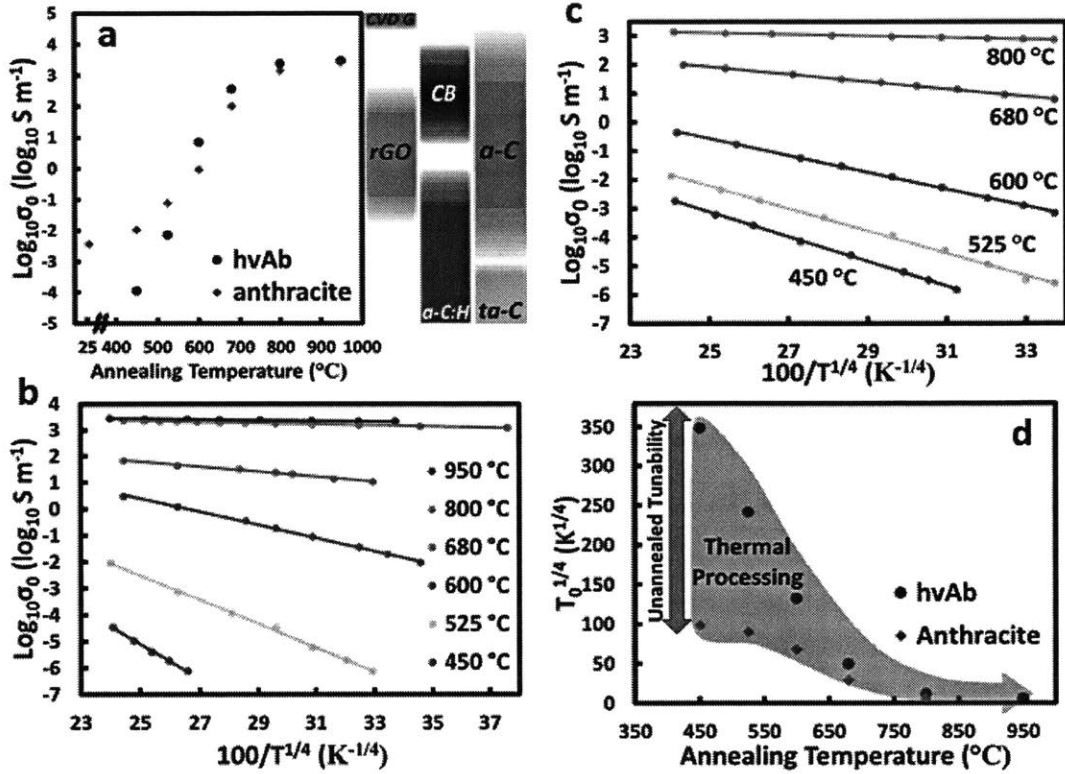
$$T_0 = 1/(k_B \xi^3 N(E_F)) \tag{2.2}$$

40

Figure 2-10: Conductivity and hopping transport in coal thin films. a, Conductivity as determined from slope of σ/w as a function of $1/L$ for several annealing temperatures. By choice of annealing temperature, the conductivity can be tuned over 7 orders of magnitude. Typical range of conductivities reported from some synthetic carbon materials of research and commercial importance are included for reference, specifically, CVD grown graphene (CVD G)[68, 69], rGO films[66, 67], carbon black (CB)[95, 96], hydrogenated amorphous carbon (a-C:H)[97, 98], a-C[97, 99, 100], and tetrahedral amorphous carbon (ta-C)[61, 75]. Plot of the base 10 log of conductivity as a function of $T^{-1/4}$ for hvAb, b, and anthracite, c. Devices annealed at higher temperature show much weaker temperature dependence of conductivity due to an increase in the size and density of aromatic domains. Slope of best fit lines is related to $T_0^{1/4}$. d, Plot of best-fit values of $T_0^{1/4}$ for films annealed at several temperatures. The large difference in $T_0^{1/4}$ values for hvAb and anthracite at low and medium annealing temperatures illustrates the diversity of structures and properties between coals. Annealing results in a conversion towards a minimal $T_0^{1/4}$ value indicating large and closely spaced aromatic domains.

41

where $N(E_F)$ is the density of states at the Fermi level. A plot of $log_{10}(\sigma)$ as a function of $T^{-1/4}$ for the hvAb and anthracite films annealed at several temperatures is shown in Figure 2-10b and 4c, respectively. A linear behavior with a single T_0 value across the temperature range for each sample is observed. For samples annealed at high temperatures, sp^2 domains are spaced closely both in energy and/or physical proximity, which gives rise to a small T_0. The values of $T_0^{1/4}$ are shown in Figure 2-10d as a function of the annealing temperature. The large difference in $T_0^{1/4}$ between the hvAb and anthracite for low and moderate annealing temperatures illustrates the variability in the electronic landscape accessible through the choice of natural carbon source. As the room temperature conductivity approaches saturation after high temperature annealing, the characteristic hopping energies of the two coals converge and approache a minimum. The values here reported are in good agreement with those for single flake rGO devices (20 to 140 $K^1/3$ depending strongly on the degree of reduction)[102, 103] and a-C (from 220 $K^{1/4}$ for $\sigma = 10^{-5}S/m$ to 87 $K^{1/4}$ for $= 100$ S/m)[104, 105]. This demonstrates that in addition to possessing similar chemical properties, including the sp^2 domain size and amount of disorder, these properties result in the same conduction mechanism for the natural sourced carbon material and comparable synthetic materials such as a-C and rGO.

While an understanding of the work function and electrical mobility gap across the natural carbon phase space is needed for fabrication of band engineered devices such as transistors and photovoltaics, the ability to tune the conductivity in excess of 10^3 S/m opens up applications in Joule heating for medical[106, 107], defogging and defrosting[71], lab-on-a-chip[108], and other applications[109]. The low cost and abundance of natural carbon makes it attractive compared to complex materials such as doped tin oxides and singled walled carbon nanotubes. Silver nanowire meshes, while solution processable, typically fail at temperatures ranging from 120 to 200 $°C$[109, 110]. To demonstrate the performance of high conductivity films made with naturally sourced carbon for stable high temperature Joule heaters, anthracite films were deposited onto quartz substrates and annealed at 950 $°C$ (Figure 2-11a). The temperature of the device was measured at biases up to 60 V which results in heating

as high as 285 °C (Figures 2-11b and 2-11c) – well beyond the region of instability of many silver films and comparable or exceeding 1000 °C annealed rGO and graphene based devices under equal bias. The natural carbon films also had similar or better response times (less than 120 s) compared to rGO and graphene devices[71, 72] and improved temperature uniformity across the device[111]. To further demonstrate the durability of the amorphous aromatic network, the films were maintained at 150 and greater than 200 °C for 30 minutes without deterioration in temperature (Figure 2-12).

2.5 Summary

In conclusion, we present a solution-based method of producing thin films of low-cost, widely available, natural carbon which preserves the broad chemical phase space of the starting material. Unlike several synthetic materials where the need for highly pure compositions adds to processing complexity and cost, the heterogeneous nature of natural carbon, with its breadth of chemical functionalities, allows a single parameter, temperature, to carefully tune the optical and electrical properties of the material, in addition to C-H bond content, sp^2 domain size, and disorder. By use of low temperature measurements, hopping transport was shown to govern the properties of the material in a manner comparable to rGO and a-C with a strong dependence on the size of sp^2 domains. Using the broad chemical phase space of coal and simple thermal annealing, the optical gap was shown to vary from 0 to 1.8 eV, and the conductivity was shown to be tunable over 7 orders of magnitude, a range which encapsulates many synthetic carbon materials of active research interest. Finally, the highest conductivity material was leveraged to fabricate Joule heating devices capable of reaching 285 °C without failure.

Recent years have witnessed a surge in scientific interest in the use of carbon materials such as a-C, graphene, and rGO as transparent conductive films, transistors, photovoltaics, and battery anodes. While promising research continues, limitations remain for these materials such as the reduced conductivity of rGO and need for

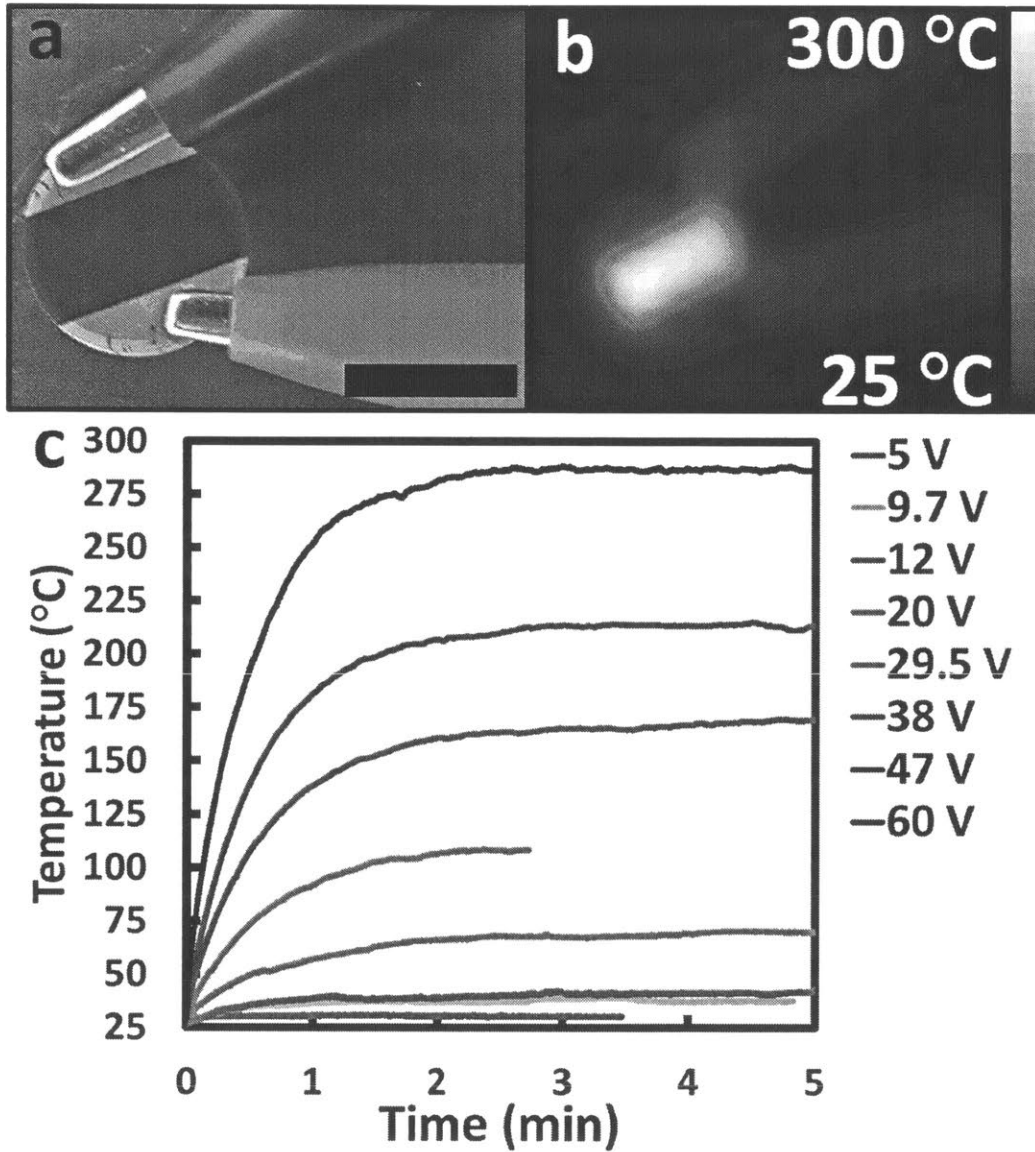Figure 2-11: Joule heating devices fabricated from anthracite a, Optical image of anthracite film on quartz substrate during testing. Scale bar 1 cm. b, Temperature map of device at 60 V bias showing heating to 285 ^{circ}C with good uniformity away from contacts. c, Maximum device temperature as a function of time for a representative device under several bias conditions showing heating response.
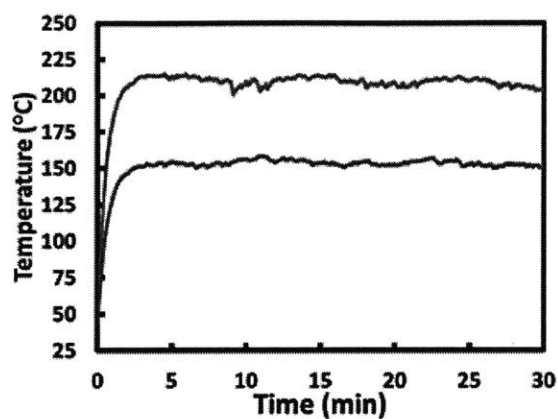
Figure 2-12: Stability of Joule heating devices. Device shown in figure 5 maintained at 150 and >200 °C for 30 min under air. No deterioration in device temperature was observed which indicates little degradation in the film quality or chemistry. Sharp fluctuations (particularly visible in >200 °C trace) are due to instabilities in the supplied voltage.

plasma processing of a-C. Here, we have shown that solution processed thin films of low cost natural carbon such as coal possess a broad range of electrical properties that could be tapped for many of the same applications. Simple processing such as thermal annealing can further tune the chemical structure and electrical properties. Joule heating devices were demonstrated to achieve temperatures beyond many synthetic alternatives and performed as well or better than synthetic carbon devices. More fundamentally, this work shows the built-in chemical diversity of natural carbon provides opportunities in creative and innovative advanced materials applications, beyond its current use – primarily power generation through combustion.

Chapter 3

Electronic Properties of Asphaltene and Vacuum Residuals

3.1 Introduction

While coals are one example of a natural carbon resource, there are many other solid carbon materials which may be used for electronic devices. One such class of materials are asphaltenes. Asphaltenes are the aromatic rich portion of the lowest boiling fraction of crude distillation [112]. They are prepared by precipitation from vacuum distillation residuals by the addition of heptane or other aliphatic solvents. Vacuum distillation is used to separate the bottoms from the first distillation system in crude refining. The bottoms or residuals from that process are a blend of low boiling point organics and some metal contamination. The portion of that material which is insoluble in saturated hydrocarbon solvents are the asphaltenes [112]. Figure 3-1 shows a few model asphaltene structures. Molecules are typically about 750 Da in size with a single fused ring system at their core and short aliphatic chains extending off of it.

Two different vacuum residuals and their asphaltenes were used in this work. Marlim vacuum residual has relatively low metals (200 ppm total and low aromatics/more hydrogen (10.8 wt% H). It contains 10% n-heptane insoluble asphaltenes. A Maya vacuum residual was also used which has high metals (940 ppm) and more
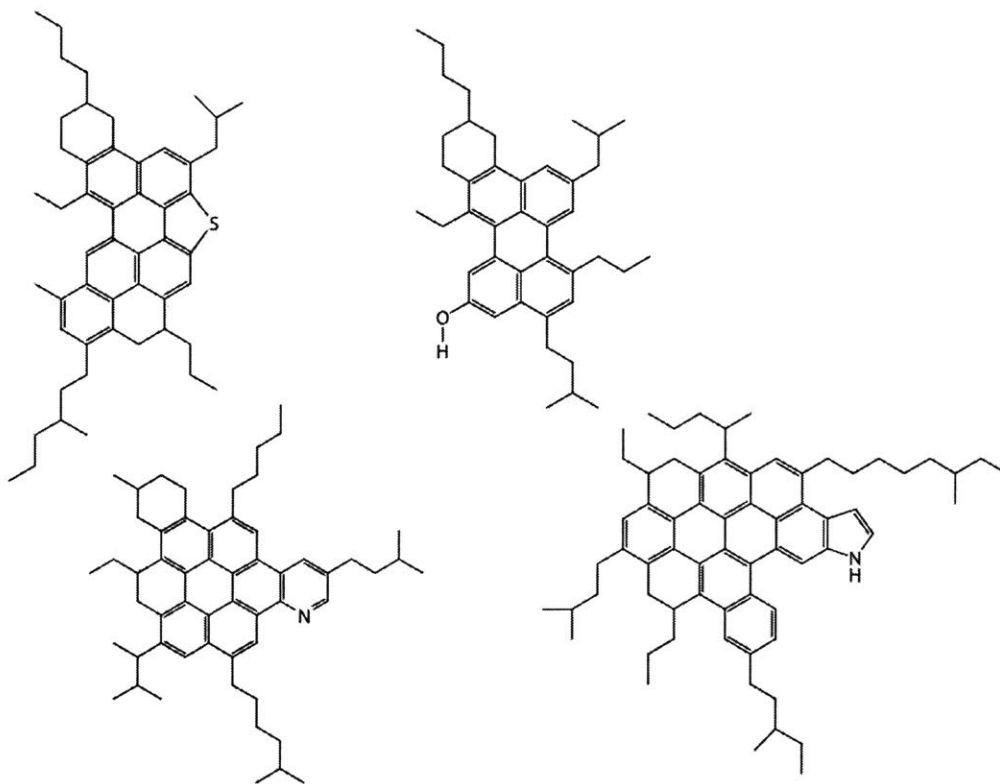
Figure 3-1: Model structures of typical asphaltenes. Asphaltenes have single aromatic cores with some heteroatom content and hydrogen or aliphatic termiations at the edge of the ring systems. Reproduced from [112]

.

aromatics/less hydrogen (9.8 wt% H). As a result, it contains 40% asphaltenes.

While I demonstrated that the electrical properties of coals are of interest for a broad range of applications and may compete favorably with synthetic carbon materials, the use of 10's to 100's of nm diameter suspended particles presents challenges for some device architectures. Figure 3-2 highlights some of the challenges. Following annealing, the large masses of material connected by thin bridges limits the conductivity of the material by forcing the charger carriers to traverse narrow bottlenecks. In a Joule heating device, those bottlenecks may be prone to overheating and thus oxidation or failure. The larger masses of the material increase the optical absorption – undesirable for transparent conductors – and those carriers may be difficult to extract in photovoltaic device due to their distance from a junction. Even in a film which has not been annealed, it is difficult to deposit pinhole free films, and an inherent roughness is present which is extremely detrimental to field effect transistor fabrication. Finally, the particle restricts the thinnest the film can be fabricated to a few times the diameter of the particles.

In contrast, the true solubility of asphaltenes and vacuum residuals in solvents such as toluene enables fabrication of smooth films with thickness determined by the concentration of asphaltenes and spin coating conditions (Figure 3-3). This approach can easily allow the variation of the film thickness to impact such properties as optical transmission (Figure 3-4). The ability to controll the film thickness in this manner is critical to applications ranging from photovoltaic absorbers to transparent conducting thin films.

3.2 Conductivity of Annealed Vacuum Residuals

The optical and electrical properties of annealed vacuum residuals were studied. While the coal materials I discussed previously can be quite conductive following high temperature annealing, they remain too optically opaque for many applications. Similarly, other researchers have tried to manufacture thin films of carbon black to leverage its low cost and high conductivity for applications in displays, light har-
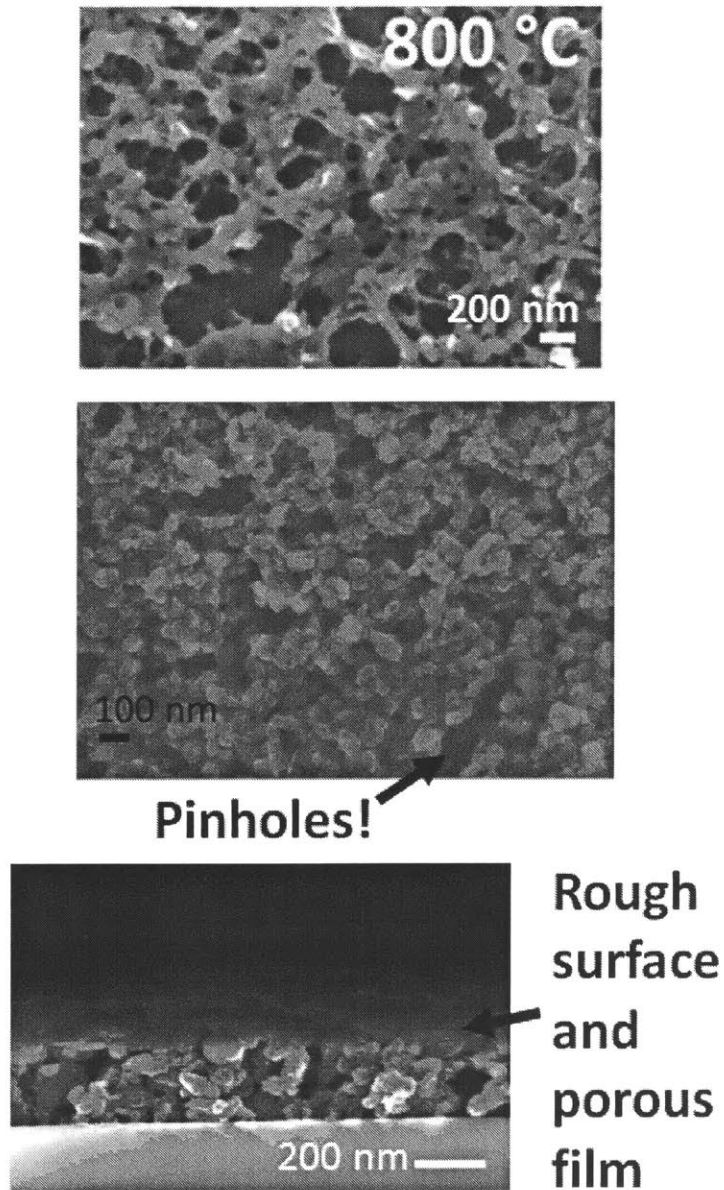
Figure 3-2: Top SEM image shows a hvAb film after annealing at 800 °C showing the formation of a web like structure which is detrimental to optical transmission and electrical conductivity. The center and lower images show the presence of pinholes and film roughness in unannealed hvAb. Such features are detrimental to the fabrication of sophisticated devices such as photovoltaics and field effect transistors.

Figure 3-3: Asphaltene thin film deposited by spin coating onto a silicon wafer with a 300 nm thermal oxide coat.

Figure 3-4: High temperature annealed vacuum residuals deposited on quartz disks. The dark rings are material deposited by contact with the o-ring on the bottom side of the quartz during spin coating.

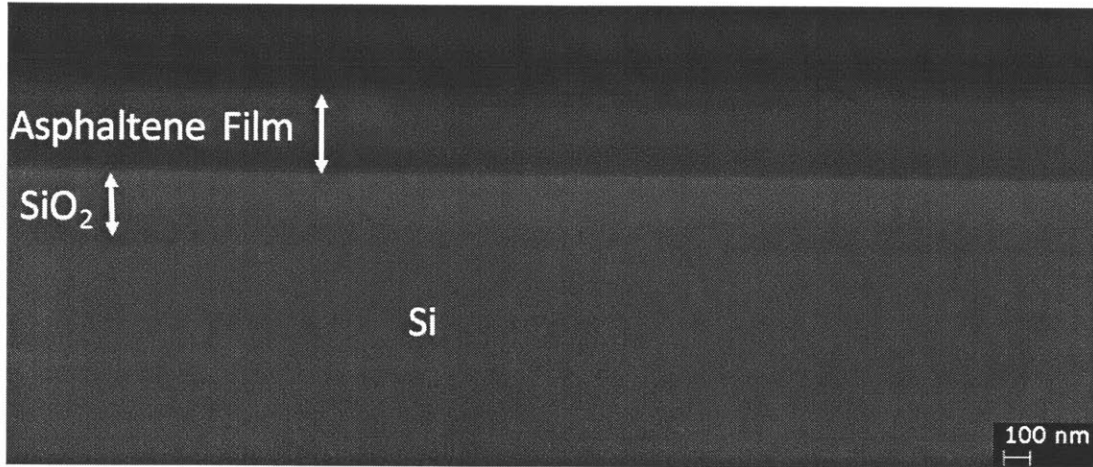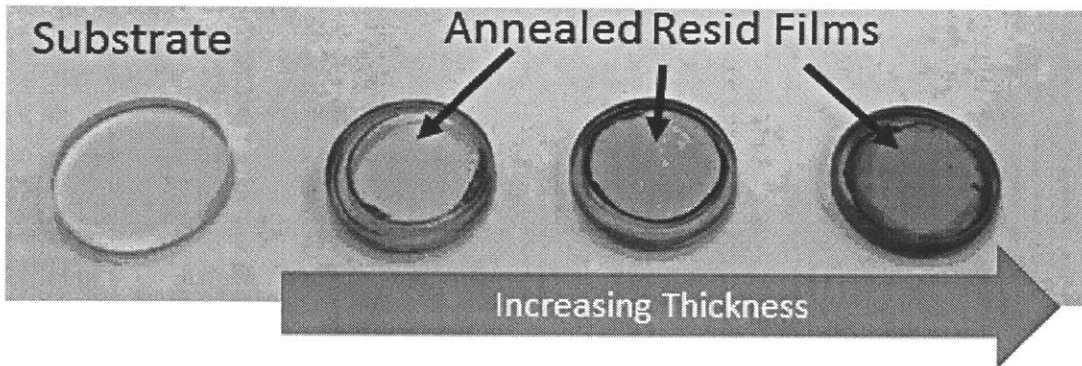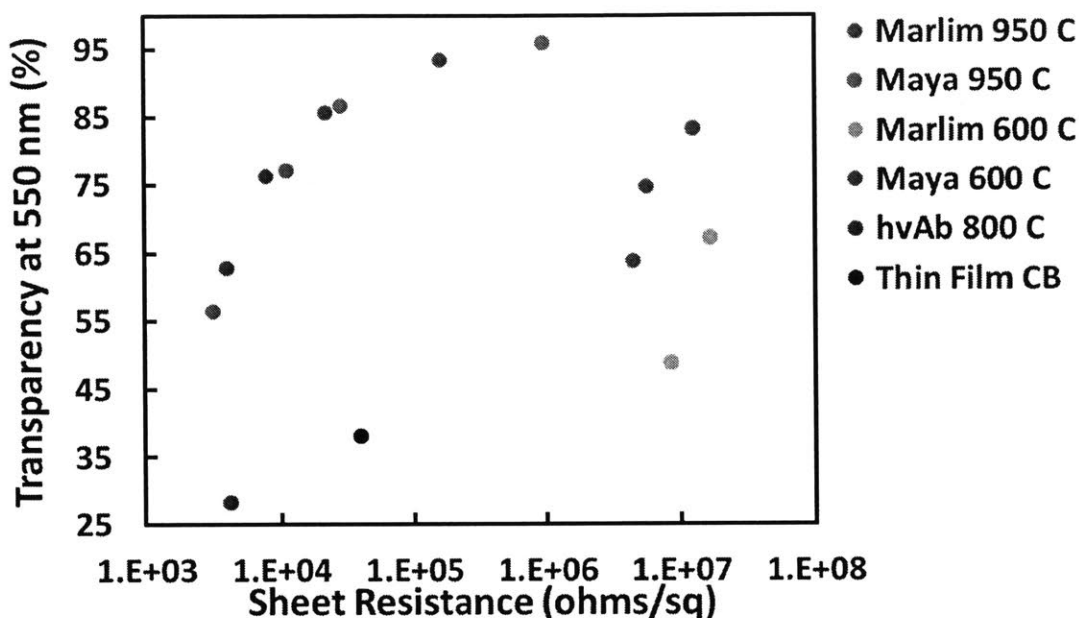Figure 3-5: Transmission of visible light at 550 nm as a function of sheet resistance for vacuum residuals annealed at 950 and 600 °C. For comparison hvAb previously described and layer by layer deposited carbon black [114] are also shown.

vesting, and coatings. However, even using layer-by-layer techniques, thin films with good optical transparency and electrical conductivity have proven difficult to prepare [113, 114]. As shown in figure 3-5 by annealing vacuum residuals under argon after deposition onto quartz substrates, I prepared thin films of low cost carbon with sheet resistances approximately 10^4 ohms per square at 85 % transmission at 550 nm in contrast to carbon black films of similar sheet resistance and less than 40 % transmission. This was also a significant improvement in transparency over the coal films previously discussed.

3.3 Electrical Studies of Asphaltenes

The fabrication of more sophisticated devices such as photovoltaics requires more detailed knowledge of a materials energy levels – in particular their alignment relative to vacuum so that heterojunctions can be designed. Cyclic voltammetry was used to characterize the onsets of oxidation and reduction of asphaltenes prepared from
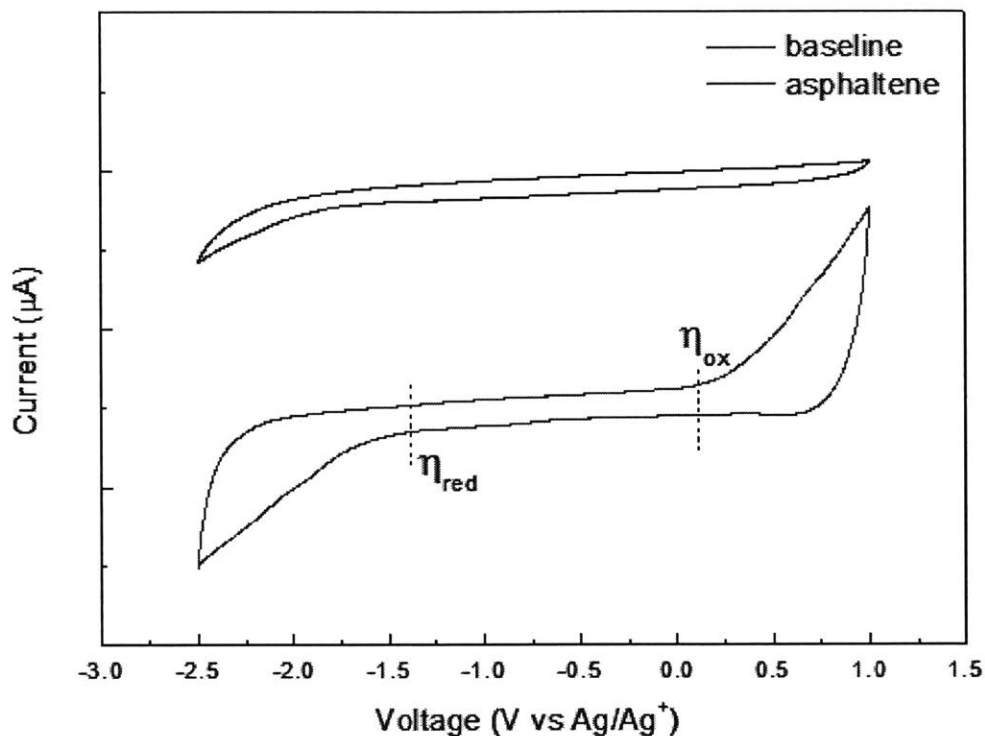
Figure 3-6: Cyclic voltammetry of asphaltenes prepared from Maya vacuum distillation residuals relative to a Ag/Ag+ reference electrode. A scan baseline is included to clarify the onset of oxidation and reduction.

the Maya residual (Figure 3-6). Oxidation onset occurred at -0.11 V relative to a Ag/Ag+ reference electrode and reduction at -1.36 V. Calibration of the Ag/Ag+ electrode to Fc/Fc+ standard gives values of the effective HOMO and LUMO for the asphaltene blend to be 5.30 and 3.83 eV respectively. This electrical gap of 1.47 eV can be validated by comparison to the optical gap of the material (Figure 3-7). Using exceeding $10^4 cm^{-1}$ as the definition of the optical gap, it can be determine to be 1.51 eV in the case asphaltenes prepared from the Maya residual. The asphaltenes from the Marlim residual have a larger optical gap of 2 eV which underscores the range of properties available in the natural carbon space.

53

Figure 3-7: Absorbance of asphaltene films from both Marlim and Maya vacuum residuals.

3.4 Conclusions and Future Work

The solubility of these materials enabled an advance in the optical transparency of thin films of highly conductive carbon enabling applications in displays, transparent heating, thin film photovoltaic contacts, and other transparent electric 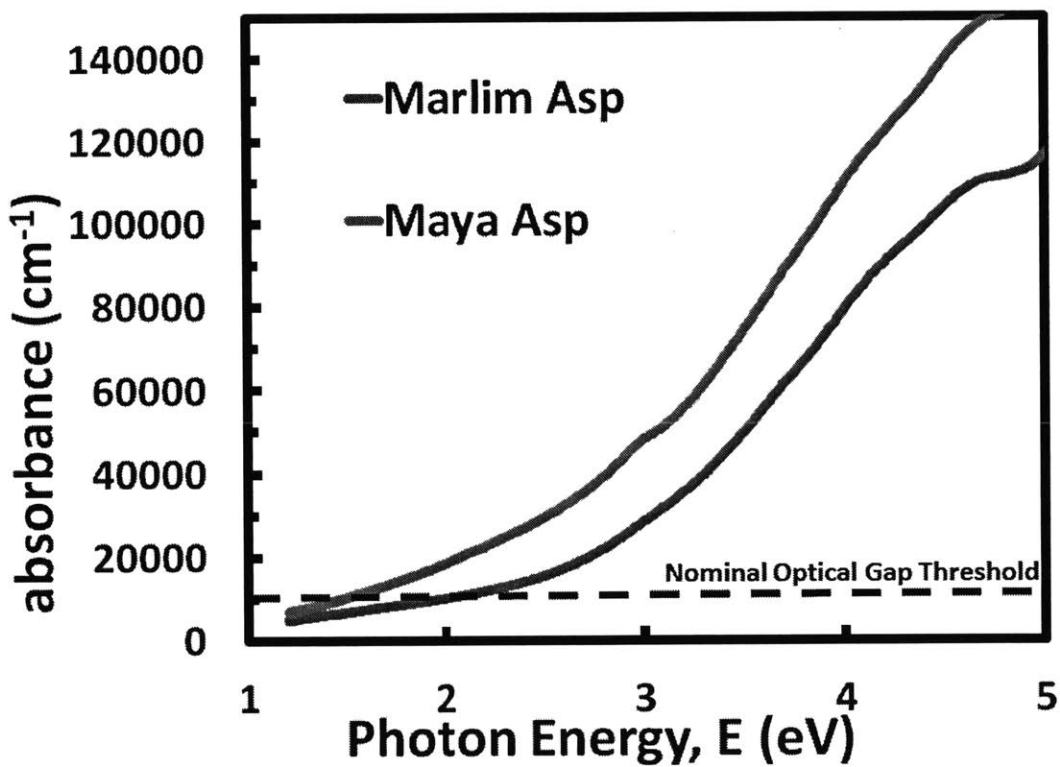devices. Specifically, an improvement from 35% to 85% transparency was achieved compared to thin films of carbon black using high temperature annealed vacuum residuals. In addition the HOMO and LUMO levels of asphaltenes were characterized. This information could be used to develop more sophisticated devices. For example, a band diagram for a possible photovoltaic device is show in figure 3-8 which is based on a hetero junction between Maya asphaltenes and α, ω - Dihexylsexithiophene, a solution processable small molecule absorber to serve as a well understood material for a proof of concept device.

Much work remains before it will be clear if and where natural carbon devices from coal, asphaltenes, or other materials will find applications in electronic devices. Important questions about trap states, carrier mobility, majority carrier type, and exciton lifetime remain. In addition, vast majority of the materials phase space remains unexplored. Direct modification using the tools of synthetic chemistry may enable more intelligent means of connecting sp^2 cores than simple thermal annealing. Hall measurements or field effect transistor devices would provide fundamental insight into the electronic properties of these materials by decoupling the carrier density from the mobility and identifying the majority carrier type. Prolonged lower temperature annealing may allow better connection of sp2 domains without as large of an increase in domain size possibly enabling a wider gap semiconducting natural carbon with good mobility. Finally, the impact of heteroatom content on doping can only be answered by expanding the phase space of coals, asphaltenes, or other natural carbon studied. Utilizing different materials with different heteroatom content may ultimately lead to devices entirely composed of natural carbon – a truly exciting prospect.
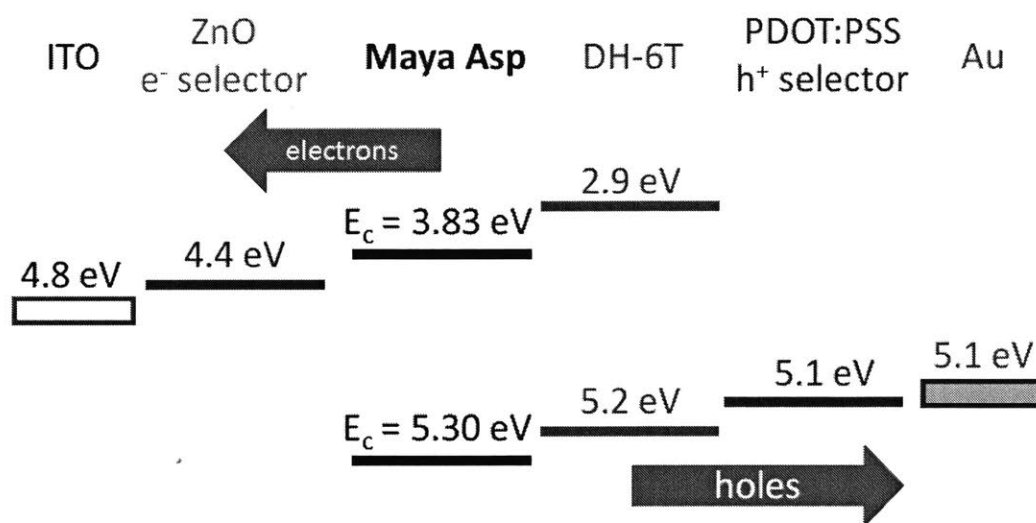
Figure 3-8:   Theoretical band alignment of possible asphaltene containing photo-voltaic device.

Chapter 4

Large Area MoS$_2$ Monolayers

4.1 Introduction

Monolayer and few layer transition metal dichalcogenides (TMDs) including MoS$_2$ have attracted attention as materials for transistors[33], photovoltaics[44, 43], sensors[115, 116], and flexible systems[117], due to their tunable[31, 30] and unique electronic properties[33, 118, 119]. The direct technological application of such films relies on the availability of large area, low defect density materials with precise layer control[120]. To date, a number of methods have been used to synthesize films of MoS$_2$ and other TMDs including chemical vapor deposition (CVD)[120, 47, 121, 122, 123, 124, 125, 126]. However for applications including integrated circuits which require large area, complete and/or conformally grown films, an alternative approach under investigation for the deposition of MoS$_2$ and other TMDs centers around the deposition of a thin film of the transition metal or its oxide and subsequent exposure to a sulfur containing vapor at high temperature[52, 127]. While this approach is limited by the uniformity, thickness, and continuity of the starting oxide or metal, for this very reason it offers a number of potential advantages compared to a CVD method if that oxide can be deposited with exceptional control.[120, 52, 127]. For example, extremely large area, complete films, as well as conformal monolayer coatings and abrupt vertical heterostructures may be comparatively easy to achieve. While ALD has been used to deposit extremely uniform and thin oxide films to generate large area layer

control for WS_2[53], MoS_2 and $WxMo_1 - xS_2$ alloys[54], given how promising this approach is, it is surprising that it has not received much greater attention. This is in part because the oxide deposition must be so well controlled. A detailed understanding of the specific deposition conditions is required to accelerate nucleation such that film coalescence occurs at a thinner film than the amount required for a monolayer of MoS_2. This requirement is challenging even with the highly reactive precursors used for oxide synthesis[55] due to the extreme thinness of monolayer MoS_2. The results from previous work[54] use $Mo(CO)_6$ and oxygen plasma PEALD and sulfurization with H_2S. While this method clearly shows significant promise for large area, well controlled growth, the factors which control the nucleation regime and thus the thinnest possible coalesced oxide film are still not yet completely understood hence limiting the applicability of this method for ultimate commercial fabrication of MoS_2 and other TMDs.

In this work, we focus on the investigation of sulfurization of MoO_3 films deposited from $(tBuN)_2(NMe_2)_2Mo$ and ozone[128] or from $(tBuN)_2(NMe_2)_2Mo$ with oxygen plasma. For both cases a post sulfurization process using elemental sulfur vapor was employed. The novel optimization methods to control nucleation kinetics of MoO_3 were the choices of oxidant, PEALD temperature, an extended Mo precursor exposure, as well as plasma and piranha surface oxidants were studied. The composition of the film was characterized after each step of a multistep sulfurization of the oxides, and the control of oxide nucleation was used to synthesize large area ($> 1cm^2$) monolayer MoS_2 films. Finally, through slower sulfurization temperature ramps, the photoluminescence (PL) intensity and the 2H MoS_2 crystal quality could be further improved independent of the layer control provided by the PEALD nucleation engineering.

4.2 Oxide Deposition Engineering

ALD and PEALD of MoO_3 films were deposited on silicon wafers with both native oxide and thermal oxide (300 nm) surfaces. The ALD process was monitored with

in situ ellipsometry (Figure 4-1a). The deposition is observed to be step wise in a true ALD process with film thickness controlled by cycle count. The growth per cycle (GPC) was observed to be constant after approximately 15 cycles indicating a nucleation inhibited regime in the first 15 cycles. Atomic force microscopy (AFM) of the as deposited oxide (Figure 4-1b-d) shows nucleation islands after the first cycle which can be observed to increase in size and density through the 4th and 7th cycles. Following sulfurization, MoS_2 was transferred onto fresh thermal oxide (300 nm) on silicon wafers using a polymer transfer – MoS_2 films were coated with PMMA, followed by etching of the underlying native oxide or thermal oxide with 10% HF, rinsed with DI water, transferred to the new substrate, and the PMMA was removed with warm acetone. Scanning electron microscopy (SEM) and AFM of the edges of transferred MoS_2 show that the nucleation islands are preserved resulting in an incomplete and rough film (Figure 4-1b-d). While the PMMA transfer is possible with even the very thin native oxide, at high temperature silicon and sulfur react and form volatile products[129, 130] and thus without the protective diffusion barrier, the sulfur vapors were observed to etch pits in silicon wafers with only native oxide at temperatures above 700 °C (Figure 4-2). With the exception of small tears and wrinkles associated with the polymer transfer, the MoS_2 films prepared by this method show excellent uniformity with complete MoS_2 coverage of the wafer fragment sulfurized (Figure 4-1d).

Because the film morphology was preserved during sulfurization (Figure 4-1b-d), to grow complete monolayer MoS_2 over large areas, the coalesced oxide film thickness must be reduced to less than that required to produce a monolayer of MoS_2 from MoO_3 (assuming no losses of Mo due to volatility or diffusion during the sulfurization and based on the bulk densities of MoO_3 and MoS_2, approximately 0.7 nm thick). To reduce the thickness of a film at coalescence, the density of nucleation islands must be increased. This can be accomplished through increasing precursor reactivity and dosing or by reducing surface mobility of adhered species, if they are sufficiently mobile to diffuse to nucleation islands. To increase reactivity, the process was adapted to PEALD. While thermal ALD deposited films were grown at 300 °C to provide the
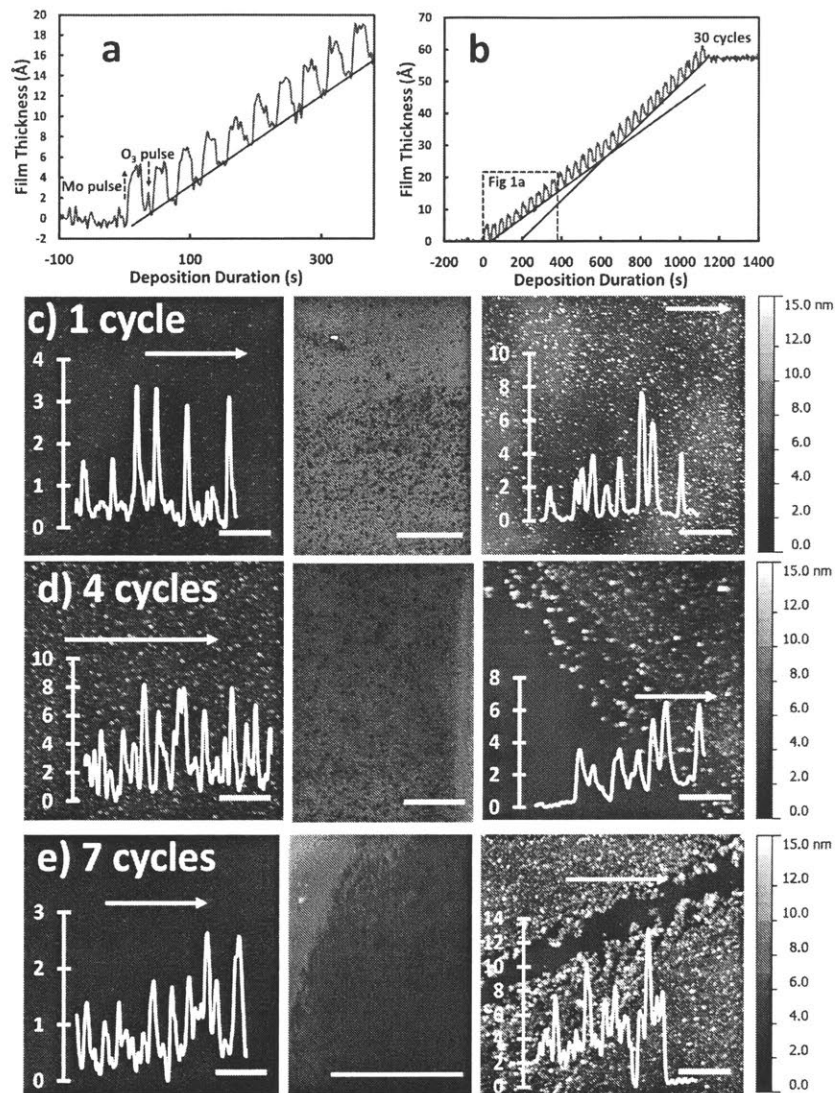
Figure 4-1: Nucleation of MoO_3 films from ALD process on as received silicon wafers. (a) In-situ ellipsometry of ALD growth of MoO_3 from $(NtBu)_2(NMe_2)_2Mo$ and Ozone. The film can be observed to thicken with each $(NtBu)_2(NMe_2)_2Mo$ and thin following oxidation by ozone to MoO_3 with consistent growth per cycle starting after the second cycle in a true ALD process. (b) Ellipsometry of the same film deposition as in a. The initially lower growth per cycle after approximately 15 cycles indicates nucleation inhibition in that regime. The lines in a and b are to guide the eye. (c-e) From left to right, AFM of ALD MoO_3 nucleation islands, SEM and AFM of the edge of a MoS_2 film following sulfurization and transfer to a 300 nm SiO_2 on Si wafer. Initial few nm islands present after 1 cycle are observed to increase in height and density as the cycle count is increased and by 7 counts the film nears coalescence into a few nm MoS_2 film. All scales bars 1 µm. All AFM vertical scales the same.

Figure 4-2: Optical image of damage to an approximately 1 cm by 1 cm silicon wafer piece from high temperature exposure to sulfur vapors without thermal oxide coating.

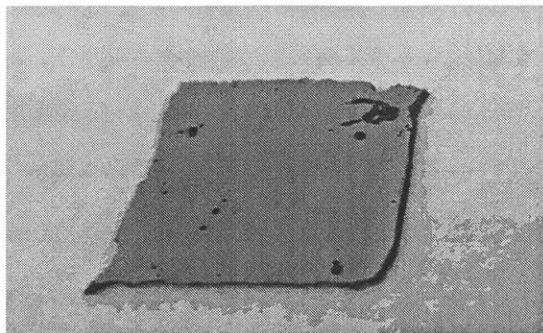highest purity film[128], higher temperatures lead to larger nucleation islands due to increased ad-species diffusivity and/or run-away CVD growth. Because of the increased reactivity of PEALD, the temperature can be reduced without sacrificing film purity (Figure 4-4). Figure 4-3 shows > 10 nm films deposited by PEALD at 150, 200, and 300 $°C$. At 300 $°C$ very large nucleation islands are observed, indicative of precursor decomposition and CVD growth at nucleation sites spaced hundreds of nm apart. The roughness of the films is dramatically reduced at lower temperature indicating a true ALD process and is further improved from 200 to 150 $°C$ with reduced surface mobility of precursor species.

Nucleation islands with one nanometer thickness are still observed for PEALD growth at 150 $°C$ (Figure 4-5a). While significantly improved over the ALD process after a similar number of cycles, the islands are still larger than needed to produce monolayer MoS$_2$ (less than 1 nm) from coalesced films. In an attempt to further increase the nucleation density (and thus reduce coalesced film thickness), the number of molybdenum precursor pulses was increased, but no qualitative improvement in the nucleation regime was observed (Figure 4-5b) indicating that Mo precursor transport and reaction kinetics are not limiting in the nucleation process. Large nucleation features associated with surface contaminants not removed by an oxygen plasma treatment were exacerbated by the extended molybdenum exposure and appear as large bright (tall) spots.
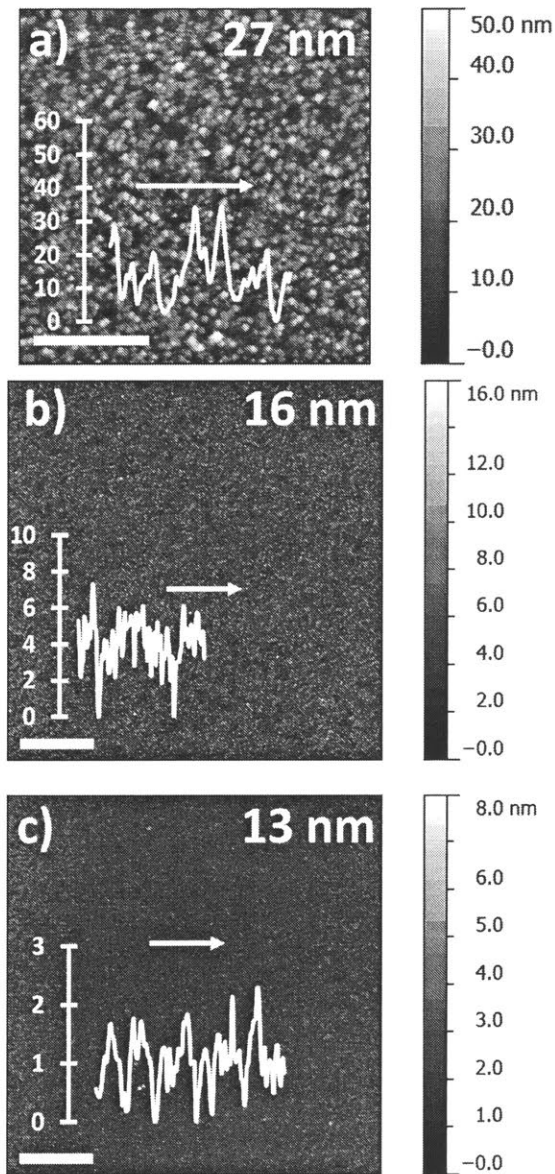
61

Figure 4-3: Impact of temperature on PEALD process. AFM images of thick films showing rough large nucleation features at a) 300 °C and coalesced films at b) 200 and c) 150 °C indicating a transition in growth regime. The 150 °C samples is observed to be smother than the 200 °C samples indicating the reduced mobility of active species at lower temperature. All scale bars 1 μm.
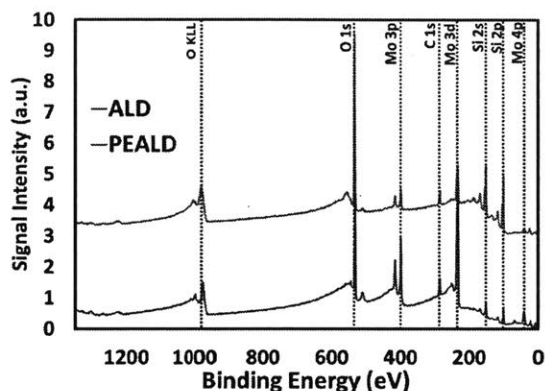
Figure 4-4: Survey XPS spectra of the surface MoO$_3$ films after deposition by ALD and PEALD. Major peaks from all components are labeled.

Finally, a piranha cleaning treatment prior to PEALD growth was found to be exceptionally effective in increasing nucleation density and eliminating nucleation islands larger than one nm after 5 cycles (Figure 4-5c). The piranha treatment increases the hydrophilicity of the surface and a high density of hydrophilic functional groups often improves ALD nucleation. However, piranha followed by oxygen plasma cleaning before PEALD growth did not improve nucleation density highlighting the importance of hydroxyl functionality on the silica surface for reactivity with the molybdenum precursor (Figure 4-5d). Piranha was also effective in reducing the size of the large nucleation islands potentially related to contamination.

4.3 Sulfurization

To sulfurize the oxide films into MoS$_2$, approximately 1 cm^2 wafer cuttings were loaded into a quartz tube furnace under an Ar and H$_2$ atmosphere at low pressure. At the desired temperature, a solid sulfur source immediately upstream of the furnace was heated to produce sulfur vapors. Because MoO$_3$ is a volatile oxide, a multistep sulfurization was adopted, to first partially reduce or sulfurize the film at lower temperature (500 to 800 °C) before final processing at higher temperature[54, 131]. Figure 4-6a shows Mo 3d XPS for several annealing temperatures. The as-deposited oxides show a single doublet at higher binding energy as expected for Mo^{6+}. Peak broad-
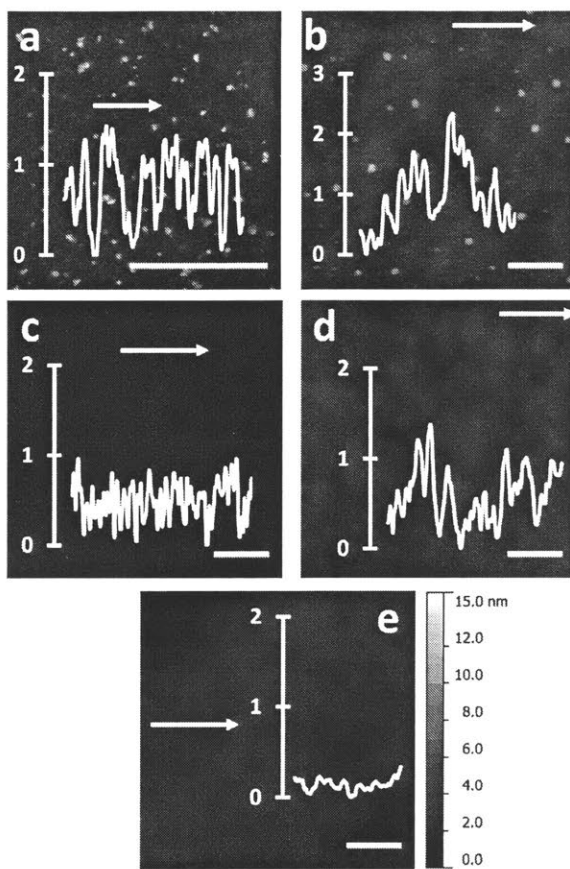
Figure 4-5: Control of MoO_3 nucleation. a) AFM of 5 cycle PEALD deposited MoO_3 following 4 min oxygen plasma clean. Large features are likely sources of nucleation from remaining surface contaminates and small nucleation features can be seen covering remainder of surface. Trace from a clean region (white arrow) shows these smaller nucleation features are 1 nm which result in multilayer MoS_2. b) 5 cycles of PEALD with addition of a 14 s $(NtBu)_2(NMe_2)_2Mo$ extended exposure on a similarly oxygen plasma cleaned wafer. Nucleation islands remain in the 1 nm regime. c) 6 cycle PEALD deposited MoO_3 following piranha clean without plasma clean. Piranha clean removes larger surface contaminants and nucleation islands are observed to be <1 nm in height which is critical to large area monolayer MoS_2 fabrication. d) 5 cycle PEALD deposited MoO_3 following piranha clean but with subsequent oxygen plasma clean. Greater than 1 nm tall nucleation islands which were eliminated with the piranha treatment are observed when the piranha treated sample is exposed to oxygen plasma. e) As received wafer for comparison. All scales bars 1 µm. All AFM vertical scales the same.

ening is indicative of moderate contribution from lower oxidation states. This is in contrast to previous sulfurization work by Song et al.[54] which started from a less oxidized film deposited using a $Mo(CO)_6$ precursor with a single broad Mo 3d complex showing large contributions from Mo^{6+}, Mo^{5+}, and Mo^{4+} which demonstrates the robustness of the subsequent sulfurization with regards to Mo chemistry. After processing at 300 °C, we observe partial reduction with the Mo^{6+}, Mo^{5+}, and Mo^{4+} all present and with 37 atomic percentage (at %) sulfur based on deconvolution of the Mo 3d 5/2 and sulfur 2s complex (Figure 4-6b), but no Raman signal associated with 2H MoS_2 is present (Figure 4-6c) suggesting that the material likely remains amorphous at these temperatures. Increasing the temperature to 600 °C completes the reduction of molybdenum to Mo^{4+} and a weak Raman signal emerges in films, but the film remains depleted in sulfur. Process temperatures up to 700 °C do not result in significant further sulfurization. However, temperature increase to 900 or 1000 °C results in a dramatic increase in the Raman scattering intensity and increase in sulfur content to a nearly stoichiometric 68 at % sulfur. From these results we conclude that while Mo reduction and sulfur incorporation proceeds readily at lower temperatures, high temperatures are required to activate the conversion to the 2H crystal structure.

Figure 4-7a shows post sulfurization thickness as a function of cycle count for several MoS_2 films as well as the oxide thickness for ALD deposited films. The method demonstrates broad tunability in the thickness of large area MoS_2 films, from monolayer through several nm. The positive x-intercept of the guideline shows the combined effects of the remaining nucleation delay and volatile losses during sulfurization. Raman spectra for transferred films show the expected difference in Raman shifts between the A_{1g} and E_{2g} bands (23.6, 22.5, and 19.7 cm^{-1}, respectively) for multi, bi-, and monolayer. In particular, a difference of less than 20 cm^{-1} (figure 5b) was found for the monolayer film which agrees with values reported elsewhere for monolayer MoS_2 on SiO_2 (19 to 20.6 cm^{-1})[54, 14, 39]. AFM characterization shows approximately 1 nm thick film, which is slightly thicker than the bulk layer spacing (0.7 nm) – probably due to layer substrate interactions – in agreement with
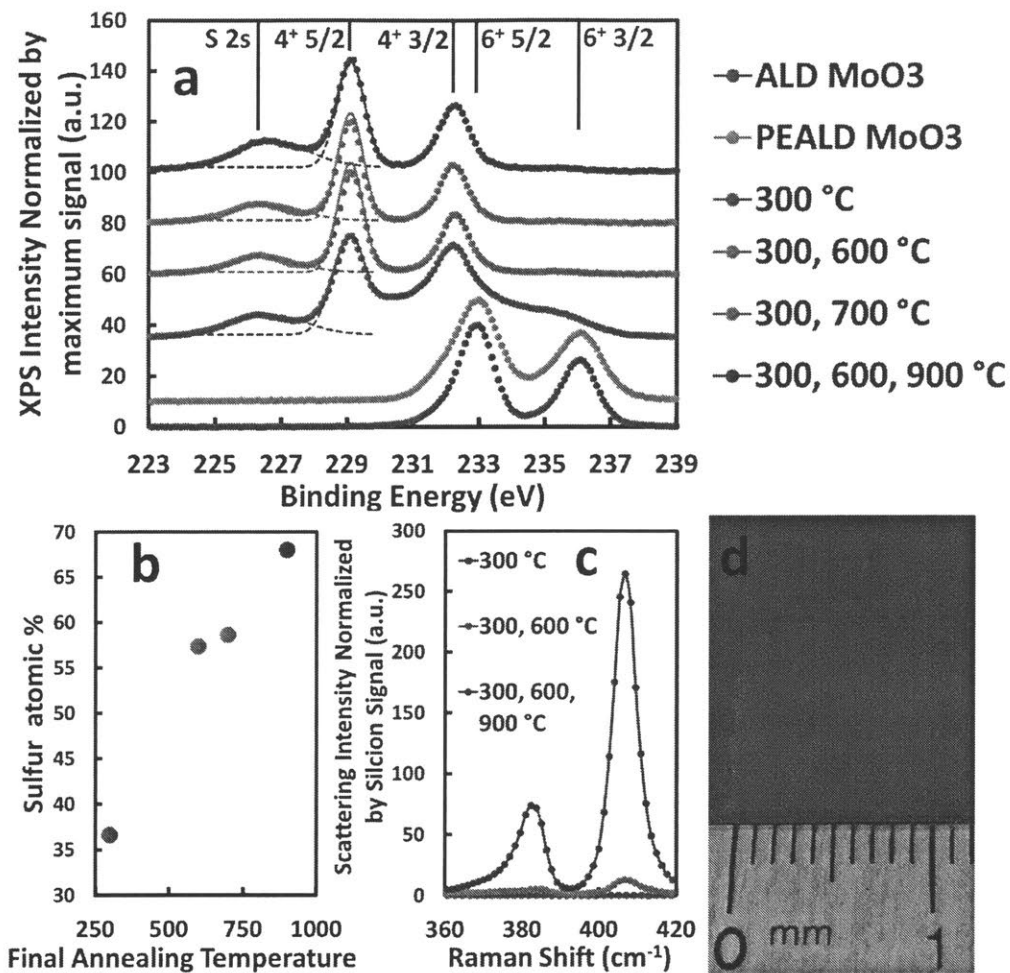
Figure 4-6: Multistep sulfurization of a) Mo 3d XPS normalized by maximum signal for as deposited ALD and PEALD films and following single step processing at 300 $^{\circ}C$, 2 step processing at first 300 and then 600 or 700 $^{\circ}C$, and 3 step processing to 900 $^{\circ}C$. Partial reduction is observed at 300 $^{\circ}C$ (downshift of Mo 3d 3/2 and 5/2 and appearance of S 2s at 226 eV). Films annealed about 600 $^{\circ}C$ show complete reduction of molybdenum. For the annealed samples, the S 2s and Mo^{4+} 3d 5/2 signals were deconvoluted to determine the sulfur content. Dashed lines represent fitted contributions of S 2s and Mo4+ 3d 5/2 and the solid line represents total contribution. b) Atomic percentage of sulfur based on the Mo 3d and S 2s peaks showing partial incorporation of sulfur during 300 $^{\circ}C$ single step anneal and final stoichiometric incorporation via three step anneal. As the sulfur content increases, Raman spectra (c) shows the emergence in the A1g and E2g peaks characteristic of the 2H structure of multilayer MoS$_2$. Processing up to 900 $^{\circ}C$ shows a dramatic increase in the intensity of these peaks. d) optical image of 4.5 nm thick MoS$_2$ following transfer to a larger 300 nm SiO$_2$ on Si substrate showing centimeter scale uniformity achieved with ALD and post sulfurization process.

66

monolayer MoS_2 reported elsewhere[54, 132]. Finally to demonstrate the uniformity of an ALD based approach to MoS_2 growth, Raman spectra were sampled across a 500 μm by 1 cm region with 100 μm distances between points (figure 5d) for a monolayer MoS_2 sample prepared with a 1000 °C final annealing step. The hundreds of spectra collected form a single distribution in A_{1g} and E_{2g} difference centered at 19.7 cm^{-1} and width limited by of the frequency resolution of the detector (0.5 cm^{-1}). This indicates unifrom monolayer coverage accross the sampled area.

PL (Figure 4-7) at the direct band gap energy (1.8 to 1.9 eV)[31, 30] indicates high crystal quality[133, 134] monolayer MoS_2. PL spectra were collected for MoS_2 monolayer films following sulfurization. While the ALD process sets the number of layers of MoS_2 as shown above, the crystal quality is determined by the kinetics of the nucleation of the 2H crystal structure. The decoupling of layer control from crystal quality – frequently impossible in CVD – is an advantage which can allow for independent progress on both challenges. To explore the effect of sulfurization temperature ramp rate on this 2H nucleation and growth process and to improve the crystal quality of the material, samples with an accelerated multistep sulfurization (30 °C/min and holds for 10 min at 600 and 1000 °C) and with slow but linear temperature profiles (4.7 and 6.4 °C/min up to 1000 °C) were prepared. All samples were first partially reduced and sulfurized at 300 °C for 30 min. The slower ramp rate samples show much stronger PL emission which indicates larger and/or more defect free 2H crystal domains. Crystal domain size is determined by the competition of crystal growth from the amorphous MoS_x matrix and nucleation of new crystal domains in that matrix. If a nucleation event requires greater thermal activation than growth of an already nucleated domain, then by heating more gradually, the nucleation rate is comparatively suppressed and 2H MoS_2 domains grow much larger before encountering other domains.

The actual crystal domain size may be indicated by the size of the fragments of MoS_2 at the edge of the film in figures 4-1c and 4-7b. These islands are typically 100 to 200 nm across indicating such as the domain size of crystals in the material as synthesized. Further improvements in crystal domain size are necessary to unlock
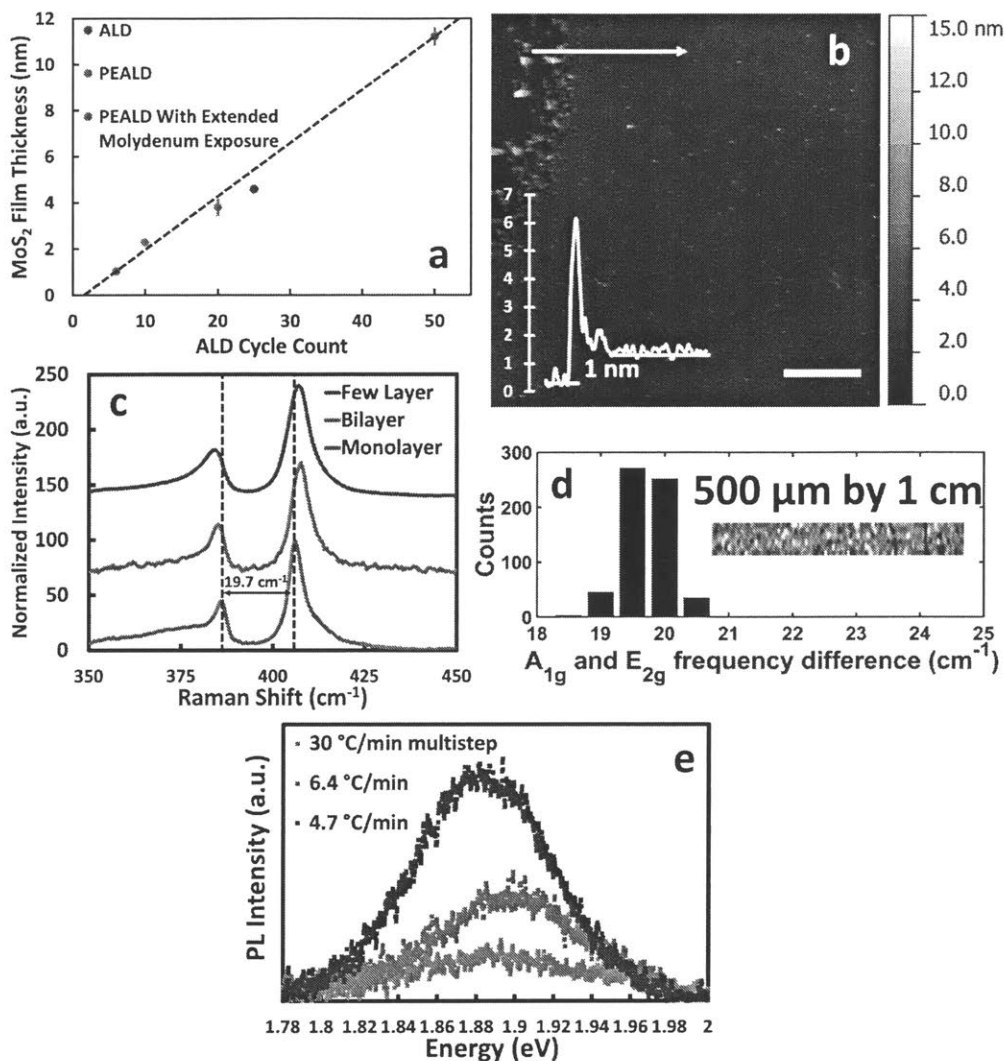
Figure 4-7: MoS$_2$ layer control. a) Resulting MoS$_2$ film thickness as a function of ALD or PEALD cycle count down to the monolayer regime. Line is only to guide the eye. b) AFM of Monolayer MoS$_2$ with trace showing 1 nm film thickness. Scale bar 1 μm. c) Raman spectroscopy of monolayer, bilayer, and few layer MoS$_2$ samples based on E2g and A1g peak separation. d) Large area Raman mapping of monolayer MoS$_2$ showing film uniformity on the cm scale. Histogram shows single distribution of peak spacing centered between 19.5 and 20 cm^{-1} and with width of approximately the detector resolution of 0.5 cm^{-1}. Inset shows spatial map indicating variation is random across sample indicating uniformity in thickness as opposed to regions of difference in Raman peak difference. e) Effect of heating rate on PL signal intensity for monolayer MoS$_2$ samples suflurized with 30 min at 300 °C hold then a 30 °C/min ramp with additional holds for 10 min at 600 and 1000 °C (multistep) as well as two samples with linear temperature profiles (no holds) from 300 °C to 1000 °C.

68

many electronic applications, but doing so after identification of a method which offers independent layer control has clear advantages. Consider the development of large area single crystal graphene growth. Methods were developed from CVD growth on nickel substrates which offered large area, polycrystalline, multilayer materials [68]. A switch to surface limited reactions of copper foils enabled large area, highly polycrystalline monolayers, but provided a platform in which that problem could be tackled independent of the number of layers [12]. More recently, excellent nucleation control has enabled cm scale graphene single crystals [135] grown on copper and even epitaxial wafer scale monolayers grown on germanium by leveraging a similar surface limited reaction [136].

4.4 Summary

In conclusion, a detailed study of the synthesis conditions of the metal oxide film, let to the successful growth of large scale, thickness controlled MoS_2 films via sulfurization of ALD and PEALD Mo-oxide films, which can be transferred onto arbitrary substrates. The effect of temperature, a 14 s extended precursor exposure, plasma and piranha surface treatment on MoO_3 PEALD deposition were studied. Plasma processing at 150 °C was found to be beneficial to nucleation, and a piranha treated surface immediately preceding the first ALD pulse was critical to monolayer MoS_2 fabrication. The molybdenum chemistry and sulfur incorporation were also studied at each stage of the subsequent multistep sulfurization. Although molybdenum reduction and sulfur incorporation into the films occurred at temperatures below 700 °C, elevation to 900 °C was required to activate the conversion to crystallize the 2H structure. Through the control of the nucleation process, centimeter scale monolayers with uniformity across the substrate were synthesized as demonstrated by AFM and Raman spectroscopies.

Ultimately, any growth method for MoS_2 or other TMDs for applications such as digital logic, must offer three features: layer uniformity, complete or controlled coverage, and large domain size or preferably single crystallinity. One of the key

advantages of the method presented is the decoupling of the MoS_2 crystallinity from layer control and coverage by separating this into two distinct nucleation processes. Specifically, we have shown that through control of the ALD process, the nucleation density of the oxide can be controlled on the wafer scale to provide two of the three key features, layer control and uniformity. The subsequent nucleation of the 2H crystal structure at high temperature after sulfur incorporation independently controls the final property, crystallinity. While this will be the subject of future work, crystal quality can be approached through a number of methods including heating rate as shown here. However the ability to tackle this last property independent of the layer count and uniformity of the film – because it is already set by the nucleation engineering of the ALD oxide – is a significant step towards wafer scale, high quality, MoS_2 .

Chapter 5

Mechanically Exfoliated Transition Metal Dichalcogenide Materials

5.1 Solution Exfoliated Transition Metal Dichalcogenides

While deposition methods such as ALD and CVD have to potential to offer excellent materials quality and layer control over larger areas, for applications where very large volumes are needed at low cost such as catalysis, filtration, electrochemical storage, sensing, and even photovoltaics, solution fabrication of monolayers may provide a competitive alternative [117]. For such a process, one of two approaches are typically taken – either the material is chemical modified to force it into solution and then restored such as in the case of Li intercalation in Mos_2 [137], or in the fabrication of rGO. Alternatively, sonication in an aqueous surfactant can be used exfoliate material and stabilize it in water. The later approach has been performed for both graphene [138, 139, 140] and TMDs [141, 142, 117] using cholate to stabilize the flakes. Such a low cost deposition from solution of exfoliated MoS_2 and WS_2 was explored in my work. Solutions prepared by bead milling TMD powder in an aqueous sodium cholate solution followed by centrifugation were provided by PLACEHOLDER. Material from these solutions was deposited on 300 nm thermal oxide on silicon substrates by spin

Figure 5-1: Optical microscope images of a WS$_2$ film transferred onto a 300nm SiO_2 on Si substrate by filtration and floatation on water.

coating, drop casting, and freeze drying. However, the most uniform and continuous depositions onto as received wafers were produced by filtering the solutions through a 25 nm pore nitrocelluose filter and then gently submerging the filter in water to lift off the film from the filter's surface. Placing a substrate on the surface of the water or using it to scoop the resulting film from the water were both successful in transferring the material. Figure 5-1 shows and optical microscope image of a film transferred by this method. SEM of these films (Figure 5-2) reveals material which appears continuous enough for electrical devices although more TMD material can be layered on top of the film by repeating the transfer process.

XPS revealed a high (30%) carbon content in the films due to residual cholate. To address this, solvent, acid, and thiol washes were tested to remove or reduce the carbon content in the films. Specifically, acetone, ethane dithiol, toluene, borane, hydrazine, acetic acid, and solutions of hydrocholic acid , sodium hydroxide, and hydrogen peroxide were tested. While most treatments were not successful, glacial acetic acid exposure did reduce the cholate content and improve uniformity of the carbon content across different regions of the film (Figure 5-3). We also performed annealing
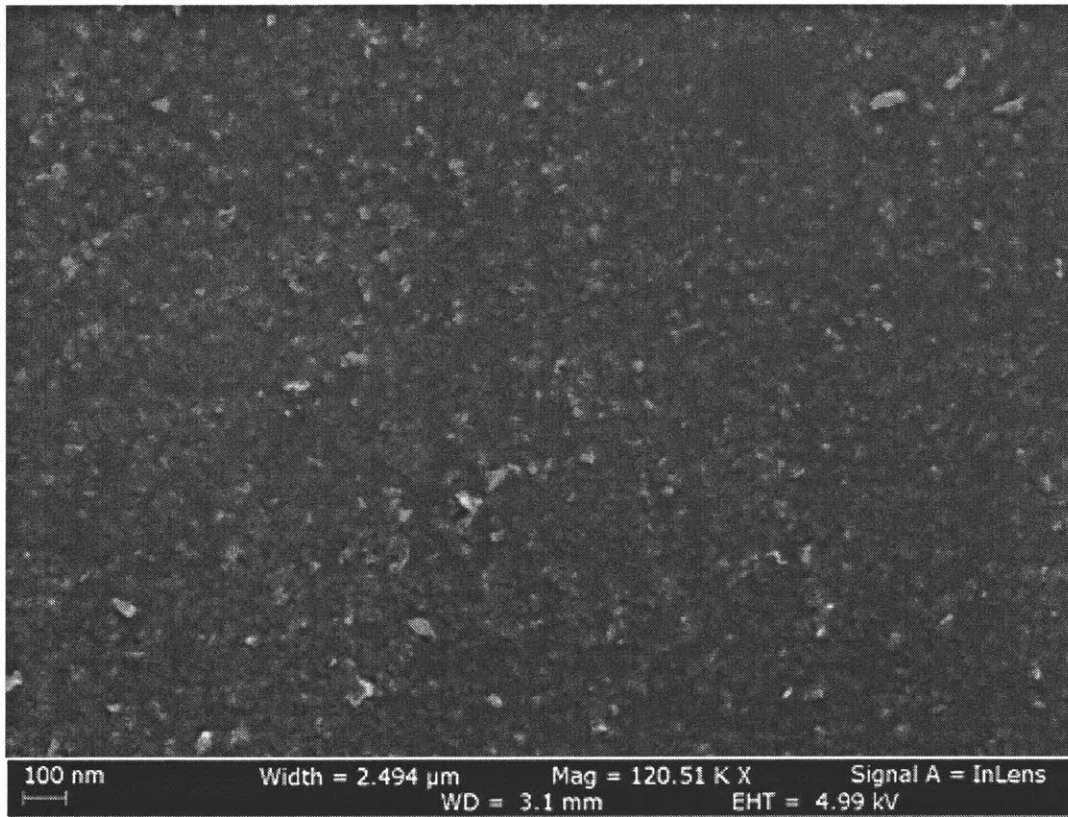
Figure 5-2: SEM micrograph of a WS$_2$ film transferred onto a 300nm SiO_2 on Si substrate by filtration and floatation on water.
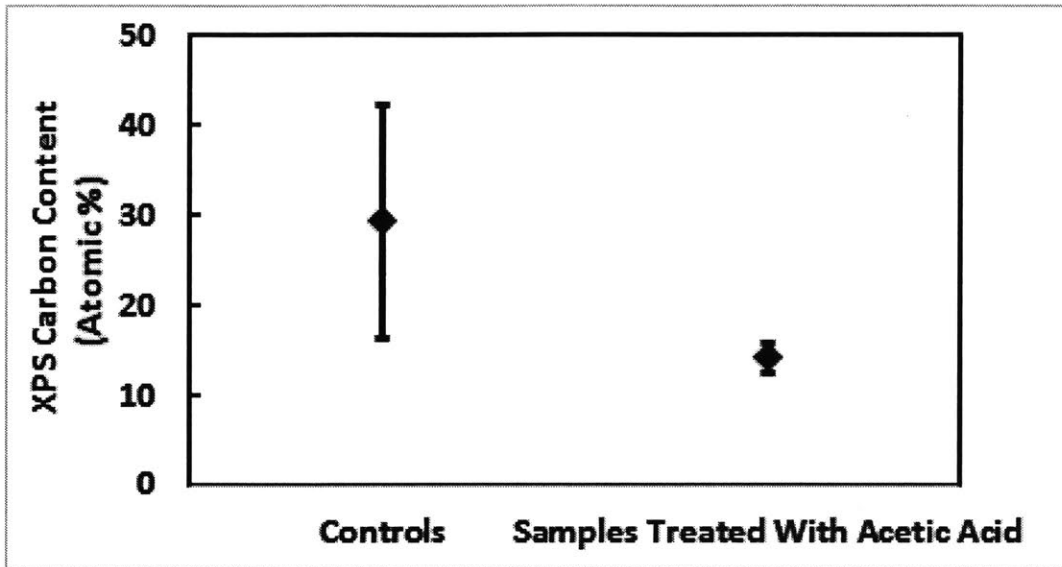
Figure 5-3: Carbon content in WS$_2$ films prepared by bead milling, filtration, delamination, and transfer as described in earlier updates. Treatments with acetic acid is effective at removing a large amount of cholate and improving the homogeneity of the films. Error bars represent standard deviations across at least 10 measurements across multiple samples.

overnight of as deposited films in argon/hydrogen mixtures at 250°C, 350°C, 450°C, 500°C, 550°C, 750°C, and 1000°C, low pressure O_2 plasma etching, and UV ozone. At 500°C, effective removal of surface C is observed, however, loss of S content complicates this approach for cleaning the films (Figure 5-4). Without knowledge of a detail chemcial mechanism, it is possible that a reduced duration and/or intermediate temperature could allow for selective removal of carbon over sulfur. In addition, annealing in a sulfur rich atmosphere may prevent or heal sulfur loss.

For many solution processed or low cost applications requiring large amounts of material, solution processed films could provide a significant advantage over more expensive but better layer controlled deposition methods. In such processes, ligands are used to improve yield, solution stability, paritcle size, and coating morphology. Removing the ligands post deposition is critical to improving electrical contact between flakes. Based on this work, glacial acedic treatments can prove effective in remoing much of the surplus cholate following deposition. Thermal based methods cause damage to the MoS$_2$ flakes, but it is likely that such sulfur loss may be preventable or
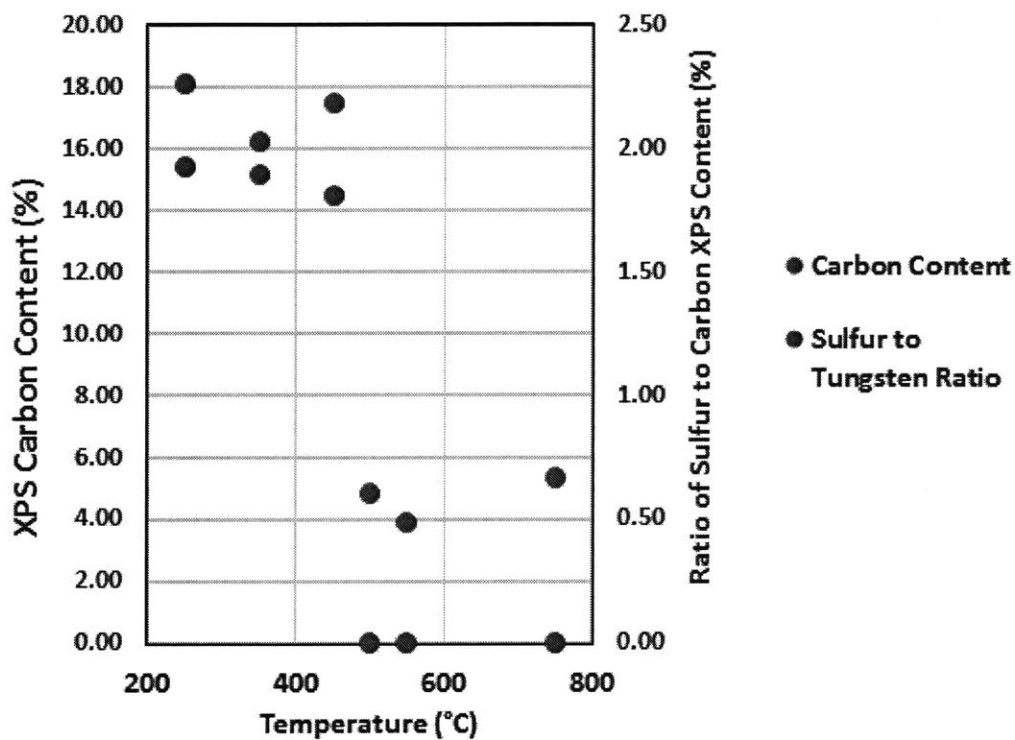
Figure 5-4: Average compositions of WS_2 films after annealing overnight at several temperatures. Loss of both carbon and sulfur occurs between 450 and 500°C indicating cholate decomposition at either the same temperature or via a mechanism which results in the desulfurization of the WS_2.

reversible with further study.

5.2 Tape Exfoliated Graphene MoS$_2$ Heterojunction

Beyond the ability to synthesize or deposit monolayer TMD materials, we must also consider their use in complex devices. In this part of my thesis, I describe preparation and characterization of a junction between a monolayer of MoS2 and a sheet of graphene. Of particular interest is the heterojunction between MoS$_2$ and graphene which has been predicted by Bernardi et al. [43] to from a Schottkey barrier for holes that could be used as a photovoltaic (Figure 5-5). Using Adhesive tape exfoliation of MoS$_2$, monolayer and few layer samples of MoS$_2$ can be prepared (Figure 5-6). The number of layers of such samples can be validated using Raman spectroscopy [14] (Figure 5-7). A monolayer of MoS$_2$ prepared in this manner was used to fabricate a graphene MoS$_2$ heterojunction (Figure 5-8). Charge transfer of photogenerated carriers from MoS$_2$ to graphene through quenching of the photoluminescence (PL) signal was observed. The PL spectra were normalized by the A_{1g} Raman signal intensity [31] to control for variables such as the focus of the microscope. Electrons, holes, or complete excitons are injected from the MoS$_2$ sheet into the graphene sheet followed by non-radiative recombination which results in the quenching of the PL signal following the transfer of the graphene sheet. Based on the previous computational results [43], we hypothesize that electron injection from MoS$_2$ into the graphene sheet is the primary charge separation mechanism. Validation of charge transfer from MoS$_2$ to graphene both demonstrates a potential first step in a photovoltaic process. It also shows that this transfer method can be used to produce sufficiently clean and well contacted junctions for electronic and optical devices.

A previous report[143] of these junctions showed much less effective PL quenching, but the devices in that report had significant issues with volatile contaminants that could be removed by vacuum annealing. We have also performed temperature depen-
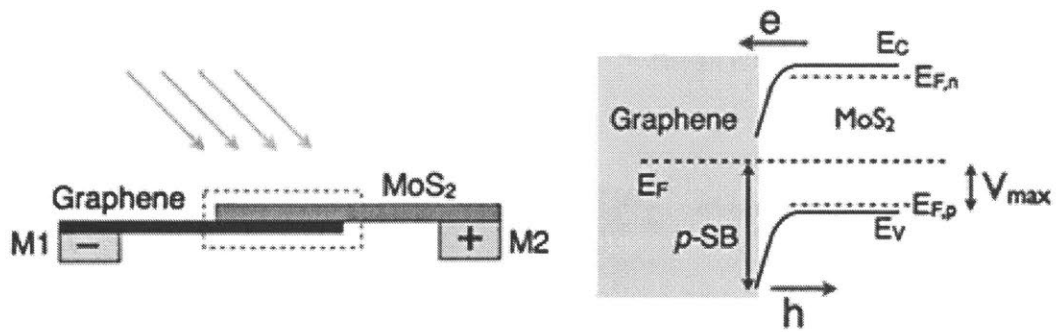
Figure 5-5:   Schematic and energy level diagrams of computed graphene MoS_2 heterostructure. Reproduced from [43]
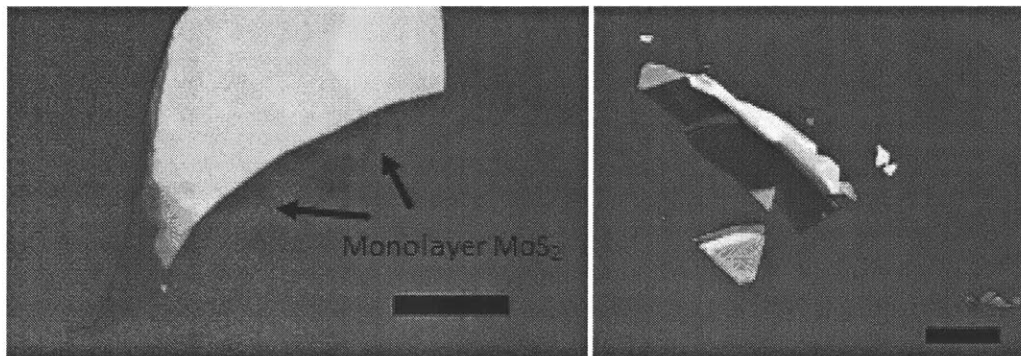
Figure 5-6:   Example of mono and few layer MoS_2 flake produced by automated mechanical exfoliation. Scale bar 10 μm.
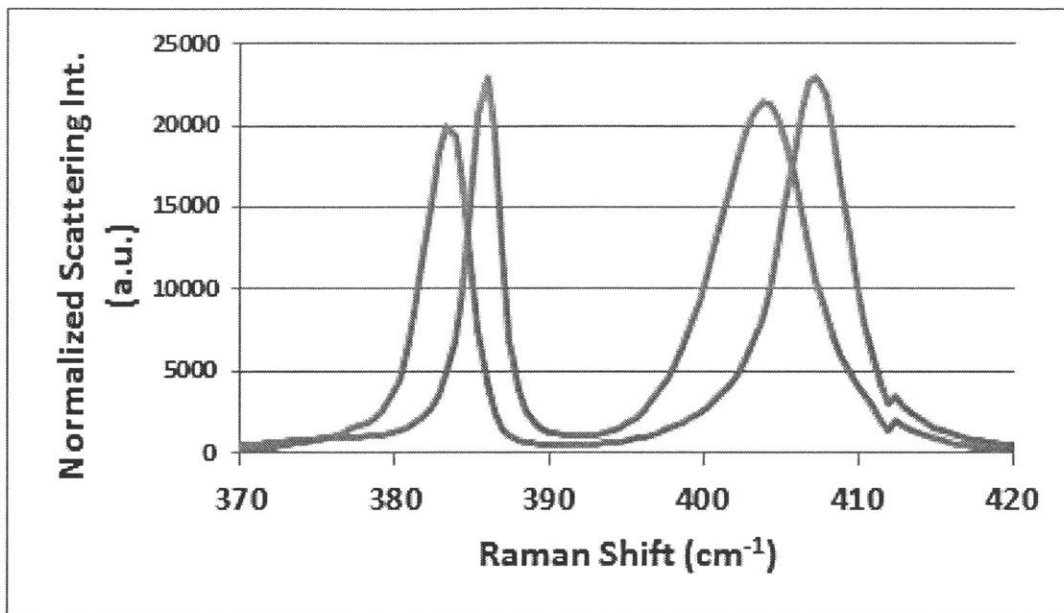
Figure 5-7: Normalized Raman spectra of a monolayer region produced by mechanical exfoliation (green) and a many layered flake (blue) for comparison. The separation between the A_{1g} and E_{2g} agrees well with literature.
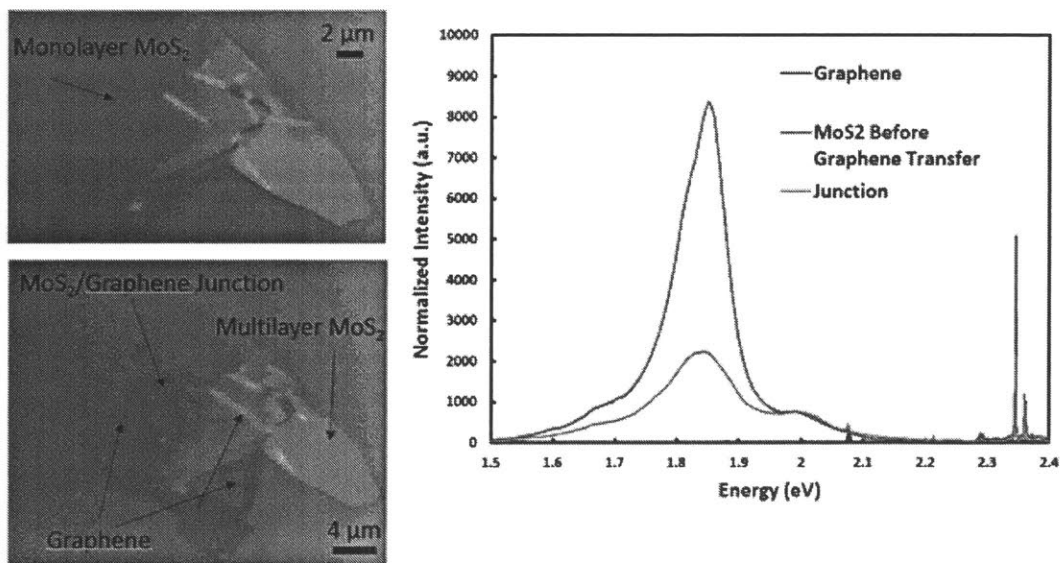
Figure 5-8: Optical microscope image of Monolayer MoS_2 and adjacent multilayer flake before graphene transfer and after graphene transfer. PL spectra collected from monolayer region before and after graphene transfer normalized by the intensity of the A1g Raman signal. Signal from a graphene region without MoS_2 normalized by G peak intensity.

dence studies of the PL signal of a MoS_2/graphene in a nitrogen atmosphere (Figure 5-9). The expected decreased PL with increasing temperature is both expected[144] as non-radiative recombination lifetimes are strongly temperature dependent and reversible which supports the hypothesis that volatile contaminants such as water or acetone are not impacting our PL signal. However, AFM characterization (Figure 5-10) shows significant PMMA contamination from the graphene transfer on top of the junction. Some PMMA contamination is typical and results in p-type doping of the graphene. This effect would be expected to reduce the built in potential of a graphene MoS_2 heterojunction (Figure 5-5) and thus it is expected that it would lessen the degree of photoluminescence quenching. It also points to the importance of future experiments to explore the impact of the transfer processes on TMD and other 2D materials junctions.
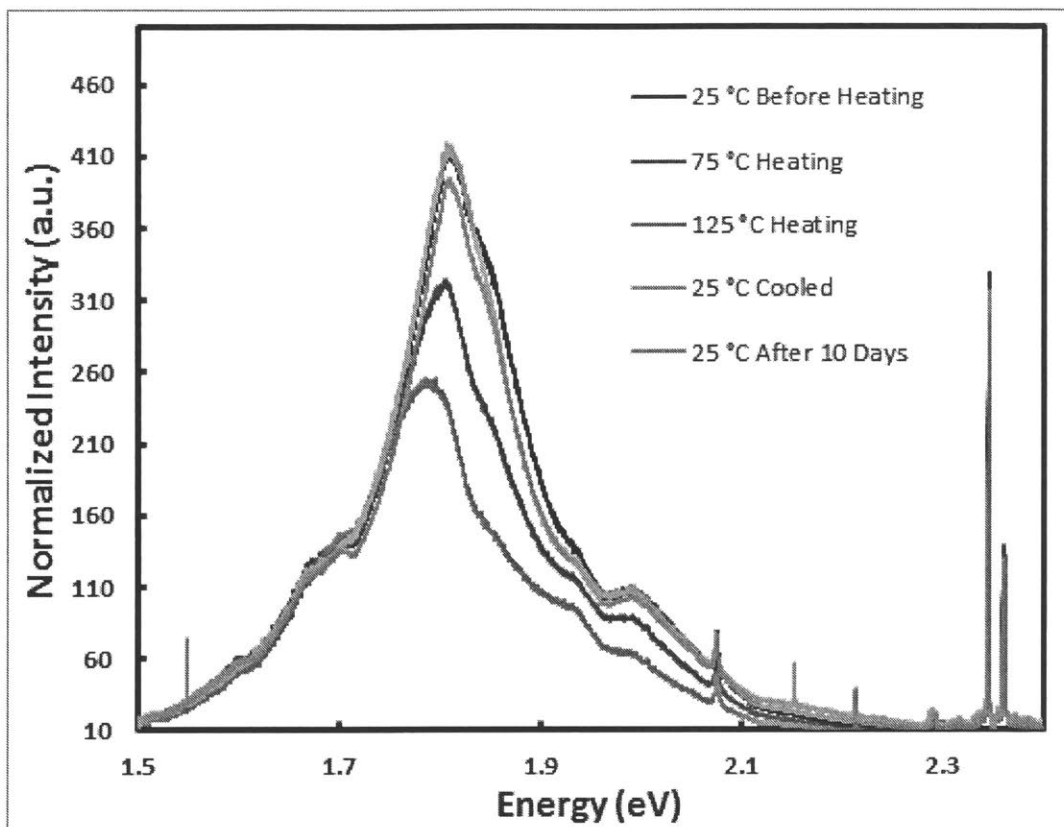
Figure 5-9: Raman normalized PL spectra of graphene/MoS$_2$ junction before, during, and after heating in a N_2 atmosphere. Restoration of original signal after heating supports that quenching is not caused by volatile water contamination.
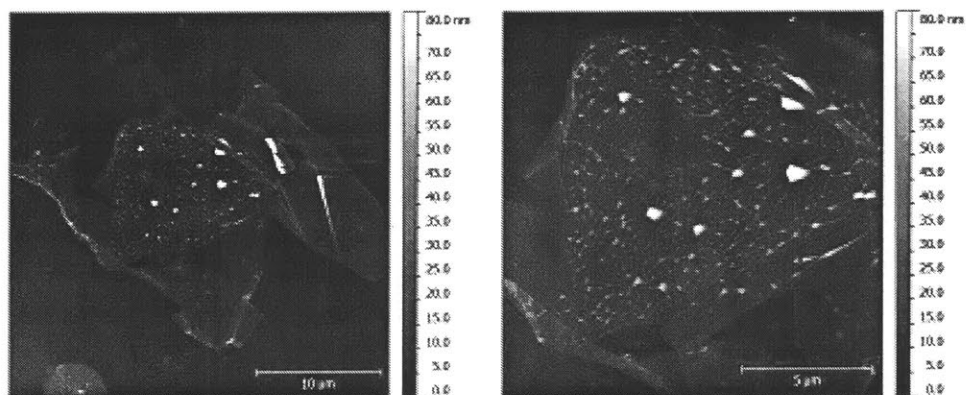
Figure 5-10: AFM images of graphene MoS$_2$ junction showing probable PMMA contamination.

Chapter 6

Materials and Methods

6.1 Coal Film Preparation and Annealing

Department of Energy Coal Standard (DECS) coals (20 mL) were loaded as received with 2 mm stainless steel balls (10 mL) into a stainless steel ball milling chamber (50 mL), and the remaining free volume was filled with IPA. Milling was performed at 450 rpm in Retsch PM 100 ball mill for 100 hours unless otherwise stated. The resulting paste was transferred from the chamber, and the coal was washed off the balls with IPA (75-200 mL). Centrifugation was performed between 2500 and 3500 rpm. Samples were spin coated at 2500 rpm onto either silicon wafers with 300 nm of thermal oxide or quartz substrates in the case of optical absorption measurements. Annealing was performed under argon atmosphere (270 millitorr) for 30 minutes following a 20-minute ramp to the set point temperature. Contacts on samples for electrical measurement were deposited by thermal evaporation of gold and use of a shadow mask.

6.2 ALD and PEALD Oxide Deposition

The MoO_3 films were deposited using both thermal ALD and PEALD techniques. The thermal ALD process was conducted in a cross flow, hot wall Ultratech-Cambridge Nanotech Savannah system at $300°C$. The $(NtBu)_2(NMe_2)_2Mo$ precursor was de-

livered to the chamber using a boosted N_2 precursor delivery. The ozone coreactant was delivered to the chamber with an O_2 /O_3 flow rate of 330 sccm and a concentration of 120 mg/l. The deposition was performed as described by Bertuch et al [?]. The PEALD depositions were performed at $150°C$ in a top flow reactor (Ultratech-CNT Fiji system) using a remote Inductively Couple Plasma (ICP) unit. The argon gas flow for the process was 20 sccm of Ar carrier gas with 200 sccm of plasma Ar continuously flowing through the chamber. The Mo precursor and delivery technique was unchanged and utilized the boosted precursor delivery technique using Ar instead of N_2 gas. The co-reactant was O_2 plasma generated at 300 Watts in a flowing gas of 20 sccm O_2 and 80 sccm Ar. Plasma exposure times were 20 sec with a purge time of 5 sec. For extended Mo precursor exposure, the downstream vacuum valve was closed for 14 sec during the precursor pulse step, then opened for the precursor purge and plasma steps. The piranha treatment was performed using 3 parts 98% H_2 SO4 and 1 part 30% H_2 O_2 within 4 hours of the subsequent MoO_3 film deposition.

6.3 Sulfurization

Sulfurizations were performed at 240 millitorr with 45 sccm of Argon and 4 sccm of H_2 gas flowing. Solid sulfur (500 mg) was supplied at either 125 or 135 $°C$ immediately upstream of the heater. No effect on the sulfurization was observed for the variation in sulfur source temperature. Temperature ramp times between stages were 10 min and the temperature was held at each step for 30 min unless otherwise mentioned.

6.4 2D Materials Transfer

Figure 6-1 shows a schematic of a 2D materials transfer method for graphene grown on copper although it can easily be adapted for transfers of other 2D materials such as MoS_2 grown on silicon oxide. PMMA (Microchem A5 950k ebeam resist) was spun coat at 5000 rpm onto the wafer used as a synthesis substrate. Using forceps or a razor blade, an outline was scratched into the PMMA film to aid release during etching.
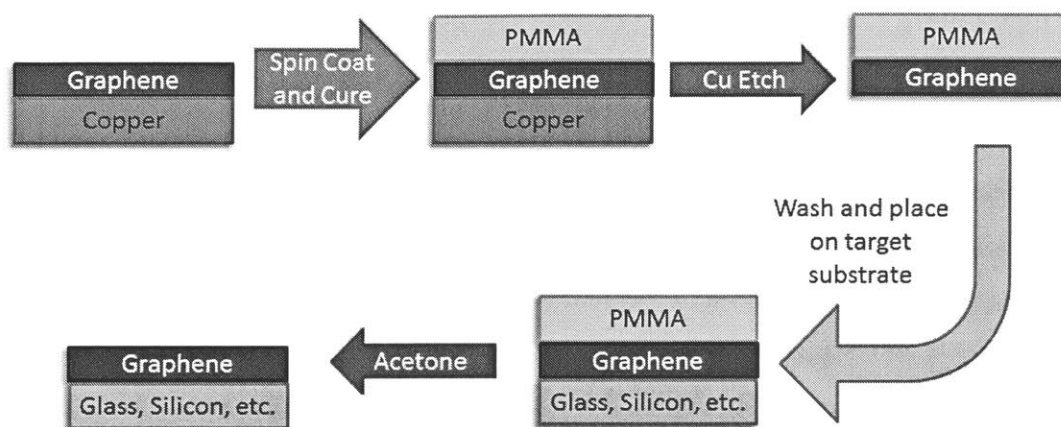
Figure 6-1: Schematic of PMMA based 2D materials transfer for graphene grown on copper foils. A PMMA stamp is deposited from solution and etchant is used to release the 2D material and polymer from the growth substrate. After cleaning with water, the sample is placed onto the target substrate, and the polymer is removed with warm acetone.

The samples were then floated on 10 % HF to remove the underlying native or thermal oxide. After the etching process was complete, the wafers were lightly disturbed to sever the PMMA along the scratches and causing the wafer to submerge. Finally, the PMMA film was coupled with a glass slide onto DI water for cleaning and finally onto the target substrate. The transferred films were dried at $40°C$ and the PMMA was removed with warm acetone.

6.5   Characterization Methods

Thermogravimetric analysis was performed using TA Instruments Q500 TGA. Approximately 40 mg of as received coal powder was placed on a platinum pan and maintained at $100°C$ for 60 min to remove any moisture and then ramped to $950°C$ at a rate of $10°C/min$. Optical absorption spectroscopy was performed with an Agilent Carry 60 UV-Vis spectrometer over the range of 1100 to 200 nm. X-ray photoluminescence spectroscopy was performed over regions 400 μm in diameter using a Thermo Scientific K-Alpha XPS with Aluminum K radiation. SEM was performed on a Zeiss Ultra55 or a Helios Nanolab 600, both operated at 5 kV. An Agilent 4155C and

lakeshore TTP4 probe station with liquid N_2 cooling was used for the majority of the low temperature characterization. All room temperature electrical characterization was done under air and all low temperature characterization under vacuum. Joule heating measurements were performed using a FLIR AX5 camera with emissivity set to 0.93.

6.5.1 Raman Spectroscopy

Micro-Raman spectra were acquired using a Horiba LabRAM 800 HR spectrometer equipped with a 632.8 nm excitation source for cabonacous materials and a 514.5 nm excitation source for TMD materials. The laser spot on the sample was 800 nm in diameter and had a power of 4 mW at the sample surface. For carbonaceous materials, the full spectral window for each acquisition is from -50 to 2850 cm^{-1}. In order to reduce the amount of artifacts introduced by the background subtraction, the spectrum was broken down into several regions of interest. The first-order spectral window for the organic region was taken from 1000 to 1800 cm^{-1}, and background subtraction in this spectral window was performed using 2nd order polynomial functions.

Raman spectroscopy is a powerful tool for quickly identifying the number and quality of layers of 2D materials. The phonon structure, relevant electronic transitions, and a Raman spectrum from literature showing the primary graphene associated peaks is shown in Figure 6-2. The G band is common to graphene samples of all layer count and is associated with the doubly degenerate iTO and iLO bands at the Γ point. It is the only peak which occurs from a normal first order Raman process (Fig. 15a) and is typically located between 1582 cm^{-1} in graphite and 1589 cm^{-1} in graphene. There are two peaks associated with defects in the graphene lattice: the D and D' peaks. The D peak involves intervalley scattering by a single iTO phonon near the K point and an elastic scattering event involving a defect. The D' peak occurs by a similar intravalley process involving an iLO phonon and a defect. Scattering by two iTO phonons is also possible and may occur by either a double or triple resonance process as shown in figure 15a to produce the G' peak. Because of the pair of inelastic events, the G' peak appears at twice the Raman shift as the D peak, and
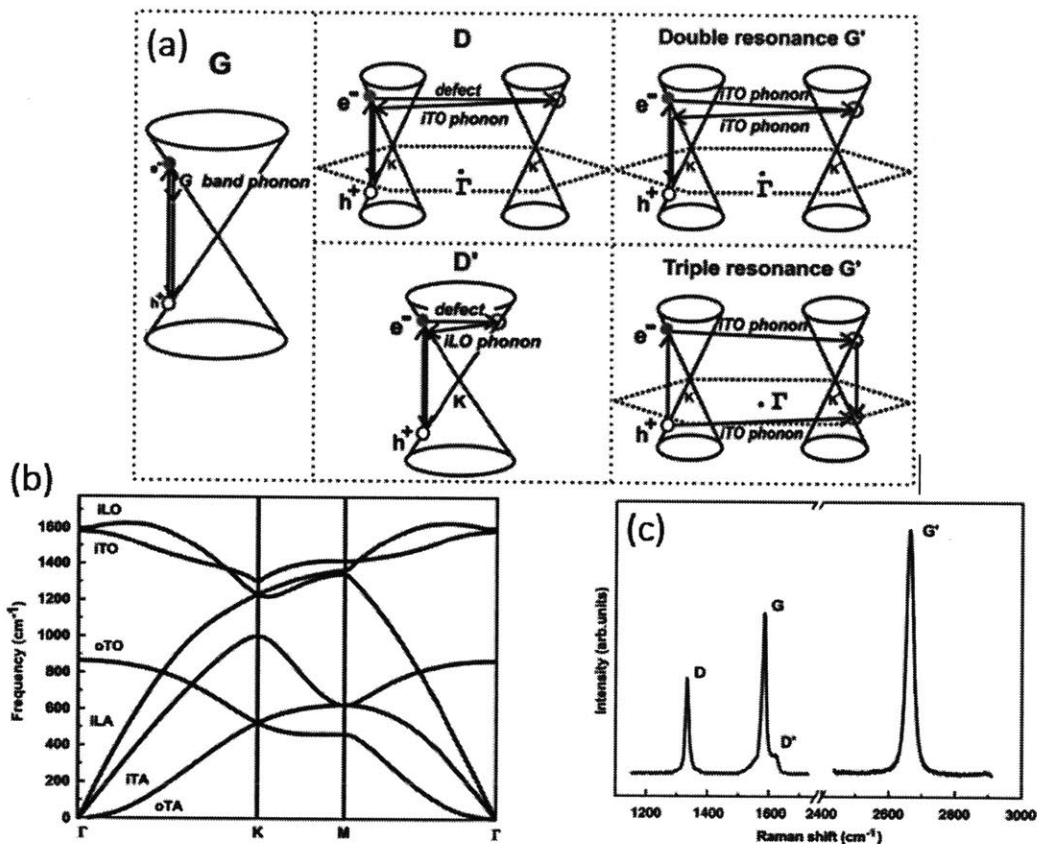
Figure 6-2: Raman spectra on graphitic materials. (a) Electron, hole, and phonon interactions which give rise to key Raman features. (b) Phonon structure of graphene. (c) Raman spectrum of graphene showing key features. Reproduced from reference [145].

so it is typically referred to as the 2D peak. The 2D peak is very sensitive to the number of layers in the graphene sample. For monolayer graphene, it forms a single Lorentzian peak of height greater than the G peak. As the layer count increases, the magnitude is greatly reduced, and due to the splitting of the electronic and phonon bands, it becomes a super position of several smaller peaks depending on the layer count [145].

However, in extremely disordered samples, the D peak becomes more complex with aliphatic, and other contributions beyond defect modes in aromatic systems. Because the G peak intensity is primarily contributed from all sp^2 bond bonds but the primary D peak contribution comes from defective aromatic systems, for carbon
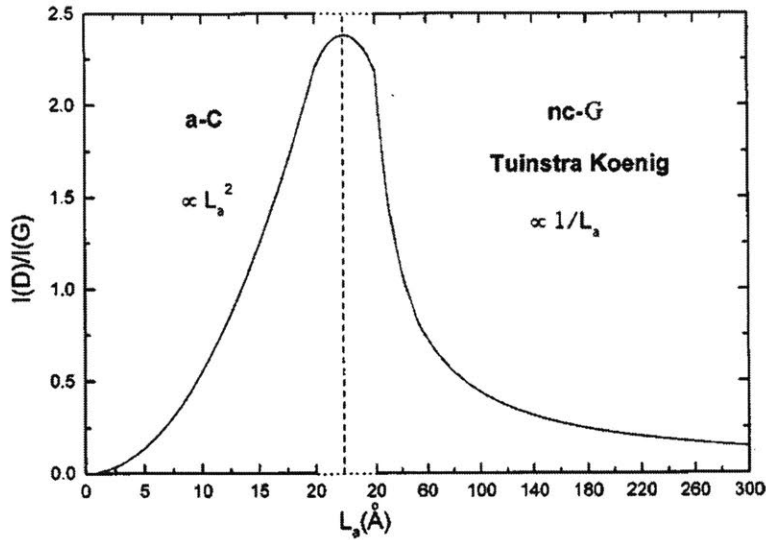
Figure 6-3: Approximate relationsip between the ratio of the D and G scattering intensities, as a function of defect correlation length. Reproduced from reference [85].

materials with very small (< 2-3 nm) correlation distances between aromatic defects, the D peak increases as the size of aromatic carbon domains increases as the average distance to the edge of an aromatic patch decreases for an sp^2 bond (Figure 6-3).

The two strongest Raman Scattering modes are the E_{2g}^1 and A_{1g}. They change frequency strongly with the number of layers making them an excellent method for validating TMD thickness (Figure 6-4). Specifically the E_{2g}^1 vibration blueshifts from 382 to 384.5 cm^{-1} and the A_{1g} redshifts from 405 to 403 cm^{-1} as the material thins from bulk to monolayer. This phenomenon makes the difference between those frequencies a particularly useful indicator of layer number. Ranging from 17 to 20 cm^{-1} for monolayer MoS2 to 25 cm^{-1} in the bulk.
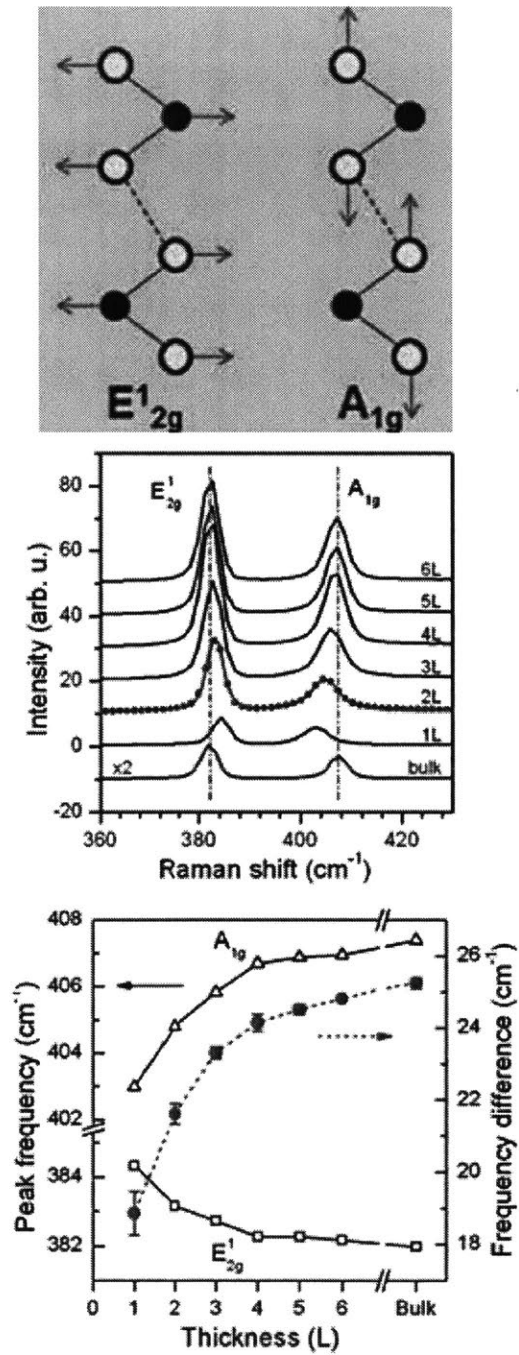
Figure 6-4: Raman spectra on TMD materials. (a) Schematic of strongest scattering Raman active modes in MoS_2 (b) Raman spectra of bulk and few layer MoS_2. (c) Frequency postions and difference between them for A_{1g} and E_{2g}^1 peaks of MoS_2 for different numbers of layers. Reproduced from reference [14].

Chapter 7

Conclusions and Discussion

Technological advances are critical to meeting both defining challenges of this century and also to equally complex challenges in devices which simply offer to continue improving the human experience. These new technologies are often dependent on new materials which provide solutions to design questions that otherwise lack solutions. I have worked in two exciting materials spaces: 2D materials and natural carbon materials. In both I have worked to develop methods of processing which leverage the inherent advantages of the materials for ultimate use in exciting applications. I have also characterized these materials to build a deep understanding of the connections between processing and properties at a structural level. Finally, I have identified the properties of most use for devices and fabricate those proof of concept strucutres.

Electronic devices from natural carbon materials was an entirely novel idea. To understand a material which is complex and diverse in both structures and chemistries is difficult task, but the potential rewards are tremendous. Many synthetic carbon materials were once heralded as the keys to ultra-low cost flexible photovoltaics or the successor materials to silicon in digital logic. Ultimately all of the materials have brought great strengths in processing, properties, and/or tenability, but have suffered from key weakness in stability or cost. But as a materials space these weakness are not shared. rGO and organic small molecules can be very cheap, and graphene and carbon nanotubes extremely stable. My work has begun the process of characterizing, tuning, and fabricating devices from these natural carbon materials. I have charac-

terized the properties including optical absorbance, conductivity, charge transport mechanism, and band alignment of thin films of several natural carbon materials. The potential to tune these materials to very high conductivity enabled me to fabricate high performance Joule heating devices competitive with the leading synthetic options.

Natural carbon materials sit a rich intersection. They share chemistries with all of the carbon systems. They can be large sp^2 ring systems or small organic soups. They are low cost and phase space to choose from is massive. Future research will continue to answer the question: Can the rich natural carbon phase space leverage the strengths of synthetic carbon materials to overcome their weaknesses? For what applications are these materials best suited?

In contrast to natural carbon for electronic devices, 2D materials have been extensively studied by many groups in the last decade. The materials sit at an ultimate limit for device thinness and the reduce dimensionality offers unique physics. To leverage these materials, deposition methods must provide the level of control demanded by the material – a film uniformly 3 atoms thick. I have studied the nucleation ALD regime of MoO_3 and post processing chemistry to develop a process which leverages the control of atomic layer deposition to fabricate continuous large area films of monolayer MoS_2. I have also worked on methods of cleaning solution processed TMDs which use cholate as a stabilizing ligand and used scotch tape exfoliated MoS_2 to demonstrate charge separation in MoS_2 and graphene heterojunctions.

Bibliography

[1] G. Li, R. Zhu, and Y. Yang, "Polymer solar cells," *Nat. Photonics*, vol. 6, no. 3, pp. 153–161, 2012.

[2] M. Bernardi, J. Lohrman, P. V. Kumar, A. Kirkeminde, N. Ferralis, J. C. Grossman, and S. Ren, "Nanocarbon-based photovoltaics.," *ACS nano*, vol. 6, pp. 8896–903, oct 2012.

[3] M. P. Ramuz, M. Vosgueritchian, P. Wei, C. Wang, Y. Gao, Y. Wu, Y. Chen, and Z. Bao, "Evaluation of Solution-Processable Carbon-Based Electrodes for All Carbon Solar Cells," *ACS Nano*, no. 11, pp. 10384–10395, 2012.

[4] R. M. Jain, R. Howden, K. Tvrdy, S. Shimizu, A. J. Hilmer, T. P. McNicholas, K. K. Gleason, and M. S. Strano, "Polymer-free near-infrared photovoltaics with single chirality (6,5) semiconducting carbon nanotube active layers," *Advanced Materials*, vol. 24, no. 32, pp. 4436–4439, 2012.

[5] V. C. Tung, J.-H. Huang, J. Kim, A. J. Smith, C.-W. Chu, and J. Huang, "Towards solution processed all-carbon solar cells: a perspective," *Energy & Environmental Science*, vol. 5, no. 7, p. 7810, 2012.

[6] M. Gong, T. A. Shastry, Y. Xie, M. Bernardi, D. Jasion, K. A. Luck, T. J. Marks, J. C. Grossman, S. Ren, and M. C. Hersam, "Polychiral semiconducting carbon nanotube-fullerene solar cells," *Nano Letters*, vol. 14, no. 9, pp. 5308–5314, 2014.

[7] J. P. Mathews and A. L. Chaffee, "The molecular representations of coal - A review," *Fuel*, vol. 96, no. August 2016, pp. 1–14, 2012.

[8] D. Ginley and D. Cahen, *Fundamentals of Materials for Energy and Environmental Sustainability.* 2012.

[9] J. H. Shinn, "From coal to single-stage and two-stage products: A reactive model of coal structure," *Fuel*, vol. 63, no. 9, pp. 1187–1196, 1984.

[10] K. S. Novoselov, a. K. Geim, S. V. Morozov, D. Jiang, Y. Zhang, S. V. Dubonos, I. V. Grigorieva, and a. a. Firsov, "Electric field effect in atomically thin carbon films.," *Science*, vol. 306, pp. 666–9, oct 2004.

[11] K. Bolotin, K. Sikes, Z. Jiang, M. Klima, G. Fudenberg, J. Hone, P. Kim, and H. Stormer, "Ultrahigh electron mobility in suspended graphene," *Solid State Communications*, vol. 146, pp. 351–355, jun 2008.

[12] X. Li, W. Cai, J. An, S. Kim, J. Nah, D. Yang, R. Piner, A. Velamakanni, I. Jung, E. Tutuc, S. K. Banerjee, L. Colombo, and R. S. Ruoff, "Large-area synthesis of high-quality and uniform graphene films on copper foils.," *Science*, vol. 324, pp. 1312–1314, jun 2009.

[13] K. S. Kim, Y. Zhao, H. Jang, S. Y. Lee, J. M. Kim, K. S. Kim, J.-H. Ahn, P. Kim, J.-Y. Choi, and B. H. Hong, "Large-scale pattern growth of graphene films for stretchable transparent electrodes.," *Nature*, vol. 457, pp. 706–10, feb 2009.

[14] C. Lee, H. Yan, L. Brus, T. Heinz, J. Hone, and S. Ryu, "Anomalous lattice vibrations of single-and few-layer MoS2," *ACS nano*, vol. 4, no. 5, pp. 2695–700, 2010.

[15] S. Bae, H. Kim, Y. Lee, X. Xu, J.-S. Park, Y. Zheng, J. Balakrishnan, T. Lei, H. R. Kim, Y. I. Song, Y.-J. Kim, K. S. Kim, B. Ozyilmaz, J.-H. Ahn, B. H. Hong, and S. Iijima, "Roll-to-roll production of 30-inch graphene films for transparent electrodes.," *Nature Nanotechnology*, vol. 5, pp. 574–8, aug 2010.

[16] X. Li, C. W. Magnuson, A. Venugopal, J. An, J. W. Suk, B. Han, M. Borysiak, W. Cai, A. Velamakanni, Y. Zhu, L. Fu, E. M. Vogel, E. Voelkl, L. Colombo, and R. S. Ruoff, "Graphene films with large domain size by a two-step chemical vapor deposition process.," *Nano Letters*, vol. 10, pp. 4328–34, nov 2010.

[17] S. Bhaviripudi, X. Jia, M. S. Dresselhaus, and J. Kong, "Role of kinetic factors in chemical vapor deposition synthesis of uniform large area graphene using copper catalyst.," *Nano Letters*, vol. 10, pp. 4128–33, oct 2010.

[18] F. Schwierz, "Graphene transistors.," *Nature Nanotech*, vol. 5, no. 7, pp. 487–96, 2010.

[19] R. Balog, B. Jørgensen, L. Nilsson, M. Andersen, E. Rienks, M. Bianchi, M. Fanetti, E. Laegsgaard, A. Baraldi, S. Lizzit, Z. Sljivancanin, F. Besenbacher, B. Hammer, T. G. Pedersen, P. Hofmann, and L. Hornekaer, "Bandgap opening in graphene induced by patterned hydrogen adsorption.," *Nature Materials*, vol. 9, pp. 315–9, apr 2010.

[20] D. Haberer, D. V. Vyalikh, S. Taioli, B. Dora, M. Farjam, J. Fink, D. Marchenko, T. Pichler, K. Ziegler, S. Simonucci, M. S. Dresselhaus, M. Knupfer, B. Büchner, and A. Grüneis, "Tunable band gap in hydrogenated quasi-free-standing graphene.," *Nano Letters*, vol. 10, pp. 3360–6, sep 2010.

[21] D. Elias, R. Nair, and T. Mohiuddin, "Control of graphene's properties by reversible hydrogenation: evidence for graphane," *Science*, no. January, pp. 610–613, 2009.

[22] S.-H. Cheng, K. Zou, F. Okino, H. R. Gutierrez, a. Gupta, N. Shen, P. C. Eklund, J. O. Sofo, and J. Zhu, "Reversible fluorination of graphene: Evidence of a two-dimensional wide bandgap semiconductor," *Physical Review B*, vol. 81, p. 205435, may 2010.

[23] K.-J. Jeon, Z. Lee, E. Pollak, L. Moreschini, A. Bostwick, C.-M. Park, R. Mendelsberg, V. Radmilovic, R. Kostecki, T. J. Richardson, and E. Rotenberg, "Fluorographene: a wide bandgap semiconductor with ultraviolet luminescence.," *ACS Nano*, vol. 5, pp. 1042–6, feb 2011.

[24] J. T. Robinson, J. S. Burgess, C. E. Junkermeier, S. C. Badescu, T. L. Reinecke, F. K. Perkins, M. K. Zalalutdniov, J. W. Baldwin, J. C. Culbertson, P. E. Sheehan, and E. S. Snow, "Properties of fluorinated graphene films.," *Nano Letters*, vol. 10, pp. 3001–5, aug 2010.

[25] E. Bekyarova, M. E. Itkis, P. Ramesh, C. Berger, M. Sprinkle, W. a. de Heer, and R. C. Haddon, "Chemical modification of epitaxial graphene: spontaneous grafting of aryl groups.," *Journal of the American Chemical Society*, vol. 131, pp. 1336–7, feb 2009.

[26] P. Huang, H. Zhu, L. Jing, Y. Zhao, and X. Gao, "Graphene covalently binding aryl groups: conductivity increases rather than decreases.," *ACS Nano*, vol. 5, pp. 7945–9, oct 2011.

[27] S. Niyogi, E. Bekyarova, J. Hong, S. Khizroev, C. Berger, W. de Heer, and R. C. Haddon, "Covalent Chemistry for Graphene Electronics," *The Journal of Physical Chemistry Letters*, vol. 2, pp. 2487–2498, oct 2011.

[28] S. Niyogi, E. Bekyarova, M. E. Itkis, H. Zhang, K. Shepperd, J. Hicks, M. Sprinkle, C. Berger, C. N. Lau, W. a. DeHeer, E. H. Conrad, and R. C. Haddon, "Spectroscopy of covalently functionalized graphene.," *Nano Letters*, vol. 10, pp. 4061–6, oct 2010.

[29] K. S. Novoselov, D. Jiang, F. Schedin, T. J. Booth, V. V. Khotkevich, S. V. Morozov, and A. K. Geim, "Two-dimensional atomic crystals," *Proceedings of the National Academy of Sciences of the United States of America*, vol. 102, no. 30, pp. 10451–10453, 2005.

[30] K. Mak, C. Lee, J. Hone, J. Shan, and T. Heinz, "Atomically Thin MoS2: A New Direct-Gap Semiconductor," *Physical Review Letters*, vol. 105, pp. 2–5, sep 2010.

[31] A. Splendiani, L. Sun, Y. Zhang, T. Li, J. Kim, C.-Y. Chim, G. Galli, and F. Wang, "Emerging photoluminescence in monolayer MoS2.," *Nano Letters*, vol. 10, pp. 1271–5, apr 2010.

[32] H. Shi, H. Pan, Y.-W. Zhang, and B. I. Yakobson, "Quasiparticle band structures and optical properties of strained monolayer MoS$_2$ and WS$_2$," *Physical Review B*, vol. 87, no. 15, p. 155304, 2013.

[33] B. Radisavljevic, A. Radenovic, J. Brivio, V. Giacometti, and A. Kis, "Single-layer MoS2 transistors.," *Nature Nanotechnology*, vol. 6, pp. 147–50, mar 2011.

[34] K. Dolui, I. Rungger, C. Das Pemmaraju, and S. Sanvito, "Possible doping strategies for MoS_{2} monolayers: An ab initio study," *Physical Review B*, vol. 88, p. 075420, aug 2013.

[35] K. Dolui, I. Rungger, and S. Sanvito, "Origin of the n-type and p-type conductivity of MoS 2 monolayers on a SiO 2 substrate," *Physical Review B*, vol. 87, 2013.

[36] H. Wang, L. Yu, Y.-H. Lee, Y. Shi, A. Hsu, M. L. Chin, L.-J. Li, M. Dubey, J. Kong, and T. Palacios, "Integrated circuits based on bilayer MoS2 transistors.," *Nano letters*, vol. 12, pp. 4674–80, oct 2012.

[37] Y.-H. Lee, X.-Q. Zhang, W. Zhang, M.-T. Chang, C.-T. Lin, K.-D. Chang, Y.-C. Yu, J. T.-W. Wang, C.-S. Chang, L.-J. Li, and T.-W. Lin, "Synthesis of large-area MoS2 atomic layers with chemical vapor deposition.," *Advanced Materials*, vol. 24, pp. 2320–5, may 2012.

[38] Z. Zeng, Z. Yin, X. Huang, H. Li, Q. He, G. Lu, F. Boey, and H. Zhang, "Single-layer semiconducting nanosheets: high-yield preparation and device fabrication.," *Angewandte Chemie (International ed. in English)*, vol. 50, pp. 11093–7, dec 2011.

[39] Y. Zhan, Z. Liu, S. Najmaei, P. M. Ajayan, and J. Lou, "Large-area vapor-phase growth and characterization of MoS(2) atomic layers on a SiO(2) substrate.," *Small (Weinheim an der Bergstrasse, Germany)*, vol. 8, pp. 966–71, apr 2012.

[40] Q. H. Wang, K. Kalantar-Zadeh, A. Kis, J. N. Coleman, and M. S. Strano, "Electronics and optoelectronics of two-dimensional transition metal dichalcogenides.," *Nature nanotechnology*, vol. 7, pp. 699–712, nov 2012.

[41] K. Mak, K. He, J. Shan, and T. Heinz, "Control of valley polarization in monolayer MoS2 by optical helicity," *Nature Nanotechnology*, vol. 7, pp. 494–498, 2012.

[42] H. Zeng, J. Dai, W. Yao, D. Xiao, and X. Cui, "Valley polarization in MoS2 monolayers by optical pumping," *Nature Nanotechnology*, vol. 7, no. 8, pp. 490–493, 2012.

[43] M. Bernardi, M. Palummo, and J. C. Grossman, "Extraordinary Sunlight Absorption and 1 nm-Thick Photovoltaics using Two-Dimensional Monolayer Materials," *Nano Letters*, jun 2013.

[44] L. Britnell, R. M. Ribeiro, a. Eckmann, R. Jalil, B. D. Belle, a. Mishchenko, Y.-J. Kim, R. V. Gorbachev, T. Georgiou, S. V. Morozov, a. N. Grigorenko, a. K. Geim, C. Casiraghi, a. H. Castro Neto, and K. S. Novoselov, "Strong light-matter interactions in heterostructures of atomically thin films.," *Science (New York, N.Y.)*, vol. 340, pp. 1311–4, jun 2013.

[45] M. Fontana, T. Deppe, A. K. Boyd, M. Rinzan, A. Y. Liu, M. Paranjape, and P. Barbara, "Electron-hole transport and photovoltaic effect in gated MoS2 Schottky junctions.," *Scientific reports*, vol. 3, p. 1634, jan 2013.

[46] Y. Lee, J. Lee, H. Bark, I.-K. Oh, G. H. Ryu, Z. Lee, H. Kim, J. H. Cho, J.-H. Ahn, and C. Lee, "Synthesis of wafer-scale uniform molybdenum disulfide films with control over the layer number using a gas phase sulfur precursor," *Nanoscale*, vol. 6, no. 5, p. 2821, 2014.

[47] Y.-H. Lee, L. Yu, H. Wang, W. Fang, X. Ling, Y. Shi, C.-T. Lin, J.-K. Huang, M.-T. Chang, C.-S. Chang, M. S. Dresselhaus, T. Palacios, L.-J. Li, and J. Kong, "Synthesis and Transfer of Single Layer Transition Metal Disulfides on Diverse Surfaces.," *Nano letters*, mar 2013.

[48] Q. Ji, Y. Zhang, T. Gao, Y. Zhang, D. Ma, M. Liu, Y. Chen, X. Qiao, P.-H. Tan, M. Kan, J. Feng, Q. Sun, and Z. Liu, "Epitaxial monolayer MoS2 on mica with novel photoluminescence.," *Nano letters*, vol. 13, pp. 3870–7, aug 2013.

[49] X. Huang, Z. Zeng, and H. Zhang, "Metal dichalcogenide nanosheets: preparation, properties and applications.," *Chemical Society reviews*, vol. 42, pp. 1934–46, mar 2013.

[50] J. Mun, D. Kim, J. Yun, Y. Shin, S. Kang, and T. Kim, "Chemical Vapor Deposition of MoS2 Films," *ECS Transactions*, vol. 58, no. 7, pp. 199–202, 2013.

[51] T. Scharf, S. Prasad, T. Mayer, R. Goeke, and M. Dugger, "Atomic layer deposition of tungsten disulphide solid lubricant thin films," *Journal of Materials Research*, vol. 19, pp. 3443–3446, mar 2011.

[52] H. R. Gutiérrez, N. Perea-López, A. L. Elías, A. Berkdemir, B. Wang, R. Lv, F. López-Urías, V. H. Crespi, H. Terrones, and M. Terrones, "Extraordinary Room-Temperature Photoluminescence in Triangular WS2 Monolayers.," *Nano Letters*, dec 2012.

[53] J.-g. Song, J. Park, W. Lee, T. Choi, H. Jung, C. W. Lee, S.-h. Hwang, J. M. Myoung, J.-h. Jung, S.-h. Kim, C. Lansalot-matras, and H. Kim, "Conformal Synthesis of Tungsten Disulfide Nanosheets Using Atomic Layer Deposition," pp. 11333–11340, 2013.

[54] J.-G. Song, G. H. Ryu, S. J. Lee, S. Sim, C. W. Lee, T. Choi, H. Jung, Y. Kim, Z. Lee, J.-M. Myoung, C. Dussarrat, C. Lansalot-Matras, J. Park, H. Choi, and H. Kim, "Controllable synthesis of molybdenum tungsten disulfide alloy for vertically composition-controlled multilayer.," *Nature communications*, vol. 6, p. 7817, 2015.

[55] S. M. George, "Atomic layer deposition: An overview," *Chemical Reviews*, vol. 110, no. 1, pp. 111–131, 2010.

[56] D. D. L. Chung, "Electrical applications of carbon materials," *J. Mater. Sci.*, vol. 39, pp. 2645–2661, 2004.

[57] K. Persson, Y. Hinuma, Y. Meng, A. Van der Ven, and G. Ceder, "Thermodynamic and kinetic properties of the Li-graphite system from first-principles calculations," *Physical Review B*, vol. 82, no. 12, p. 125416, 2010.

[58] E. Buiel and J. R. Dahn, "Li-insertion in hard carbon anode materials for Li-ion batteries," *Electrochimica Acta*, vol. 45, no. 1, pp. 121–130, 1999.

[59] H. Zheng, Q. Qu, L. Zhang, G. Liu, and V. S. Battaglia, "Hard carbon: a promising lithium-ion battery anode for high temperature applications with ionic electrolyte," *RSC Advances*, vol. 2, no. 11, p. 4904, 2012.

[60] K. K. Chan, G. a. J. Amaratunga, Z. a. Shafi, P. Ashburn, and S. P. Wong, "Bipolar transistor action from an amorphous carbon/silicon heterojunction emitter," *Diamond and Related Materials*, vol. 2, pp. 1445–1448, 1993.

[61] A. Ilie, N. Conway, B. Kleinsorge, J. Robertson, and W. Milne, "Photoconductivity and electronic transport in tetrahedral amorphous carbon and hydrogenated tetrahedral amorphous carbon," *Journal of Applied Physics*, vol. 84, no. 1998, pp. 5575–5582, 1998.

[62] Z. Q. Ma and B. X. Liu, "Boron-doped diamond-like amorphous carbon as photovoltaic films in solar cell," *Solar Energy Materials and Solar Cells*, vol. 69, no. 4, pp. 339–344, 2001.

[63] A. N. Fadzilah, K. Dayana, and M. Rusop, "New method of depositing the nanostructured amorphous carbon for carbon based solar cell applications," *International Journal of Photoenergy*, vol. 2013, no. 784743, pp. 1–7, 2013.

[64] X. Wang, L. Zhi, and K. Müllen, "Transparent, conductive graphene electrodes for dye-sensitized solar cells," *Nano Letters*, vol. 8, no. 1, pp. 323–327, 2008.

[65] Z. Yin, S. Sun, T. Salim, S. Wu, X. Huang, Q. He, Y. M. Lam, and H. Zhang, "Organic photovoltaic devices using highly flexible reduced graphene oxide films as transparent electrodes," *ACS Nano*, vol. 4, no. 9, pp. 5263–5268, 2010.

[66] H. A. Becerril, J. Mao, Z. Liu, R. M. Stoltenberg, Z. Bao, and Y. Chen, "Evaluation of solution-processed reduced graphene oxide films as transparent conductors," *ACS Nano*, vol. 2, no. 3, pp. 463–470, 2008.

[67] G. Eda, G. Fanchini, and M. Chhowalla, "Large-area ultrathin films of reduced graphene oxide as a transparent and flexible electronic material.," *Nature nanotechnology*, vol. 3, no. 5, pp. 270–274, 2008.

[68] A. Reina, X. Jia, J. Ho, D. Nezich, H. Son, V. Bulovic, M. S. Dresselhaus, and J. Kong, "Large area , few-layer graphene films on arbitrary substrates by chemical vapor deposition," *Nano letters*, vol. 9, no. 1, pp. 30–35, 2009.

[69] X. Li, Y. Zhu, W. Cai, M. Borysiak, B. Han, D. Chen, R. D. Piner, L. Colombo, and R. S. Ruoff, "Transfer of large-area graphene films for high-performance transparent conductive electrodes," *Nano Letters*, vol. 9, no. 12, pp. 4359–4363, 2009.

[70] K. Maize, S. R. Das, S. Sadeque, A. M. S. Mohammed, A. Shakouri, D. B. Janes, and M. A. Alam, "Super-Joule heating in graphene and silver nanowire network," *Applied Physics Letters*, vol. 106, no. 14, 2015.

[71] A.-r. O. Raji, T. Varadhachary, K. Nan, T. Wang, J. Lin, B. Genorio, Y. Zhu, C. Kittrell, and J. M. Tour, "Composites of Graphene Nanoribbon Stacks and Epoxy for Joule Heating and Deicing of Surfaces," *ACS Applied Materials and Interfaces*, 2015.

[72] D. Sui, Y. Huang, L. Huang, J. Liang, Y. Ma, and Y. Chen, "Flexible and transparent electrothermal film heaters based on graphene materials," *Small*, vol. 7, no. 22, pp. 3186–3192, 2011.

[73] G. Kuhner and V. Manfred, "Manufacture of Carbon Black," in *Carbon Black Science and Technology* (J.-B. Donnet, R. C. Bansal, and W. Meng-Jiao, eds.), pp. 1–66, 1993.

[74] J. Robertson, "Amorphous carbon," *Advances in Physics*, vol. 35, pp. 317–374, 1986.

[75] M. Weiler, S. Sattel, T. Giessen, K. Jung, H. Ehrhardt, V. Veerasamy, and J. Robertson, "Preparation and properties of highly tetrahedral hydrogenated amorphous carbon," *Physical Review B*, vol. 53, no. 3, pp. 1594–1608, 1996.

[76] J.-H. Lee, E. K. Lee, W.-j. Joo, Y. Jang, B.-s. Kim, J. Y. Lim, S.-H. Choi, S. J. Ahn, J. R. Ahn, M.-h. Park, C.-w. Yang, B. L. Choi, S.-w. Hwang, and D. Whang, "Wafer-scale growth of single-crystal monolayer graphene on reusable hydrogen-terminated germanium.," *Science (New York, N.Y.)*, vol. 344, no. 6181, pp. 286–9, 2014.

[77] H. Zhou, W. J. Yu, L. Liu, R. Cheng, Y. Chen, X. Huang, Y. Liu, Y. Wang, Y. Huang, and X. Duan, "Chemical vapour deposition growth of large single crystals of monolayer and bilayer graphene.," *Nature communications*, vol. 4, p. 2096, 2013.

[78] US Energy Information Administration, "Annual Energy Review," 2012.

[79] D. G. Levine, R. H. Schlosberg, and B. G. Silbernagel, "Understanding the chemistry and physics of coal structure (A Review)," *Proceedings of the National Academy of Sciences of the United States of America*, vol. 79, no. 10, pp. 3365–3370, 1982.

[80] H. Dindi, X.-h. Bai, and W. B. Krantz, "Thermal and electrical property measurements for coal," *Fuel*, vol. 68, no. 2, pp. 185–192, 1989.

[81] A. G. Duba, "Electrical conductivity of coal and coal char," *Fuel*, vol. 56, no. 4, pp. 441–443, 1977.

[82] B. D. Keller, N. Ferralis, and J. C. Grossman, "Rethinking Coal: Thin Films of Solution Processed Natural Carbon Nanoparticles for Electronic Devices.," *Nano Letters*, p. acs.nanolett.5b04735, 2016.

[83] *The Penn State Coal Sample Bank And Database.* 1998.

[84] J. W. Cumming and J. McLaughlin, "The thermogravimetric behaviour of coal," *Thermochimica Acta*, vol. 57, no. 3, pp. 253–272, 1982.

[85] A. C. Ferrari and J. Robertson, "Interpretation of Raman spectra of disordered and amorphous carbon," *Physical Review B*, vol. 61, pp. 14095–14107, may 2000.

[86] A. Ferrari and J. Robertson, "Resonant Raman spectroscopy of disordered, amorphous, and diamondlike carbon," *Physical Review B*, vol. 64, no. 7, p. 075414, 2001.

[87] F. Tuinstra and J. L. Koenig, "Raman Spectrum of Graphite," *The Journal of Chemical Physics*, vol. 53, no. 3, p. 1126, 1970.

[88] M. Lucchese, F. Stavale, E. M. Ferreira, C. Vilani, M. Moutinho, R. B. Capaz, C. Achete, and a. Jorio, "Quantifying ion-induced defects and Raman relaxation length in graphene," *Carbon*, vol. 48, pp. 1592–1597, apr 2010.

[89] A. C. Ferrari and D. M. Basko, "Raman spectroscopy as a versatile tool for studying the properties of graphene.," *Nature nanotechnology*, vol. 8, no. 4, pp. 235–46, 2013.

[90] H. Kuzmany, R. Pfeiffer, N. Salk, and B. Günther, "The mystery of the 1140 cm-1 Raman line in nanocrystalline diamond films," *Carbon*, vol. 42, no. 5-6, pp. 911–917, 2004.

[91] J. Tauc, R. Grigorovic, and a. Vancu, "Optical properties and electronic structure of amorphous germanium," *Physica Status Solidi (B)*, vol. 15, no. 2, pp. 627–637, 1966.

[92] E. a. Davis and N. F. Mott, "Conduction in non-crystalline systems V. Conductivity, optical absorption and photoconductivity in amorphous semiconductors," *Philosophical Magazine*, vol. 22, no. 179, pp. 0903–0922, 1970.

[93] J. Robertson, "Hard amorphous (diamond-like) carbons," *Progress in Solid State Chemistry*, vol. 21, no. 4, pp. 199–333, 1991.

[94] J. Robertson and E. O'Reilly, "Electronic and atomic structure of amorphous carbon," *Physical Review B*, vol. 35, no. 6, pp. 2946–2957, 1987.

[95] J. Sánchez-González, a. Macías-García, M. Alexandre-Franco, and V. Gómez-Serrano, "Electrical conductivity of carbon blacks under compression," *Carbon*, vol. 43, no. 4, pp. 741–747, 2005.

[96] N. Probst, "Conducting Carbon Black," in *Carbon Black Science and Technology* (J.-b. Donnet, R. C. Bansal, and M.-J. Wang, eds.), pp. 271–288, 1993.

[97] N.-H. Cho, K. M. Krishnan, D. K. Veirs, M. D. Rubin, C. B. Hopper, B. Bhushan, and D. B. Bogy, "Chemical structure and physical properties of diamond-like amorphous carbon films prepared by magnetron sputtering," *Journal of Materials Research*, vol. 5, no. 11, pp. 2543–2554, 1990.

[98] D. I. Jones and a. D. Stewart, "Properties of hydrogenated amorphous carbon films and the effects of doping," *Philosophical Magazine B*, vol. 46, no. 5, pp. 423–434, 1982.

[99] Y. S. Park, H. J. Cho, and B. Hong, "Characteristics of Conductive Amorphous Carbon (a-C) Films Prepared by Using the Magnetron Sputtering Method," *Journal of the Korean Physical Society*, vol. 51, no. 3, p. 1119, 2007.

[100] N. Savvides, "Optical constants and associated functions of metastable diamondlike amorphous carbon films in the energy range 0.5-7.3 eV," *Journal of Applied Physics*, vol. 59, no. 12, pp. 4133–4145, 1986.

[101] N. Apsley and H. P. Hughes, "Temperature- and field-dependence of hopping conduction in disordered systems," *Philosophical Magazine*, vol. 31, no. 6, pp. 1327–1339, 1975.

[102] G. Eda, C. Mattevi, H. Yamaguchi, H. Kim, and M. Chhowalla, "Insulator to semimetal transition in graphene oxide," *Journal of Physical Chemistry C*, vol. 113, no. 35, pp. 15768–15771, 2009.

[103] A. B. Kaiser, G. N. Cristina, R. S. Sundaram, M. Burghard, and K. Kern, "Electrical conduction mechanism in chemically derived graphene monolayers," *Nano Letters*, vol. 9, no. 5, pp. 1787–1792, 2009.

[104] J. J. Hauser, "Hopping Conductivity in Amophous Carbon Films," *Solid State Communications*, vol. 17, pp. 1577–1580, 1975.

[105] K. Miyake and K. Shimakawa, "Hopping transport of localized n. electrons in amorphous carbon films," *Phys. Rev. B*, vol. 39, no. 11, pp. 7S78–7584, 1989.

[106] A. M. Hussain, E. B. Lizardo, G. A. Torres Sevilla, J. M. Nassar, and M. M. Hussain, "Ultrastretchable and flexible copper interconnect-based smart patch for adaptive thermotherapy," *Advanced Healthcare Materials*, vol. 4, no. 5, pp. 665–673, 2015.

[107] D. H. Kim, S. Wang, H. Keum, R. Ghaffari, Y. S. Kim, H. Tao, B. Panilaitis, M. Li, Z. Kang, F. Omenetto, Y. Huang, and J. A. Rogers, "Thin, flexible sensors and actuators as 'instrumented' surgical sutures for targeted wound monitoring and therapy," *Small*, vol. 8, no. 21, pp. 3263–3268, 2012.

[108] S. H. Song, B. S. Kwak, J. S. Park, W. Kim, and H. I. Jung, "Novel application of Joule heating to maintain biocompatible temperatures in a fully integrated electromagnetic cell sorting system," *Sensors and Actuators, A: Physical*, vol. 151, no. 1, pp. 64–70, 2009.

[109] S. Coskun, E. Selen Ates, and H. E. Unalan, "Optimization of silver nanowire networks for polymer light emitting diode electrodes.," *Nanotechnology*, vol. 24, no. 12, p. 125202, 2013.

[110] P.-H. Wang, S.-P. Chen, C.-H. Su, and Y.-C. Liao, "Direct Printed Silver Nanowire Thin Film Patterns for Flexible Transparent Heaters with Temperature Gradient," *RSC Adv.*, vol. 5, pp. 98412–98418, 2015.

[111] A. Kozłowska, G. Gawlik, R. Szewczyk, A. Piatkowska, and A. Krajewska, "Infrared Thermal Emission from Joule-Heated Graphene with Defects," *OSA Technical Digest*, 2014.

[112] O. C. Mullins, "The Asphaltenes," *Annual review of analytical chemistry (Palo Alto, Calif.)*, vol. 4, pp. 393–418, 2011.

[113] M. D. Walton, Y. S. Kim, C. J. Jan, E. P. McConnel, W. N. Everett, and J. C. Grunlan, "Deposition and patterning of conductive carbon black thin films," *Synthetic Metals*, vol. 157, no. 16-17, pp. 632–639, 2007.

[114] C. Jason Jan, M. D. Walton, E. P. McConnell, W. S. Jang, Y. S. Kim, and J. C. Grunlan, "Carbon black thin films with tunable resistance and optical transparency," *Carbon*, vol. 44, no. 10, pp. 1974–1981, 2006.

[115] F. K. Perkins, A. L. Friedman, E. Cobas, P. M. Campbell, G. G. Jernigan, and B. T. Jonker, "Chemical vapor sensing with monolayer MoS 2," *Nano Letters*, vol. 13, no. 2, pp. 668–673, 2013.

[116] B. Liu, L. Chen, G. Liu, A. N. Abbas, M. Fathi, and C. Zhou, "High-performance chemical sensing using Schottky-contacted chemical vapor deposition grown monolayer MoS2 transistors," *ACS Nano*, vol. 8, no. 5, pp. 5304–5314, 2014.

[117] M. Chhowalla, H. S. Shin, G. Eda, L.-J. Li, K. P. Loh, and H. Zhang, "The chemistry of two-dimensional layered transition metal dichalcogenide nanosheets.," *Nature chemistry*, vol. 5, no. 4, pp. 263–75, 2013.

[118] H. Zhu, Y. Wang, J. Xiao, M. Liu, S. Xiong, Z. J. Wong, Z. Ye, Y. Ye, X. Yin, and X. Zhang, "Observation of piezoelectricity in free-standing monolayer MoS.," *Nature nanotechnology*, vol. 10, no. 2, pp. 151–5, 2015.

[119] O. Lopez-Sanchez, D. Lembke, M. Kayci, A. Radenovic, and A. Kis, "Ultrasensitive photodetectors based on monolayer MoS2.," *Nature nanotechnology*, vol. 8, no. 7, pp. 497–501, 2013.

[120] Y. Shi, H. Li, and L.-J. Li, "Recent advances in controlled synthesis of two-dimensional transition metal dichalcogenides via vapour deposition techniques," *Chem. Soc. Rev.*, oct 2014.

[121] C. Cong, J. Shang, X. Wu, B. Cao, N. Peimyoo, C. Qiu, L. Sun, and T. Yu, "Synthesis and Optical Properties of Large-Area Single-Crystalline 2D Semiconductor WS 2 Monolayer from Chemical Vapor Deposition," *Advanced Optical Materials*, vol. 2, no. 2, pp. 131–136, 2014.

[122] C. Huang, S. Wu, A. M. Sanchez, J. J. P. Peters, R. Beanland, J. S. Ross, P. Rivera, W. Yao, D. H. Cobden, and X. Xu, "Lateral heterojunctions within monolayer MoSe2–WSe2 semiconductors," *Nature Materials*, pp. 1–6, aug 2014.

[123] D. Dumcenco, D. Ovchinnikov, K. Marinov, P. Lazić, M. Gibertini, N. Marzari, O. L. Sanchez, Y.-c. Kung, D. Krasnozhon, M.-w. Chen, S. Bertolazzi, P. Gillet, A. Fontcuberta i Morral, A. Radenovic, and A. Kis, "Large-Area Epitaxial Monolayer MoS 2," *ACS Nano*, vol. 9, no. 4, pp. 4611–4620, 2015.

[124] K. Kang, S. Xie, L. Huang, Y. Han, P. Y. Huang, K. F. Mak, C.-J. Kim, D. Muller, and J. Park, "High-mobility three-atom-thick semiconducting films with wafer-scale homogeneity," *Nature*, vol. 520, no. 7549, pp. 656–660, 2015.

[125] I. Bilgin, F. Liu, A. Vargas, A. Winchester, M. K. L. Man, M. Upmanyu, K. Dani, G. Gupta, S. Talapatra, A. D. Mohite, and S. Kar, "Chemical Vapor Deposition Synthesized Atomically-Thin Molybdenum Disulfide with Optoelectronic-Grade Crystalline Quality," *ACS Nano*, vol. 10, no. 1021, p. 5b02019, 2015.

[126] Y. Yu, C. Li, Y. Liu, L. Su, Y. Zhang, and L. Cao, "Controlled scalable synthesis of uniform, high-quality monolayer and few-layer MoS2 films.," *Scientific reports*, vol. 3, p. 1866, 2013.

[127] L. Zhou, K. Xu, A. Zubair, A. D. Liao, W. Fang, F. Ouyang, Y. H. Lee, K. Ueno, R. Saito, T. Palacios, J. Kong, and M. S. Dresselhaus, "Large-Area Synthesis of High-Quality Uniform Few-Layer MoTe<inf>2</inf>," *Journal of the American Chemical Society*, vol. 137, no. 37, pp. 11892–11895, 2015.

[128] A. Bertuch, G. Sundaram, M. Saly, D. Moser, and R. Kanjolia, "Atomic layer deposition of molybdenum oxide using bis(tert-butylimido)bis(dimethylamido) molybdenum," *Journal of Vacuum Science & Technology A: Vacuum, Surfaces, and Films*, vol. 32, no. 1, p. 01A119, 2014.

[129] A. Haas, "The Chemistry of Silicon-Sulfur Compounds," *Angewandte Chemie International Edition in English*, vol. 4, no. 12, pp. 1014–1023, 1965.

[130] R. Carlson, R. Hall, and E. Pell, "Sulfur in silicon," *Journal of Physics and Chemistry of Solids*, vol. 8, pp. 81–83, 1959.

[131] Y.-C. Lin, W. Zhang, J.-K. Huang, K.-K. Liu, Y.-H. Lee, C.-T. Liang, C.-W. Chu, and L.-J. Li, "Wafer-scale MoS2 thin layers prepared by MoO3 sulfurization," *Nanoscale*, vol. 4, no. 20, p. 6637, 2012.

[132] Y. Zhang, Y. Zhang, Q. Ji, J. Ju, H. Yuan, J. Shi, T. Gao, D. Ma, M. Liu, Y. Chen, X. Song, H. Y. Hwang, Y. Cui, and Z. Liu, "Controlled Growth of High-Quality Monolayer WS 2 Layers on Sapphire," *ACS nano*, vol. 7, no. 10, pp. 8963–8971, 2013.

[133] M. Amani, D.-H. Lien, D. Kiriya, J. Xiao, A. Azcatl, J. Noh, S. R. Madhvapathy, R. Addou, S. KC, M. Dubey, K. Cho, R. M. Wallace, S.-C. Lee, J.-H. He, J. W. Ager, X. Zhang, E. Yablonovitch, and A. Javey, "Near-unity photoluminescence quantum yield in MoS2," *Science*, vol. 350, no. 6264, pp. 1065–1068, 2015.

[134] M. Amani, R. A. Burke, X. Ji, P. Zhao, D.-H. Lien, P. Taheri, G. H. Ahn, D. Kiriya, J. W. Ager, E. Yablonovitch, J. Kong, M. Dubey, and A. Javey, "High Luminescence Efficiency in MoS2 Grown by Chemical Vapor Deposition," *ACS Nano*, p. acsnano.6b03443, 2016.

[135] Y. Hao, M. S. Bharathi, L. Wang, Y. Liu, H. Chen, S. Nie, X. Wang, H. Chou, C. Tan, B. Fallahazad, H. Ramanarayan, C. W. Magnuson, E. Tutuc, B. I. Yakobson, K. F. McCarty, Y.-W. Zhang, P. Kim, J. Hone, L. Colombo, and R. S. Ruoff, "The role of surface oxygen in the growth of large single-crystal graphene on copper.," *Science (New York, N.Y.)*, vol. 342, no. 6159, pp. 720–3, 2013.

[136] J.-H. Lee, E. K. Lee, W.-J. Joo, Y. Jang, B.-S. Kim, J. Y. Lim, S.-H. Choi, S. J. Ahn, J. R. Ahn, M.-H. Park, C.-W. Yang, B. L. Choi, S.-W. Hwang, and D. Whang, "Wafer-Scale Growth of Single-Crystal Monolayer Graphene on Reusable Hydrogen-Terminated Germanium," *Science*, vol. 344, no. 6181, pp. 286–289, 2014.

[137] G. Eda, H. Yamaguchi, D. Voiry, T. Fujita, M. Chen, and M. Chhowalla, "Photoluminescence from chemically exfoliated MoS2.," *Nano letters*, vol. 11, pp. 5111–6, dec 2011.

[138] K. Nawaz, M. Ayub, M. Khan, A. Hussain, A. Q. Malik, M. B. K. Niazi, M. Hussain, A. U. Khan, and N. Ul-Haq, "Effect of concentration of Surfactant on the Exfoliation of Graphite to Graphene in Aqueous Media," *Nanomaterials and Nanotechnology*, p. 1, 2016.

[139] R. Petro, P. Borodulin, T. E. Schlesinger, and M. Schlesinger, "Liquid Exfoliated Graphene: A Practical Method for Increasing Loading and Producing Thin Films," *ECS Journal of Solid State Science and Technology*, vol. 5, no. 2, pp. P36–P40, 2016.

[140] S. Yumin, P. June, J. K. Yu, S. Maeng-Je, and H. Seunghun, "Synthesis of Graphene Layers Using Graphite Dispersion in Aqueous Surfactant Solutions," *Journal of the Korean Physical Society*, vol. 58, no. 41, p. 938, 2011.

[141] R. J. Smith, P. J. King, M. Lotya, C. Wirtz, U. Khan, S. De, A. O'Neill, G. S. Duesberg, J. C. Grunlan, G. Moriarty, J. Chen, J. Wang, A. I. Minett, V. Nicolosi, and J. N. Coleman, "Large-scale exfoliation of inorganic layered compounds in aqueous surfactant solutions," *Advanced Materials*, vol. 23, no. 34, pp. 3944–3948, 2011.

[142] G. Cunningham, M. Lotya, C. S. Cucinotta, S. Sanvito, S. D. Bergin, R. Menzel, M. S. P. Shaffer, and J. N. Coleman, "Solvent Exfoliation of Transition Metal Dichalcogenides : Dispersability of Exfoliated Nanosheets Varies Only Weakly Between Compounds Solvent Exfoliation of Transition Metal Dichalcogenides : Dispersability of Exfoliated Nanosheets Varies Only Weakly Bet," *ACS Nano*, no. 4, pp. 3468–3480, 2012.

[143] W. Zhang, C.-P. Chuu, J.-K. Huang, C.-H. Chen, M.-L. Tsai, Y.-H. Chang, C.-T. Liang, Y.-Z. Chen, Y.-L. Chueh, J.-H. He, M.-Y. Chou, and L.-J. Li, "Ultrahigh-gain photodetectors based on atomically thin graphene-MoS2 heterostructures.," *Scientific reports*, vol. 4, p. 3826, jan 2014.

[144] S. Tongay, J. Zhou, C. Ataca, K. Lo, T. S. Matthews, J. Li, J. C. Grossman, and J. Wu, "Thermally Driven Crossover from Indirect toward Direct Bandgap in 2D Semiconductors: MoSe2 versus MoS2," *Nano Letters*, 2012.

[145] L. Malard, M. Pimenta, G. Dresselhaus, and M. Dresselhaus, "Raman spectroscopy in graphene," *Physics Reports*, vol. 473, pp. 51–87, apr 2009.